Bachelor Thesis

Calculation of Electron-Positron Pair Production from the Cosmic Photon Background as a Function of Redshift

Mika Gelowicz

Würzburg, July 9, 2025

Julius-Maximilians-Universität Würzburg
Lehrstuhl für Astronomie
Betreuer: Dr. Thomas Siegert

Abstract

The Cosmic Photon Background (CPB) is the isotropic radiation across the entire electromagnetic spectrum, ranging from radio to very high energy γ-rays. Interactions of the CPB with itself are expected to produce positrons via pair-production. The local emissivity at redshift $z = 0$ is about $2.0 \times 10^{-36}\,\mathrm{s^{-1}\,cm^{-3}}$, which translates into a local pair production rate of $2.6 \times 10^{45}\,\mathrm{s^{-1}}$ until 200 Mpc. However, the CPB evolves with time, as its components – such as stars, Active Galactic Nuclei, and the Cosmic Microwave Background – vary with redshift. Using luminosity functions to describe the redshift evolution of these sources, along with the energy shift due to expansion of the Universe, a model of the CPB up to $z = 10.0$ is developed. Using this model, the positron emissivity up to $z = 10.0$ is calculated. The corresponding pair production emissivity, which is the rate of positrons produced per volume, rises sharply from the local value to $1.8 \times 10^{-31}\,\mathrm{s^{-1}\,cm^{-3}}$ at redshift 2.7, after which it decreases again due to a lack of star formation. By integrating the emissivity over the comoving volume, the pair production rate can be calculated. This leads to a total cosmic pair production rate of $7.4 \times 10^{54}\,\mathrm{s^{-1}}$ until redshift 5.0, and $9.3 \times 10^{54}\,\mathrm{s^{-1}}$ up to redshift 10.0. Such a rate may result in a measurable contribution to the Cosmic γ-Ray Background if all the positrons produced also annihilate.

Contents

Chapter 1

Introduction

Physics at the end of the 19th century was in big disarray: An experiment conducted by the American physicists Albert A. Michelson and Edward W. Morley disproved the existence of the ether, which was introduced to describe the propagation of electromagnetic waves in vacuum (Michelson & Morley 1887); the photoelectric effect showed that the classical theory of waves, which stated that light of every frequency should be able to eject electrons from the surface of a metal, is flawed (Hallwachs 1888); and – perhaps most famously – that the spectrum of a Blackbody could not be explained by classical means (Rayleigh 1900).

However, all of these problems could eventually be solved by two new theories of physics – arguably the two most powerful and influential theories in their field. The results of the Michelson-Morley-experiment lead to Albert Einstein's *theory of relativity*; the latter two experiments were ultimately explained by *Quantum Mechanics*.

As it turned out, light is not always best described as a wave of continuous energy flow. Instead, light can also be described by a number of light particles – so-called *photons* – with discrete energies

$$E = h\nu, \tag{1.1}$$

Energy of a photon.

where h is Planck's constant, defined as $6.626\,070\,15 \times 10^{-34}\,\mathrm{J\,s}$ (Mohr et al. 2024), and ν the frequency of light. By doing so, the German physicist Max Planck was able to solve the problem of the *UV-catastrophe*, which predicted an unphysical increase in energy emitted for short wavelengths.

The most radical reform of Quantum mechanics was the introduction of the wavefunction ψ, which breaks away from the idea that each particle has a well-defined position. The wave equation's square modulus only provides a probability density of a particle location. Its behavior is governed by the Schrödinger equation.

$$i\hbar\frac{\partial}{\partial t}\Psi(\mathbf{r},t) = \left(-\frac{\hbar^2}{2m}\nabla^2 + V(\mathbf{r})\right)\Psi(\mathbf{r},t). \tag{1.2}$$

The Schrödinger equation.

This equation is, however, non-relativistic. The unification of the Schrödinger equation with special relativity was only made possible a few years later by Paul Dirac, an English physicist.

In 1928, he made a resounding discovery: The Dirac-equation (Dirac & Fowler 1928). Originally, his attempt to make Schrödinger's wave equation relativistic, it turned out to make a much more intriguing prediction: antimatter. Upon closer examination, the Dirac equation allowed for electrons with negative energy (Dirac & Fowler 1930). Dirac's interpretation was an "anti-electron" with positive charge – later named *positron*.

$$(i\gamma^\mu\partial_\mu - m)\psi = 0 \tag{1.3}$$

The Dirac equation.

Just a few years later, several scientists confirmed the existence of said particle. Irène Curie, daughter of Marie Curie, and Frédéric Joliot were the first to measure the positron but failed to interpret their results correctly (Leone & Robotti 2010). Carl David Anderson, American particle physicist, was eventually the first to also interpret the results of his experiment correctly. In 1932, he detected particles in his cloud chamber that had the same mass as an electron, but in a magnetic field their paths were curved oppositely, meaning their charge was positive – exactly the properties of the positron (Anderson 1933). Just a year later, Patrick Blackett together with Giuseppe Occhialin published their observations that sometimes positrons and electrons originate from the same point in the cloud chamber (Blackett & Occhialini 1933). That result confirmed the idea that one photon colliding with a nucleus could result into an electron-positron pair. The nucleus remains unchanged; it is only necessary to fulfill conservation of momentum. This process is called *pair production*.

Interactions between two (real) photons are also able to produce an electron-positron pair (see Fig. 1.2). The reverse process is possible as well: An electron and positron can annihilate back into two photons.

Today, positron-electron annihilation remains one of the most intriguing and unresolved puzzles in astrophysics, as the majority of its sources are still unidentified (Siegert 2023). Several promising candidates have been proposed, including nucleosynthesis via β^+-decay in stellar environments, photon-photon pair production in the dense radiation fields surrounding accreting compact objects, and exotic processes such as the annihilation or decay of dark matter candidates like Weakly Interacting Massive Particles (WIMPs).

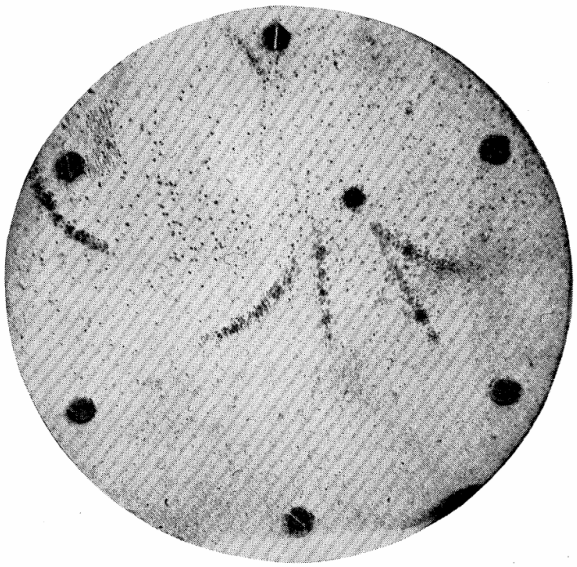

Figure 1.1: A total of six particle tracks. The outer right track of the central group of four tracks belongs to a positron (from Anderson 1933).

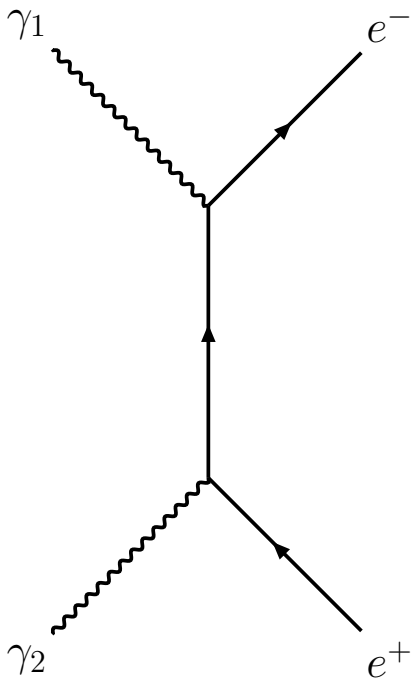

Figure 1.2: Feynman diagram of pair production. Two photons (γ_1, γ_2) interact to produce an electron (e^-) and a positron (e^+).

Pair production, one of the mechanisms capable of generating positrons, is expected to be efficient only in regions with extremely high photon densities. However, this limitation might be offset in part by the vast volumes, in which these processes may happen. If positrons produced in these environments survive long enough, they may eventually

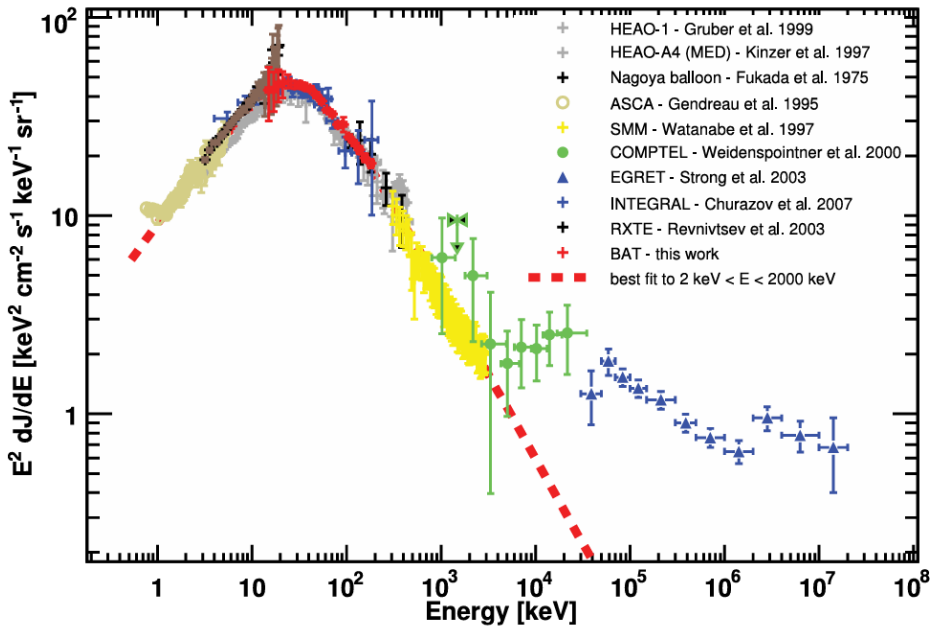

Figure 1.3: The CPB ranging from keV- up to high GeV-energies. Starting at a few MeVs, measurements of the CPB become sparse and generally have bigger errors than measurements in the keV (from Ajello et al. 2008).

annihilate and contribute to a diffuse signal. There could be a measurable signal in the Cosmic γ-Ray Background (CGB) from positron annihilation, although assessing this signal is challenging due to the significant uncertainties in the measured CGB spectrum (see Fig. 1.3).

The goal of this Bachelor Thesis is to calculate the cosmic positron pair production rate from the Cosmic Photon Background (CPB) at different redshifts corresponding to different cosmic times. This thesis is structured as follows: Chapter 2 focuses on the theoretical background, which includes the mathematical framework of pair production and the Blackbody spectrum described by Planck's law. It is also established what the CPB is and how it can be categorized. In Chapter 3, a model of the CPB is compiled by a combination of several Blackbody spectra. Further, each Blackbody is matched with a corresponding source composition. This is used in Chapter 4, where the evolution of each Blackbody is modeled. A useful tool for that is the luminosity function. This will lead to a comprehensive model of the Cosmic Photon Background. This model is used in Chapter 5 to calculate the cosmic positron rate up to redshift 10.0. This is followed by the final Chapter 6, which gives an outlook considering the cosmic-ray positron spectrum measured by the Alpha Magnetic Spectrometer on the International Space Station.

Chapter 2

Theory of Photon Interactions and Radiation

2.1 Pair production

Two colliding photons have a chance of producing an electron-positron pair, given that their combined energy is large enough, corresponding to 1022 keV as the rest mass energy of each electron or positron is 511 keV. A measure for that likelihood is the cross section σ, often measured in barn, which equals $10^{-28}\,\mathrm{m}^2$ or $10^{-24}\,\mathrm{cm}^2$, and can be interpreted as the area of the target a particle has to hit for an interaction to occur.

Given there are two photon fields $n(\varepsilon_1)$ and $n(\varepsilon_2)$, the resulting positron emissivity $\dot{n}_\pm$ can be estimated by

$$\dot{n}_\pm = c\, n(\varepsilon_1)\, n(\varepsilon_2)\, \sigma_{\mathrm{pair}}, \tag{2.1}$$

where c is the speed of light and ε_1, ε_2 the photon energies in terms of the electron mass; σ_{pair} is the cross section of the pair production process.

However, the cross section σ_{pair} is not constant for all energies – instead it is a function of β, the velocity of the produced electron or positron in the center-of-momentum frame (see Fig. 2.1) (Greiner & Reinhardt 2008: Jauch & Rohrlich 1976):

$$\sigma_{\mathrm{pair}} = \frac{3\sigma_T}{16}(1-\beta^2)\left[(3-\beta^4)\ln\left(\frac{1+\beta}{1-\beta}\right) - 2\beta(2-\beta^2)\right], \tag{2.2}$$

where σ_{T} is the Thomson cross section, which is $6.65 \times 10^{-25}\,\mathrm{cm}^2$ or 0.665 b. Further, β also depends on the angle of incidence θ_μ in the laboratory frame:

$$\beta = \sqrt{1 - \frac{2}{\varepsilon_1\varepsilon_2(1-\cos\theta_\mu)}}. \tag{2.3}$$

Hence, Eq. 2.1 needs to be adapted to include the energy and, thus, angle-dependent cross section as well as the kinematic boundary conditions – including the energy threshold

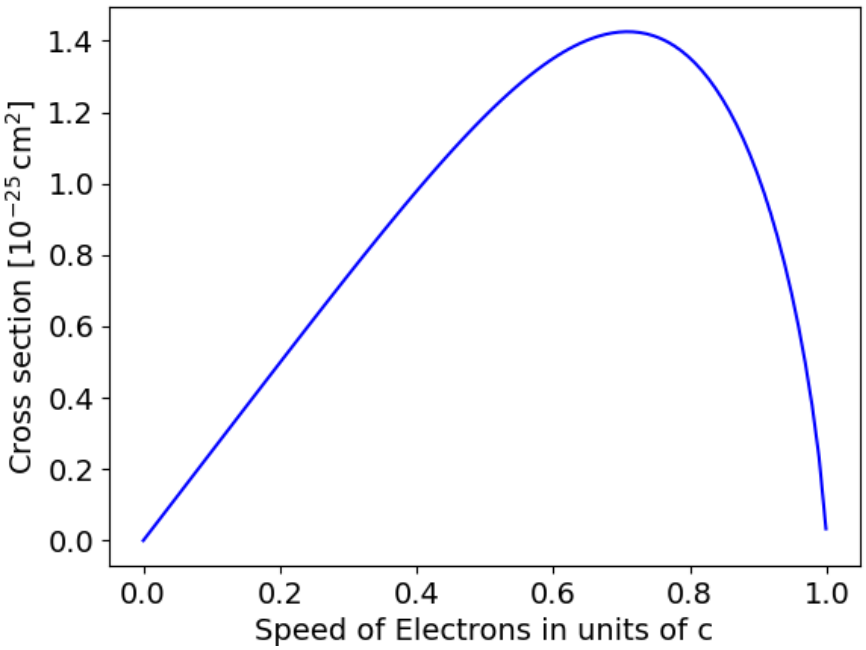

Figure 2.1: The cross section of the electron-positron pair production process as a function of the electron's velocity.

for pair production, which leads to the integral (Boettcher & Schlickeiser 1997):

$$\dot{n}_{\pm} = \frac{c}{4} \int_0^{\infty} \mathrm{d}\varepsilon_1 \, n_{\mathrm{ph}}(\varepsilon_1) \int_{\varepsilon_2^L}^{\infty} \mathrm{d}\varepsilon_2 \, n_{\mathrm{ph}}(\varepsilon_2) \int_{-1}^{1-\frac{2}{\varepsilon_1 \varepsilon_2}} \mathrm{d}\mu \, (1-\mu) \frac{\mathrm{d}\sigma}{\mathrm{d}\gamma}, \tag{2.4}$$

where

$$\varepsilon_2^L = \max\left\{\frac{1}{\varepsilon_1}, \gamma + 1 - \varepsilon_1\right\}, \tag{2.5}$$

and

$$\mu = \cos(\theta_\mu). \tag{2.6}$$

The first of the three integrals integrates over all possible energies of the first photon field; the second integral includes all energies larger than ε_2^L. This ensures that the energy of both photons is sufficient to produce an electron-positron pair. The last integral handles the angle-dependencies of the cross section. Its upper integration limit is also set by the energy threshold for pair production.

This last integral can be solved analytically, albeit the resulting calculation leads to a lengthy expression. The differential cross section $\frac{\mathrm{d}\sigma}{\mathrm{d}\gamma}$ can be expressed as:

$$\frac{\mathrm{d}\sigma}{\mathrm{d}\gamma} = \oint \mathrm{d}\Omega_{\mathrm{cm}} \frac{\mathrm{d}^2\sigma}{\mathrm{d}\Omega_{\mathrm{cm}} \, \mathrm{d}\gamma_{\mathrm{cm}}} \frac{\mathrm{d}\gamma_{\mathrm{cm}}}{\mathrm{d}\gamma}. \tag{2.7}$$

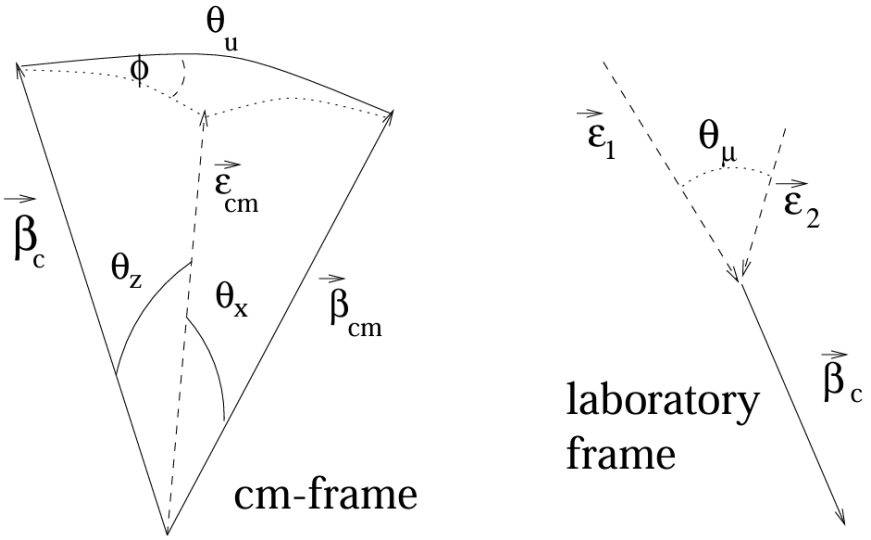

Figure 2.2: Visualization of used angles in center of momentum-system and laboratory frame (from Boettcher & Schlickeiser 1997).

with

$$\frac{\mathrm{d}^2\sigma}{\mathrm{d}\Omega_{\mathrm{cm}}\,\mathrm{d}\gamma_{\mathrm{cm}}} = \delta(\epsilon_{\mathrm{cm}} - \gamma_{\mathrm{cm}})\,\frac{\mathrm{d}\sigma}{\mathrm{d}\Omega_{\mathrm{cm}}}, \tag{2.8}$$

where

$$\begin{aligned}\frac{\mathrm{d}\sigma}{\mathrm{d}\Omega_{\mathrm{cm}}} = \frac{1}{2\pi}\frac{3}{16}\sigma_{\mathrm{T}}\frac{\beta_{\mathrm{cm}}}{\epsilon_{\mathrm{cm}}^2}\Bigg[-1 + \frac{3-\beta_{\mathrm{cm}}^4}{2}\left(\frac{1}{1-\beta_{\mathrm{cm}}x} + \frac{1}{1+\beta_{\mathrm{cm}}x}\right) \\ - \frac{1}{2\varepsilon_{\mathrm{cm}}^4}\left(\frac{1}{(1-\beta_{\mathrm{cm}}x)^2} + \frac{1}{(1+\beta_{\mathrm{cm}}x)^2}\right)\Bigg].\end{aligned} \tag{2.9}$$

The calculation included several quantities that are given in Fig- 2.2: the cosine of the angle between incoming photons and outgoing positron $x = \cos(\theta_x)$, the angle between both photons in the laboratory system $\mu = \cos(\theta_\mu)$, the velocity of an outgoing positron β_{cm}, the corresponding Lorentz factor γ_{cm}, and the energy of an incoming photon[1] $\varepsilon_{\mathrm{cm}}$ (again in terms of an electron's mass) as well as the Lorentz-factor of an electron in the laboratory frame γ and in the center-of-momentum frame γ_{cm}. The relation between β and γ in general is

$$\gamma = \frac{1}{\sqrt{1-\beta^2}}. \tag{2.10}$$

After a number of steps, the final expression for the emissivity of positrons only includes the first two integrals:

$$\dot{n}_{\pm} = \frac{3}{4}\sigma_{\mathrm{T}}c\int_0^\infty \mathrm{d}\varepsilon_1 \frac{n_{\mathrm{ph}}(\varepsilon_1)}{\varepsilon_1^2}\int_{\varepsilon_2^L}^\infty \mathrm{d}\varepsilon_2 \frac{n_{\mathrm{ph}}(\varepsilon_2)}{\varepsilon_2^2}\cdot\left[\frac{\sqrt{E^2-4\varepsilon_{\mathrm{cm}}^2}}{4} + H_+ + H_-\right]\Bigg|_{\varepsilon_{\mathrm{cm}}^L}^{\varepsilon_{\mathrm{cm}}^U}, \tag{2.11}$$

[1] In the center-of-momentum frame both photons have the same energy.

which includes the auxiliary function $H_{\pm}$:

$$\begin{aligned} H_{\pm} = &-\frac{\varepsilon_{\mathrm{cm}}}{8\sqrt{\varepsilon_1\varepsilon_2 + c_{\pm}\varepsilon_{\mathrm{cm}}^2}}\left(\frac{d_{\pm}}{\varepsilon_1\varepsilon_2} + \frac{2}{c_{\pm}}\right) \\ &+ \frac{1}{4}\left(2 - \frac{\varepsilon_1\varepsilon_2 - 1}{c_{\pm}}\right) I_{\pm} \\ &+ \frac{\sqrt{\varepsilon_1\varepsilon_2 + c_{\pm}\varepsilon_{\mathrm{cm}}^2}}{4}\left(\frac{\varepsilon_{\mathrm{cm}}}{c_{\pm}} + \frac{1}{\varepsilon_{\mathrm{cm}}\varepsilon_2\varepsilon_1}\right) \end{aligned} \tag{2.12}$$

with

$$I_{\pm} = \begin{cases} \frac{1}{\sqrt{c_{\pm}}} \ln\left(\varepsilon_{\mathrm{cm}}\sqrt{c_{\pm}} + \sqrt{\varepsilon_1\varepsilon_2 + c_{\pm}\varepsilon_{\mathrm{cm}}^2}\right) & \text{if } c_{\pm} > 0 \\ \frac{1}{\sqrt{-c_{\pm}}} \arcsin\left(\varepsilon_{\mathrm{cm}}\sqrt{-\frac{c_{\pm}}{\varepsilon_1\varepsilon_2}}\right) & \text{if } c_{\pm} < 0 \end{cases}. \tag{2.13}$$

For $c_{\pm} = 0$ the auxiliary function $H_{\pm}$ simplifies to:

$$H_{\pm} = \left(\frac{\varepsilon_{\mathrm{cm}}^3}{12} - \frac{\varepsilon_{\mathrm{cm}} d_{\pm}}{8}\right)\frac{1}{(\varepsilon_1\varepsilon_2)^{3/2}} + \left(\frac{\varepsilon_{\mathrm{cm}}^3}{6} + \frac{\varepsilon_{\mathrm{cm}}}{2} + \frac{1}{4\varepsilon_{\mathrm{cm}}}\right)\frac{1}{\sqrt{\varepsilon_1\varepsilon_2}}. \tag{2.14}$$

These equations included the terms

$$c_{\pm} = (\varepsilon_{1,2} - \gamma)^2 - 1, \tag{2.15}$$

$$d_{\pm} = \varepsilon_{1,2}^2 + \varepsilon_1\varepsilon_2 \pm \gamma\,(\varepsilon_2 - \varepsilon_1), \tag{2.16}$$

and for the integration limits

$$\varepsilon_{\mathrm{cm}}^U = \min\left\{\sqrt{\varepsilon_1\varepsilon_2}, \varepsilon_{\mathrm{cm}}^*\right\}, \qquad \varepsilon_{\mathrm{cm}}^L = \max\left\{1, \varepsilon_{\mathrm{cm}}^{\dagger}\right\}, \tag{2.17}$$

with

$$\left(\varepsilon_{\mathrm{cm}}^{*,\dagger}\right)^2 = \frac{1}{2}\left(\gamma(E-\gamma) + 1 \pm \sqrt{\left[\gamma(E-\gamma)+1\right]^2 - E^2}\right), \tag{2.18}$$

and

$$E = \varepsilon_1 + \varepsilon_2. \tag{2.19}$$

This leaves only the integrals of the two photon fields to be calculated.

2.2 The Blackbody and Planck's law

A Blackbody (BB) is an idealized physical body that absorbs all incident electromagnetic radiation, regardless of frequency or angle of incidence. A BB is also in thermal equilibrium with its surroundings, meaning thatall of the incoming radiation must be re-emitted. The resulting intensity spectrum is only dependent on the BB-temperature and exhibits a very characteristic shape, whose specific intensity is described by Planck's law:

$$I_{\nu}(\nu, T) = \frac{2h\nu^3}{c^2}\frac{1}{\exp\left(\frac{h\nu}{k_{\mathrm{B}}T}\right) - 1}, \tag{2.20}$$

where $c = 299\,792\,458\,\frac{\mathrm{m}}{\mathrm{s}}$ is the speed of light, and $k_\mathrm{B} = 1.380\,649 \times 10^{-23}\,\frac{\mathrm{J}}{\mathrm{K}}$ the Boltzmann constant (Mohr et al. 2024). This is a differential quantity, meaning that the density is given per unit frequency, denoted by the index. It can be interpreted as the intensity per solid angle and unit frequency. As the horizontal axis is mostly not given in terms of frequency but logarithmic frequency, the specific intensity often appears in the form

$$\nu I_\nu(\nu, T) = \frac{2h\nu^4}{c^2} \frac{1}{\exp\left(\frac{h\nu}{k_\mathrm{B}T}\right) - 1}, \tag{2.21}$$

considering $\mathrm{d}\nu = \nu \cdot \mathrm{d}\log(\nu)$.

The number density is related to the energy density,

$$u_\nu(\nu, T) = \frac{8\pi h\nu^3}{c^3} \frac{1}{\exp\left(\frac{h\nu}{k_\mathrm{B}T}\right) - 1}, \tag{2.22}$$

which, by dividing with the energy of one photon, results in an expression for the number density:

$$n_\nu(\nu, T) = \frac{8\pi\nu^2}{c^3} \frac{1}{\exp\left(\frac{h\nu}{k_\mathrm{B}T}\right) - 1}. \tag{2.23}$$

Since in astrophysics photons are often given in terms of their energy and not frequency, an equivalent expression in terms of energy is:

$$n_E(E, T) = \frac{8\pi}{(hc)^3} \frac{E^2}{\exp\left(\frac{E}{k_\mathrm{B}T}\right) - 1}. \tag{2.24}$$

The additional factor h in the denominator arises from the differential nature of the photon density, as it returns the number of photons per frequency or energy interval.

2.3 Overview of the Cosmic Photon Background

The CPB is an isotropic radiation that ranges across the entire electromagnetic spectrum. It is typically separated into seven different energy ranges (e.g., Hill et al. 2018), even though there are many more astrophysical components (see Ch. 3). However, as the γ-Ray Background encompasses such a large energy range, it is, here, further divided up into three subcategories:

- Cosmic Radio Background (CRB)
- Cosmic Microwave Background (CMB)
- Cosmic Infrared Background (CIB)
- Cosmic Optical Background (COB)

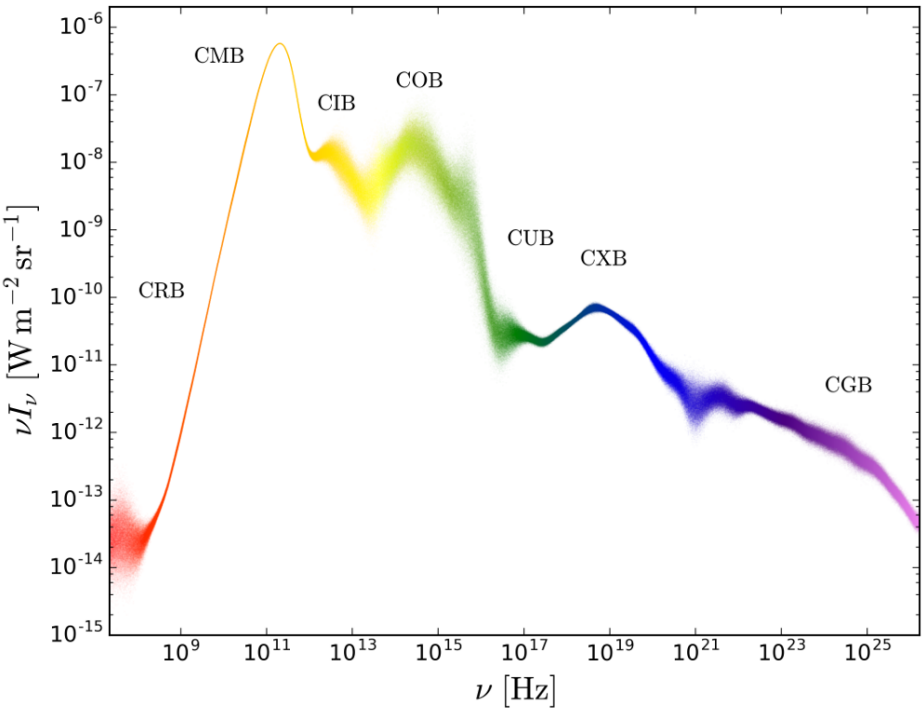

Figure 2.3: The Spectrum of the local Universe as a function of frequency. The different energy ranges are labeled, varying uncertainties of measurements are implied (from Hill et al. 2018).

- Cosmic Ultraviolet Background (CUB)
- Cosmic X-Ray Background (CXB)
- Cosmic γ-Ray Background (CGB):
  - Soft γ-Rays
  - γ-Rays
  - Very High Energies (VHE)

For lower energies, the CPB is limited by the plasma frequency of the interstellar medium (ISM); for light with low enough frequencies, the Universe is virtually opaque. At the high-energy end, observations are limited by the large cross section of these photons interacting with those comprising the CIB. A spectrum of the CPB from 10^7 Hz (10^{-7} eV) to 10^{26} Hz (10^{12} eV) is shown in Fig. 2.3. The sources and typical limits of each energy range can be seen in Tab. 2.1.

	Main sources	**Frequency/wavelength/energy range**
CRB	Synchrotron radiation, Active Galactic Nuclei (AGNs)	$\nu < 10$ GHz
CMB	Surface of last scattering	$\nu = 10$–1000 GHz
CIB	Dust heated by stars, old galaxies	$\lambda = 3$–300 μm
COB	Direct starlight	$\lambda = 300$–3000 nm
CUB	Hot, young stars	$\lambda = 30$–300 nm
CXB	Accretion disks around AGNs	$E = 0.1$–100 keV
	Quasars, FSRQs, SNe (Soft γ-Rays)	$E = 100\,\mathrm{keV} - 20\,\mathrm{MeV}$
CGB	FSRQs, BL Lacs (γ-Rays)	$E = 20\,\mathrm{MeV} - 5\,\mathrm{GeV}$
	BL Lacs (Very High Energies)	$E > 5\,\mathrm{GeV}$

Table 2.1: Main sources making up each energy range of the CPB and their corresponding extent expressed in suitable units (Hill et al. 2018). Because of the wide energy range of the CGB, it is further divided up into three sub-categories.

Chapter 3

Modeling the Photon Background

3.1 Decomposition into Blackbodies

The choice of decomposing the CPB into BB spectra is arbitrary but can be motivated by the simplicity and smoothness. Undoubtedly, also a power-law decomposition would work, but since the CMB is, indeed, a perfect BB, this functional form is used. A data compilation of different observations from Hill et al. (2018) to model the CPB was adopted. In total, the model includes 28 BBs, which were fitted to the data set by χ^2-minimization (Penny 2025).

As Planck's law only leaves the temperature T as a free parameter, an amplitude A as another free parameter was introduced, that scales the power of the other BBs, as otherwise, their magnitude would be fixed.

Hence, the full model

$$\nu I_\nu = \sum_{i=1}^{28} A_i \frac{2h\nu^4}{c^2} \frac{1}{\exp\left(\frac{h\nu}{k_\mathrm{B} T_i}\right) - 1}, \tag{3.1}$$

includes a total of 54 parameters, 27 temperatures and 27 amplitudes, and the fixed parameters $T^0_\mathrm{CMB} = 2.725\,\mathrm{K}$ and $A^0_\mathrm{CMB} = 1.0$ for the CMB. This leads to a reasonable description of the overall spectral shape of the CPB without large residuals. The resulting decomposition of the CPB into BBs can be seen in Fig. 3.1. Colors indicate different energy ranges according to the division shown in Tab. 2.1.

3.2 Conversion of temperature scales

Up to this point, only the temperatures of each BB are known as the result of the χ^2-minimization. Observations, however, are often performed in a specific wavelength, frequency, or energy range. Finding a relation that links each quantity to the temperature

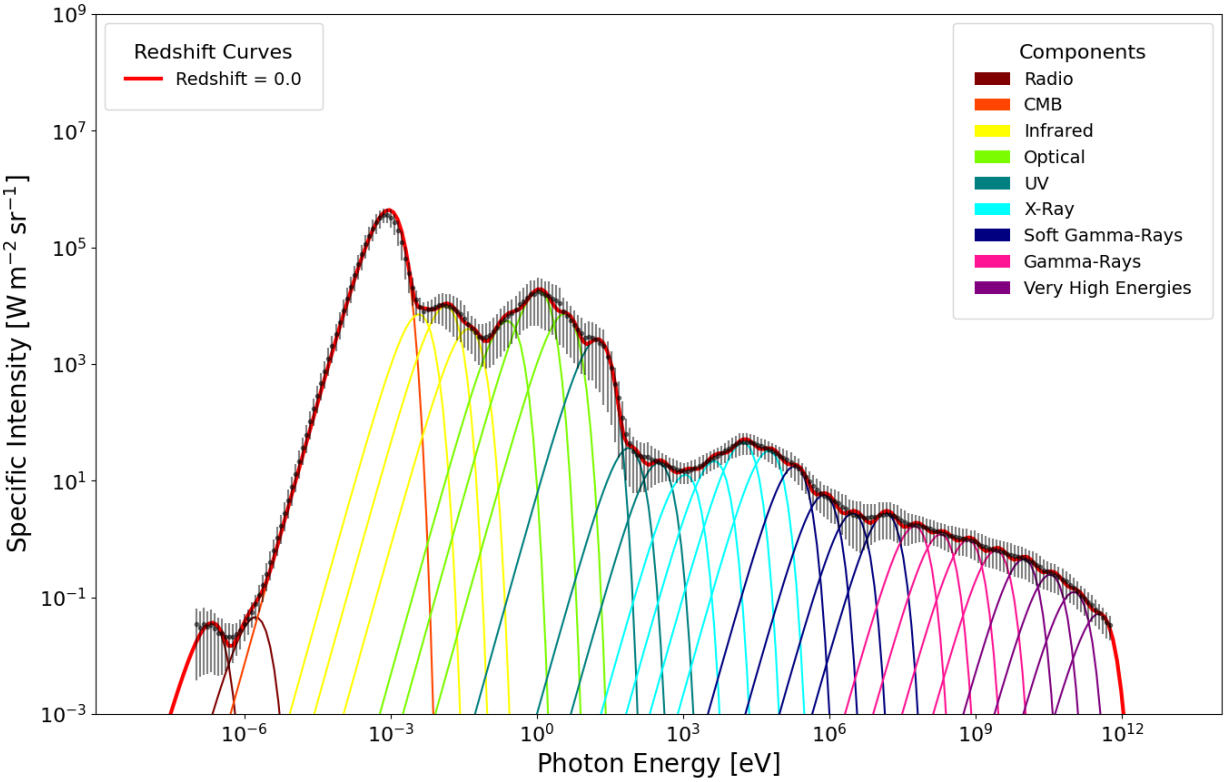

Figure 3.1: CPB spectrum (black data points) (data taken from Hill et al. 2018) together with a BB decomposition. The colors indicate the different spectral ranges (see Tab. 2.1).

of a BB is therefore essential. A suitable approach is to use the peak-wavelength λ_{peak}, peak-frequency ν_{peak}, or the average energy $\langle E \rangle$ of each BB.

Determining the peak-frequency corresponds to finding the maximum of the energy density $u_\nu(\nu, T)$. Differentiating with respect to ν yields:

$$\frac{\mathrm{d}u_\nu}{\mathrm{d}\nu} = \frac{8\pi h}{c^2} \frac{\exp\left(\frac{h\nu}{k_\mathrm{B}T}\right)\left[3\nu^2 - \frac{h\nu^3}{k_\mathrm{B}T}\right] - 3\nu^2}{\left[\exp\left(\frac{h\nu}{k_\mathrm{B}T}\right) - 1\right]^2}. \tag{3.2}$$

Setting this expression to 0 and simplifying leads to:

$$\exp\left(\frac{h\nu}{k_\mathrm{B}T}\right)\left[\frac{h\nu}{k_\mathrm{B}T} - 3\right] + 3 = 0. \tag{3.3}$$

With the substitution $x := \frac{h\nu}{k_\mathrm{B}T} - 3$ and the Lambert W function[1] the solution can be

[1]The Lambert W function solves equations of the form $x\,\mathrm{e}^x = k$, where k is some constant. It consists of two branches (the principal branch W_0 and the lower branch W_{-1}) leading to two solution for negative k. For $k > 0$, the principal branch W_0 is suffice.

written as:

$$x_{\text{peak}} = W_0(3e^{-3}) \approx -0.179, \tag{3.4}$$

which corresponds to a peak-frequency of

$$\nu_{\text{peak}} = \frac{k_{\text{B}}T}{h}\left(3 + W_0(3e^{-3})\right) = d \cdot T \tag{3.5}$$

with $\mathrm{d} = 5.879 \times 10^{10}\,\mathrm{Hz} \cdot \mathrm{K}^{-1}$.

A similar calculation can be made for the peak frequency λ_{peak}, leading to

$$\lambda_{\text{peak}} = \frac{hc}{k_{\text{B}}T\ (5 + W_0(-5e^{-5}))} = \frac{b}{T} \tag{3.6}$$

with $b = 2.898 \times 10^{-3}\,\mathrm{m} \cdot \mathrm{K}$

To find an expression for the average energy $\langle E \rangle$, one needs to calculate the total energy density

$$u_{\text{total}} = \int_0^\infty E \cdot n_E(E)\mathrm{d}E \tag{3.7}$$

and the total photon density

$$n_{\text{total}} = \int_0^\infty n_E(E)\mathrm{d}E; \tag{3.8}$$

the average energy is then

$$\langle E \rangle = \frac{u_{\text{total}}}{n_{\text{total}}}. \tag{3.9}$$

First integral can be solved with the substitution $x := \frac{E}{k_{\text{B}}T}$:

$$u_{\text{total}} = \frac{8\pi(k_{\text{B}}T)^4}{(hc)^3}\int_0^\infty \frac{x^3}{e^x - 1}\mathrm{d}x = \frac{8\pi(k_{\text{B}}T)^4}{(hc)^3}\underbrace{\Gamma(4)}_{3!=6}\underbrace{\zeta(4)}_{\frac{\pi^4}{90}} = \frac{\pi^4}{15}\frac{8\pi(k_{\text{B}}T)^4}{(hc)^3}, \tag{3.10}$$

where $\Gamma(x)$ is the Gamma function and $\zeta(x)$ is the Riemann zeta function. Similarly, the integral for the total photon density results in:

$$n_{\text{total}} = \frac{8\pi(k_{\text{B}}T)^3}{(hc)^3}\int_0^\infty \frac{x^2}{e^x - 1}\mathrm{d}x = \frac{8\pi(k_{\text{B}}T)^4}{(hc)^3}\underbrace{\Gamma(3)}_{2!=2}\zeta(3) = 2\zeta(3)\frac{8\pi(k_{\text{B}}T)^3}{(hc)^3}. \tag{3.11}$$

This, finally, leads to the expression:

$$\langle E \rangle = \frac{\pi^4}{30\zeta(3)}k_{\text{B}}T \approx 2.701\,k_{\text{B}}T. \tag{3.12}$$

3.3 Identification of source composition

To determine the exact evolution of each BB, it is necessary to first match each BB to one or more source types. The results of this BB-source type matching are summarized in Tab. 3.1, and described in the following.

3.3.1 Cosmic Radio Background (CRB)

The CPB in the radio regime ($\nu < 10\,\mathrm{GHz}$) is dominated by free-free emission and synchrotron radiation, originating from Active Galactic Nuclei (AGNs) and star-forming galaxies (SFGs), respectively. Both processes are quite similar in their origin.

Free-free emission is most prevalent in clouds of H-II (hydrogen II), that is, ionized hydrogen. If an electron moves past such an ion, its trajectory gets curved and, thus, emits bremsstrahlung, also called free-free emission. This process often happens near newborn stars that are high in UV-radiation, which is the reason that this type of emission is closely connected to the star formation rate (SFR) of the Universe.

A comparable process occurs near AGNs, where strong magnetic fields form. Relativistic electrons are forced on curved paths when passing through these fields, which leads to the emission of synchrotron radiation.

AGNs and SFGs are believed to contribute equally to this part of the CPB, although their combined contribution can only explain about one fifth of the CRB. The discrepancy is most likely a result of insufficient foreground models or an unknown diffuse source (Tompkins et al. 2023).

The CRB is modeled by the first two BBs.

3.3.2 Cosmic Microwave Background (CMB)

The CMB ($\nu = 10 - 1000\,\mathrm{GHz}$) is perhaps the most well understood part of the CPB. Shortly after the Big Bang, elementary particles started forming. The cooling of the Universe led to the first electrons and stable nuclei (mostly hydrogen and helium). However, the temperature of the Universe was still too high to form neutral atoms; instead, space was filled with a hot, ionized plasma, that scattered light – the Universe was opaque.

After about 380.000 years, the Universe cooled down enough, that electrons could recombine with protons to form neutral hydrogen – the Universe became transparent. At that time, the temperature of the Universe was about 3000 K, but with the expansion of the Universe, this radiation cooled down and shifted to longer wavelengths; nowadays, it can be seen as the CMB with a temperature of 2.725 K. Due to the near-perfect homogeneity of the early Universe, this radiation is isotropic and matches an almost perfect BB (e.g., Lahav & Liddle 2024). The *Planck* spacecraft, operated by the European Space Agency from 2009 to 2013, measured the anisotropies of the CMB with staggering precision, which can be seen in Fig. 3.2. The origin of this radiation – the surface of last scattering at $z = 1100$ – limits the observable Universe to its boundaries. The CMB is modeled by BB 3.

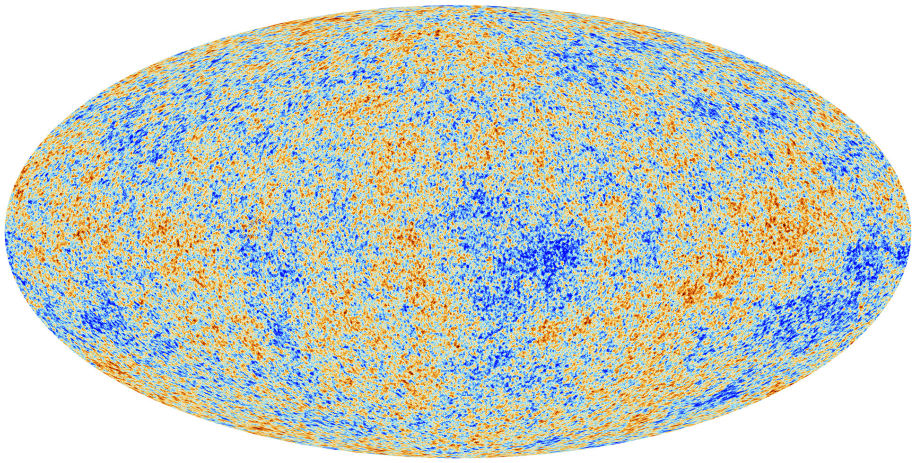

Figure 3.2: The CMB (Planck Collaboration et al. 2020b). Measured by the *Planck* satellite, its temperature anisotropies are on the order of $\sim 10^{-5}$ relative to its temperature of 2.725 K.

3.3.3 Cosmic Infrared Background (CIB)

The CIB ($\lambda = 3 - 300\,\mu\text{m}$) is an important tracer for the cosmic SFR of the Universe, as approximately 50 % of the total radiative energy output from stars over the history of the Universe lies in that energy range. Additionally, dust in galaxies heated by stars and the most redshifted galaxies contribute to the CIB (Lagache et al. 2005). Because of the big foreground emission from the Sun, planets, and the Galaxy, it is hard to precisely measure the intensity of the CIB. Another issue for Earth-bound observations arises from the molecular absorption and scattering by different molecules in Earth's atmosphere. This leads to certain wavelength windows, in which observations are possible; outside of these windows, the absorption can be as large as 100%. Often, only upper or lower limits that rely on theoretical models and estimations are available. AGNs, which were significant contributors for lower energies, become subdominant for intermediate energies (Hill et al. 2018). Therefore, this model uses 100 % contribution from galaxies for the CIB, which is modeled by BB 4 – 6.

3.3.4 Cosmic Optical Background (COB)

The COB ($\lambda = 300 - 3000\,\text{nm}$) is, in most regards, similar to the CIB. Its sources are likewise stars and galaxies, but in this case, the observed light originates directly from the sources, rather than being re-emitted by dust. Other sources are marginal and can be neglected. The challenges of direct measurements by extinction remain for the COB as well, but are now caused by tiny dust particles in the ISM that leads to significant extinction (Longair 2011). BBs 7 – 9 fall into this category.

3.3.5 Cosmic UV-Background (CUB)

The CUB ($\lambda = 30 - 300\,\mathrm{nm}$) is even less understood than the two previous energy ranges. Measurements are limited by the same factors and, additionally, by the UV-absorption of hydrogen and Earth's atmosphere, which is nearly-opaque for UV-light (Longair 2011). Especially important are two wavelengths in that energy range: 912 Å and 228 Å. The former corresponds roughly to the ionization energy of neutral hydrogen of 13.6 eV, the latter to the ionization energy of singly ionized helium. Both elements have non-negligible abundances in galaxies and models rely heavily on their properties (Khaire & Srianand 2019). It consists of contributions from galaxies, such as light of hot, young stars, as well as AGN-contribution in the form of quasars. It encompasses BBs 10 – 12.

3.3.6 Cosmic X-Ray Background (CXB)

The observational challenges that affected earlier low-energy measurements remain significant in the X-ray band ($E = 0.1 - 100\,\mathrm{keV}$) as well, though in different ways. While interstellar absorption is less severe than in the UV, X-ray observations are complicated by bright Galactic foreground emission, uncertainties in absolute calibration due to the lack of a true standard candle, and reliance on sources like the Crab nebula for relative flux normalization. Contributions from galaxies cease to be dominant for these energies;

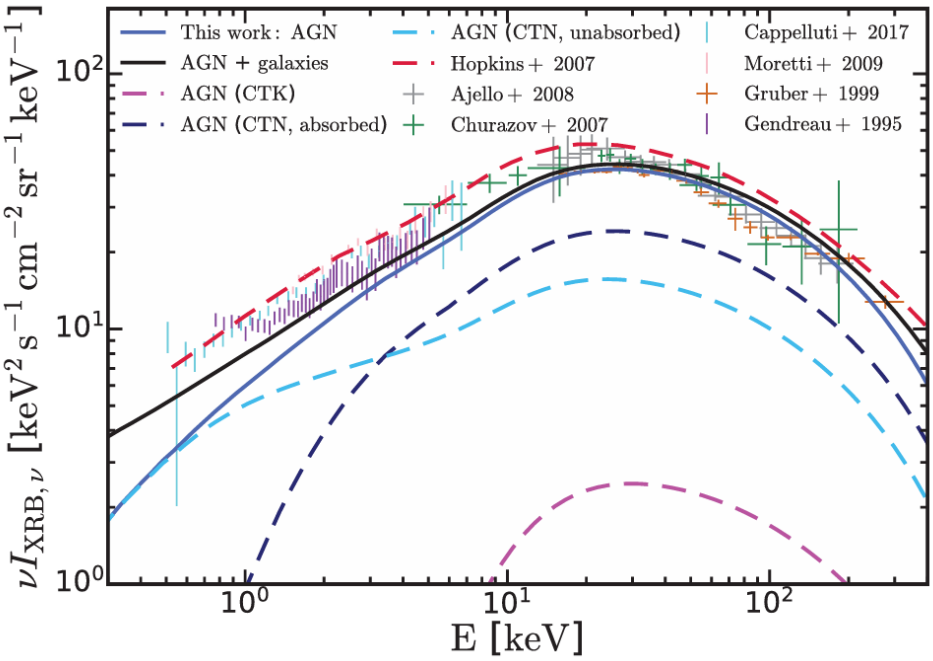

Figure 3.3: The CPB in the keV-range. It is dominated by AGNs with a small constant contribution from galaxies (from Shen et al. 2020).

instead, AGNs and their accretion disks are finally becoming the most dominant sources (Shen et al. 2020). Fig. 3.3 shows measurements of the CPB for keV-energies together with a model dominated by AGNs. The CXB is modeled by BBs 13 – 16.

3.3.7 Cosmic γ-Ray Background (CGB)

The CGB makes up the largest part of the CPB with 12 of the total 28 BBs being categorized as such. Because of the vast energy range the CGB ranges across, it is further split up into three subcategories.

Soft γ-Rays

This part includes BBs 17 – 20 and, thus, stretches from a few 100 keV to about 20 MeV. Its sources are – especially in the low MeV-range – not well understood, and there is no consensus on what sources precisely make up the CGB.

For the lower half, quasars seem to be the dominant source (Marcotulli et al. 2022), but there is an increasing contribution by Flat Spectrum Radio Quasars (FSRQs) starting at a few 100 keV (see left panel of Fig. 3.4) (Ajello et al. 2009). These are radio-loud quasars with a flat radio spectrum and are a subclass of blazars, which are a type of AGNs themselves. FSRQs are characterized by their strong and broad optical emission lines.

On the upper energetic end, supernovae of type Ia (SNe Ia) may be somewhat dominant, contributing about a quarter of sources around 1 MeV, as shown in the right panel of Fig. 3.4 (Ruiz-Lapuente et al. 2016). Those types of SNe emerge from the interaction within a binary star system. Because it is highly unlikely that both stars have the same mass, their reflective lifetimes will also differ. In the case, where one star becomes a white dwarf, it might accrete matter from the other star. White dwarf stars are in an equilibrium state, where the gravitational pulls inward and the pressure of degenerate electron gas are in balance – an effect arising from Pauli's exclusion principle that prevents any more compression. However, as more gas accumulates around the white dwarf, the pressure from that degenerate electron gas is eventually not strong enough to counterbalance the ever-growing gravitational force from outside. When reaching a mass of $1.44 M_{\odot}$, which is known as the Chandrasekhar limit, the core's temperature rises enough to fuse carbon and oxygen, which triggers an enormous release of energy within just a few seconds – the star unbinds and sends out a shock wave into space, which is observed as a supernova.

During this collapse, large amounts of heavy elements are formed. One of these is the radioactive isotope ^{56}Ni (decay time $\sim$ 8.8 days), that, through ^{56}Co (decay time $\sim$ 111.3 days), decays into stable ^{56}Fe. During each of these decays, γ-rays with energies of few 100 keV are emitted. Although the surrounding cloud of gas is opaque at first, the expanding cloud becomes increasingly transparent over the course of a few weeks, allowing

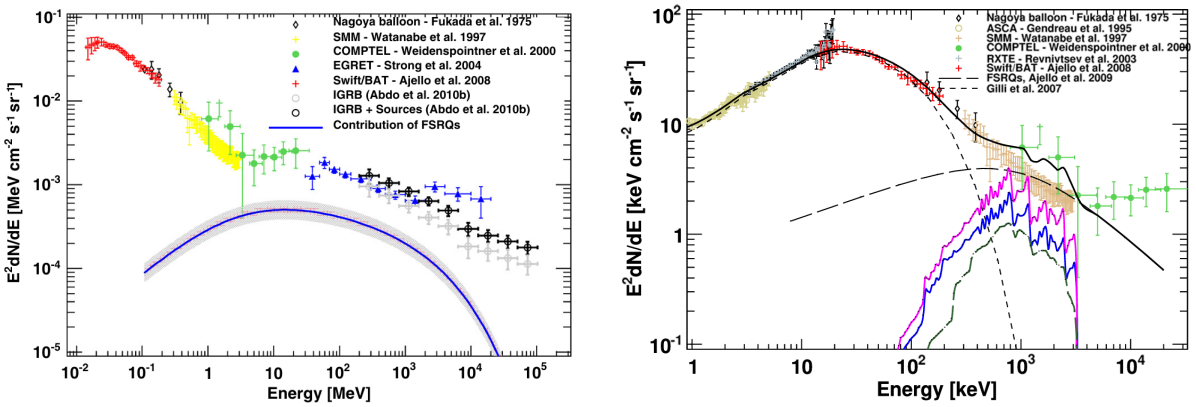

Figure 3.4: *Left*: Contribution of FSRQs (blue line) to the CPB (from Ajello et al. 2012). It is most dominant in the intermediate MeV-range but stretches across several orders of magnitude. *Right*: Upper limits of several models for the SN Ia rate (magenta, blue, and green line) (from Ruiz-Lapuente et al. 2016). Their contribution is more limited and is only significant for low MeV-energies.

more and more γ-rays to escape. Further, Compton scattering leads to a continuum of secondary radiation ranging from keV- to MeV-energies (Diehl et al. 2014).

γ-Rays

This part of the CGB ($20\,\mathrm{MeV} - 5\,\mathrm{GeV}$) was believed to be dominated by blazars making up about 50 % and radio galaxies as well as SFGs (each making up about 20 %). Thus, being close to explaining the complete background (Inoue 2014). Later studies revealed that the contribution of galaxies cannot be more than in the single digit percentages (Fukazawa et al. 2022: Ajello et al. 2020: Chen & Totani 2025).

FSRQs and BL Lacertae objects (BL Lacs), another type of blazar, are co-dominant. The key difference between BL Lacs and FSRQs are the optical emission lines, which are very weak for BL Lacs and not as strong and broad as it is the case for FSRQs.

In FSRQs, UV-photons, originally produced by the disk around the quasar, and diffuse IR-light, originating from the torus around the quasar, interact with the jet of charged particles. By inverse Compton scattering, these photons will be upscattered to higher energies, leading to γ-emission. A schematic illustration of that process is shown in Fig. 3.5. As the sources of these seed photons lie outside of the jet, this mechanism is called External radiation Compton (ERC) process (Madejski & Sikora 2016).

This part of the CPB corresponds to BBs 21 – 24.

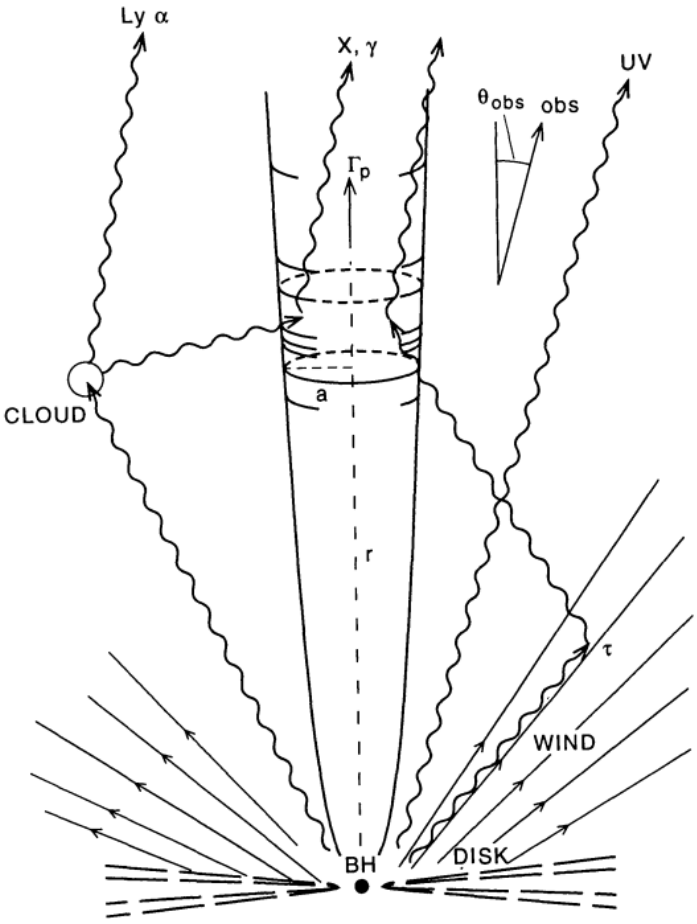

Figure 3.5: Schematic illustration of the External radiation Compton (ERC) process. IR- and UV-photons from the disk and cloud are upscattered by the jet, leading to γ-ray emission (from Sikora et al. 1994).

Very High Energies (VHE)

The composition of the last four BBs (25 – 28), corresponding to the VHE-range ($E > 5\,\mathrm{GeV}$), is relatively simple as their sources are purely BL Lacs (see Fig. 3.6). Their emission mechanism is quite similar to the one in FSRQs. However, since the UV- and optical lines are weak or even nonexistent for blazars, there is likely no significant thermal radiation originating in the disk. Therefore, there cannot be any external photons leading to γ-emission. Instead, synchrotron emission from the jet itself is the main source of γ-ray photons. Because of the origin of the photons, this mechanism is called synchrotron self-Compton scattering (Madejski & Sikora 2016).

For energies beyond 300 GeV, the intensity of the CPB is slowly cut off (Ajello et al. 2015), which can also be seen in Fig. 3.6. The reason for that is the high cross section between photons of those energies with photons making up the CIB, leading to pair production.

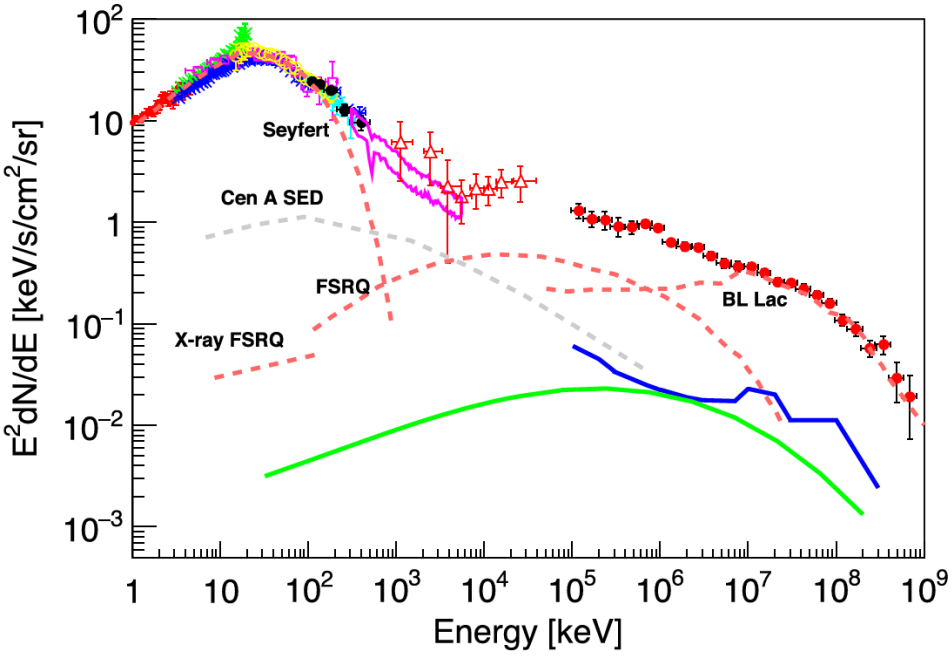

Figure 3.6: Compilation of the CPB from 1 keV to 1 TeV. Different sources and their respective contribution are included as well (from Fukazawa et al. 2022). For the highest energies (> 1 GeV), the CPB is completely dominated by BL Lac objects.

BB	Frequency / wavelength / energy	Sources	Composition
1	37 MHz	Galaxies &	50 % Galaxies &
2	295 MHz	AGNs	50 % AGNs
3	160 GHz	surface of last scattering	CMB
4	264 µm	Stars &	
5	74.4 µm	Galaxies,	100 % Galaxies
6	25.1 µm	heated dust	
7	4.09 µm	Stars &	
8	924 nm	Galaxies,	100 % Galaxies
9	271 nm	direct light	
10	57.9 nm	Galaxies & Quasars	redshift-dependent
11	13.1 nm	purely	100 %
12	3.22 nm	Quasars	Quasars
13	767 eV	mainly Quasars,	25 % Galaxies + 75 % Quasars
14	3.01 keV	in part Galaxies	10 % Galaxies + 90 % Quasars
15	11.8 keV	purely	100 %
16	39.6 keV	Quasars	Quasars
17	134 keV	Quasars &	10 % FSRQs + 90 % Quasars
18	536 keV	FSRQs	50 % FSRQs + 50 % Quasars
19	2.10 MeV	FSRQs &	25 % SNe + 75 % FSRQs
20	9.91 MeV	SNe Ia	25 % SNe + 75 % FSRQs
21	39.0 MeV		2/3 FSRQs + 1/3 BL Lacs
22	132 MeV	FSRQs &	3/5 FSRQs + 2/5 BL Lacs
23	481 MeV	BL Lacs	1/2 FSRQs + 1/2 BL Lacs
24	1.81 GeV		2/5 FSRQs + 3/5 BL Lacs
25	6.70 GeV		
26	23.4 GeV	purely	100 %
27	71.8 GeV	BL Lacs	BL Lacs
28	236 GeV		

Table 3.1: Parametrization of 28 Blackbodies, each expressed in a suitable physical quantity (energy, frequency, or wavelength), along with their sources and model contribution (Aird et al. 2015: Ajello et al. 2009, 2012, 2014: Fukazawa et al. 2022: Gruppioni et al. 2013: Helgason et al. 2012: Khaire & Srianand 2019: Mancuso et al. 2015: Marcotulli et al. 2022: Palicio, P. A. et al. 2024: Ruiz-Lapuente et al. 2016: Shen et al. 2020: Tompkins et al. 2023: Yuan et al. 2017).

Chapter 4

Redshift Evolution of the Photon Background

To model the evolution of the CPB with redshift, one needs to account for two different effects. On the one hand, there is the effect of redshift itself: The wavelength of light, that traveled through space, has been gradually stretched by the expansion of the Universe. On the other hand, the sources, whose light make up the CPB at specific energy ranges, change in their abundance throughout the history of the Universe and, therefore, their luminosity changes as well.

Former effect is modeled by stretching each BB by a factor of $(1+z)$ to higher energies. For the latter effect, different luminosity functions of the various source types need to be investigated.

4.1 Luminosity function

In general, the luminosity function returns the number of sources per volume and per luminosity interval $[L, \mathrm{d}L]$. A typical parametrization of a luminosity function is a smooth double-power law

$$\phi(L) = \frac{\phi^*}{\left(\frac{L}{L^*}\right)^{\gamma_1} + \left(\frac{L}{L^*}\right)^{\gamma_2}}, \tag{4.1}$$

which is often used for AGNs, such as quasars and blazars (Ajello et al. 2009, 2012, 2014). The four parameters are the normalization ϕ^*, the break-luminosity L^*, and the faint-end and bright-end slope γ_1 and γ_2.

Another often used parametrization is the Schechter Function, which only uses the three parameters ϕ^*, L^*, and α. It is defined as (Schechter 1976):

$$\phi(L) = \phi^* \left(\frac{L}{L^*}\right)^{\alpha} \exp\left(-\frac{L}{L^*}\right). \tag{4.2}$$

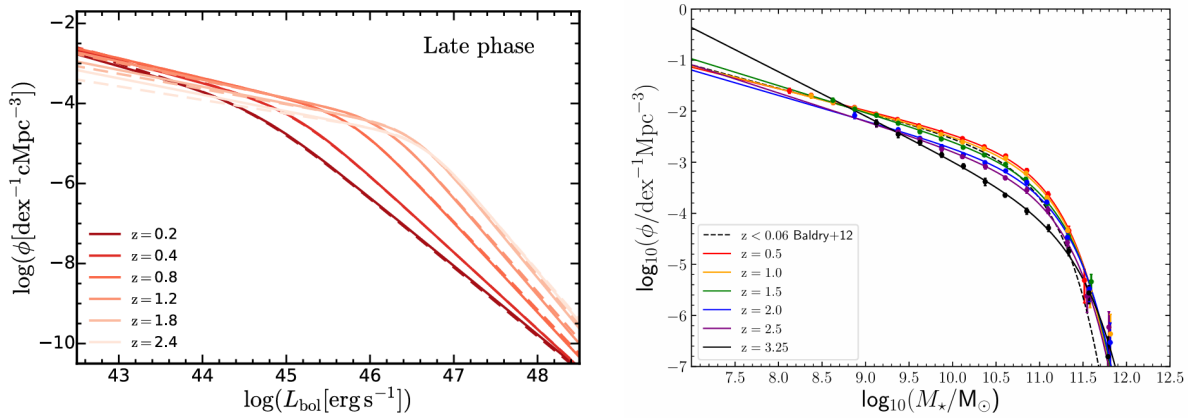

Figure 4.1: *Left*: The bolometric luminosity function of quasars which is modeled by a smooth double-power law shown for different redshifts (from Shen et al. 2020). *Right*: The galaxy stellar mass function which is modeled by a Schechter function shown for different redshifts (from McLeod et al. 2021).

In Fig. 4.1 the use of both function is shown, where, for different redshifts, a smooth double-power law models the luminosity function of quasars in the left panel, and a Schechter function models the galaxy stellar mass function in the right panel.

With the integration

$$L_{\text{total}} = \int_{L_{\text{min}}}^{L_{\text{max}}} L\,\phi(L)\,\mathrm{d}L \tag{4.3}$$

it is possible to calculate the total luminosity L_{total} of a given source type. The big advantage of the Schechter function lies in the integration given in Eq. 4.3. Setting the lower and upper integration limits L_{min} and L_{max}, to 0 and ∞, respectively, leads to an easy expression for L_{total}:

$$L_{\text{total}} = \phi^* L^* \Gamma(\alpha + 2), \tag{4.4}$$

where $\Gamma(x)$ is the Gamma function.

There are certain ways how an evolution parameter can be introduced into the luminosity function. A simple parametrization is the pure density evolution (PDE), in which the luminosity function is just multiplied by an evolution parameter – regardless of the different luminosities:

$$\phi_{\text{PDE}}(L, z) = \phi(L, z = 0) \cdot e(z). \tag{4.5}$$

A similar approach is the pure luminosity evolution (PLE), in which the luminosities themselves undergo an evolution, while the luminosity function remains unchanged:

$$\phi_{\text{PLE}}(L, z) = \phi(L/e(z), z = 0). \tag{4.6}$$

A more sophisticated approach lies in the luminosity-dependent density evolution (LDDE). This parametrization introduces an evolution parameter that also includes a

dependency on the luminosity; often times this is achieved by allowing each parameter of the evolution function to vary in some way as a function of luminosity:

$$\phi_{\mathrm{LDDE}}(L, z) = \phi(L, z = 0) \cdot e(L, z). \tag{4.7}$$

Additionally, there are approaches, that cannot be strictly categorized into one of these three categories. Alternatively, one could simply allow each of the parameters of the original luminosity function to vary in some way.

4.2 Evolution of Photon Background Components

4.2.1 Cosmic Radio Background

Evolution of galaxies

The synchrotron luminosity of galaxies

$$L_{\mathrm{synchr}} = 1.9 \times 10^{28} \left(\frac{\mathrm{SFR}}{M_{\odot}\mathrm{yr}^{-1}}\right) \left(\frac{\nu}{\mathrm{GHZ}}\right)^{-0.85} \left[1 + \left(\frac{\nu}{20\,\mathrm{GHz}}\right)^{0.5}\right]^{-1} \mathrm{erg\,s^{-1}\,Hz^{-1}} \tag{4.8}$$

as well as the luminosity from free-free emission

$$L_{\mathrm{ff}} = 3.75 \times 10^{26} \left(\frac{\mathrm{SFR}}{M_{\odot}\,\mathrm{yr}^{-1}}\right) \left(\frac{T}{10^4\,\mathrm{K}}\right)^{-0.5} g(\nu, T)\, e^{-h\nu/kT} \quad \mathrm{erg\,s^{-1}\,Hz^{-1}} \tag{4.9}$$

with

$$g(\nu, T) = 3.96 \left[1 + \ln\left(\frac{T}{10^4\,\mathrm{K}}\right) - \ln\left(\frac{\nu}{\mathrm{GHz}}\right)\right] \tag{4.10}$$

are directly proportional to the SFR, meaning to receive the relative change with redshift, it is sufficient to focus on only the SFR (Mancuso et al. 2015).

The SFR is modeled by a Schechter-like function

$$\phi_{\mathrm{SFR}}(z) = \phi(z) \left[\frac{\mathrm{SFR}}{\mathrm{SFR}_*(z)}\right]^{1-\alpha(z)} \exp\left(-\left[\frac{\mathrm{SFR}}{\mathrm{SFR}_*(z)}\right]^{\omega(z)}\right), \tag{4.11}$$

where $\phi(z)$ is the normalization, $\mathrm{SFR}(z)$ the break-SFR, $\alpha(z)$ is a measure for the faint-end slope, and $\omega(z)$ a cutoff parameter. The four parameters themselves are functions of redshift. Using observational data in the ultraviolet (UV) and infrared (IR) bands, the luminosity functions at different redshifts can be constructed. Since UV radiation traces hot, young stars, and IR emission originates from dust-reprocessed starlight, these wavelengths provide insight into both unobscured and obscured star formation. It is therefore possible to derive a SFR function for different redshifts, described by the combination of

the four parameters. The redshift evolution of these parameters can be approximated as a third-order polynomial in χ, leading to (Aversa et al. 2015):

$$\log\left[\phi(z)\right] = -2.4 - 2.3\chi + 6.2\chi^2 - 4.9\chi^3, \tag{4.12}$$

$$\log\left[\mathrm{SFR}_*(\mathrm{z})\right] = 1.1 + 3.2\chi - 1.4\chi^2 - 2.1\chi^3, \tag{4.13}$$

$$\alpha(z) = 1.2 + 0.5\chi - 0.5\chi^2 + 0.2\chi^3, \tag{4.14}$$

$$\omega(z) = 0.7 - 0.15\chi + 0.16\chi^2 + 0.01\chi^3, \tag{4.15}$$

with $\chi = \log(1+z)$. These parametrizations are motivated by practical reasons, as the evolution of each parameter is perhaps more complex than described by these third order polynomials (Mancuso et al. 2015). Aversa et al. (2015) did not include errors for these parameters, instead only stating that the tolerance on the parameters is less than 10 %.

Evolution of AGNs

The other half of the CRB-contribution will be modeled by a combination of a pure luminosity and pure density evolution of AGNs (Yuan et al. 2017):

$$\phi(L, z) = e_1(z)\, \rho(L/e_2(z), z = 0), \tag{4.16}$$

which includes two evolution functions $e_1(z)$, $e_2(z)$ and the radio luminosity function (RLF) $\rho(L, z)$. The RLF for AGNs is also described by a Schechter function, in which another parameter was added to the exponential term:

$$\rho(L, z) = \phi_1 \left(\frac{L}{L_*}\right)^{-\beta} \exp\left[-\left(\frac{L}{L_*}\right)^{\gamma}\right], \tag{4.17}$$

where ϕ_1 is the normalization parameter, L_* the break-luminosity, β the faint-end slope, and γ the bright-end cutoff.

The density evolution

$$e_1(z) = p_0 \left[\left(\frac{1+z_c}{1+z}\right)^{p_1} + \left(\frac{1+z_c}{1+z}\right)^{p_2}\right]^{-1} \tag{4.18}$$

includes the free parameters p_1, p_2, and z_c in addition to the normalization parameter

$$p_0 = \left[(1+z_c)^{p_1} + (1+z_c)^{p_2}\right], \tag{4.19}$$

which ensures $e_1(z = 0) = 1$. The luminosity evolution is modeled by a modified power-law of the form

$$e_2(z) = (1+z)^{k_1} \exp\left(-\frac{z^2}{2k_2^2}\right), \tag{4.20}$$

where k_1, k_2 are free parameters. The values for each parameter (including errors) are given in Tab. 1 in the Appendix. The density and luminosity evolutions are shown as a function of redshift in Fig. 4.2 (left) and lead to a luminosity-dependent evolution of the luminosity functions, as shown in Fig. 4.2 (right).

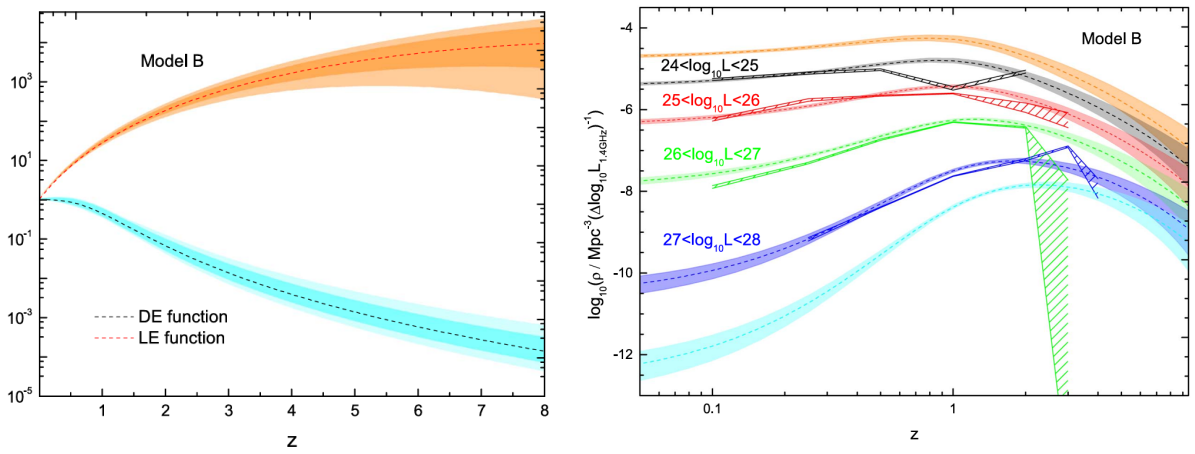

Figure 4.2: *Left*: Density evolution (blue) and luminosity evolution (orange) for AGNs in the radio regime. *Right*: Evolution of AGN radio luminosity functions sorted by brightness (from Yuan et al. 2017).

4.2.2 Cosmic Microwave Background

A slight deviation from the general approach is the redshift evolution of the CMB, that can easily be modeled by increasing the temperature of that BB by $(1 + z)$:

$$T_{\mathrm{CMB}}(z) = T^0_{\mathrm{CMB}} \cdot (1 + z), \tag{4.21}$$

where the temperature of the CMB for the local Universe is $T^0_{\mathrm{CMB}} = 2.7255\,\mathrm{K}$ (Fixsen 2009). This, by the nature of the BB spectrum, will also lead to an increased flux level, while simultaneously shifting the spectrum to higher energies for the CMB, even though the multiplicative amplitude is fixed to 1,.

4.2.3 Cosmic Infrared Background

The luminosity density of the CIB can be estimated by a triple broken-power law (Gruppioni et al. 2013):

$$\rho(z) \propto \begin{cases} z^{+3.0\pm0.2}, & z \leq 1.1 \\ z^{-0.3\pm0.1}, & 1.1 < z \leq 2.8 \\ z^{-6.0\pm0.9}, & z > 2.8 \end{cases}. \tag{4.22}$$

This corresponds to a sharp increase up to $z = 1.1$, where the luminosity density reaches a plateau until $z = 2.8$. After that, the CIB experiences a sharp decline in its brightness.

4.2.4 Cosmic Optical Background

The parametrization for the COB, again, uses a Schechter function, but this time given as a function of the absolute brightness M:

$$\phi(M) = 0.4 \ln(10)\, \phi^* \left(10^{0.4(M^*-M)}\right)^{\alpha+1} \cdot \exp\left(-10^{0.4(M^*-M)}\right). \tag{4.23}$$

This equation includes three parameters, all of which are themselves functions of z:
The normalization

$$\phi^*(z) = \phi_0^* \exp(-p(z - z_0)), \tag{4.24}$$

the characteristic absolute brightness

$$M^*(z) = M_0^* - 2.5 \log[(1 + (z - z_0))^q], \tag{4.25}$$

and the faint-end slope

$$\alpha(z) = \alpha_0 \left(\frac{z}{z_1}\right)^r, \tag{4.26}$$

where p, q, r are the best-fit exponents, ϕ_0^*, M_0^*, α_0 normalizations, and z_0, z_1 cut-off redshifts (Helgason et al. 2012).

Because of the mathematical structure of the Schechter function, integration leads – as described above – to the simple expression:

$$L_{\text{total}} = \int_0^\infty M\, \phi(M)\, \mathrm{d}M = \int_0^\infty L\, \phi(L)\, \mathrm{d}L = \phi^*\, L^*\, \Gamma(\alpha + 2), \tag{4.27}$$

where $\Gamma(x)$ is the Gamma function.
As luminosity L is related to the absolute brightness M via

$$L = L_0 \cdot 10^{-\frac{M}{2.5}}, \tag{4.28}$$

with $L_0 = 3.0128 \times 10^{35}\,\mathrm{erg\,s^{-1}}$, this expression allows for a direct computation of L^* from M^*. The parameter values for different filterss corresponding to different wavelengths can be found in Tab. 2 of the Appendix.

4.2.5 Cosmic UV-Background

Quasar contribution

Quasi stellar objects (QSOs, short quasars) undergo a surprisingly uniform evolution for different frequencies. The intensity spectrum of a quasar is usually best described by a power law $I \propto \nu^{-\alpha}$, where α is some non-negative constant and can be modified for higher energies to include an exponential term. A typical value is $\alpha \approx 1.8$, but can deviate for lower energies (Khaire & Srianand 2019). This has the consequence that – if the evolution

of a quasar is known for one wavelength – one can estimate its luminosity for a wide energy range.

Given that their luminosity evolution for $\lambda = 1000\,\text{Å}$ can be modeled by

$$e_{\text{QSO}}(z) = (1+z)^{5.9} \cdot \frac{\exp(-0.36z)}{\exp(2.2z) + 25.1} \tag{4.29}$$

and the relation between two different frequencies is a non-redshift dependent constant, the luminosity evolution of QSOs holds true for the full UV-range.

Contributions from Galaxies

A similar observation – albeit much more limited – can be done for the contributions from galaxies to the UV-spectrum. Due to the absorption of hydrogen and helium, the intensity spectrum can only be approximated by a power law for energies between $E = 13.6{-}54.4\,\text{eV}$ ($228\,\text{Å}$ and $912\,\text{Å}$). The reason for that lies in the escape fraction f_{esc} of hydrogen-ionizing photons from galaxies. Within the specified energy range, f_{esc} depends solely on redshift and remains constant throughout the frequency range. f_{esc} is shown in the left panel of Fig. 4.3 and is modeled by

$$f_{\text{esc}}(z) = \begin{cases} \frac{10^{-5}}{6.5\cdot 10^{-5} + \exp(-2.4z)} & \text{for } 228\,\text{Å} < \lambda < 912\,\text{Å} \\ 0 & \text{for } \lambda < 228\,\text{Å} \end{cases}. \tag{4.30}$$

However, if the energy is large enough to ionize helium, whose threshold is reached at $E = 54.4\,\text{eV}$ ($\lambda = 228\,\text{Å}$), the escape rate suddenly drops to 0. Thus, for those energies there are only quasar contributions, as light of such energy is not able to escape the galaxies (Khaire & Srianand 2019).

This results in an evolution function for galaxies in the UV that is described by the combined evolution of the escape fraction and luminosity:

$$e_{\text{gal}}^{\text{UV}} = f_{\text{esc}}(z)\,\frac{3.02 + 13.12z}{1 + (z/2.44)^{3.02}}. \tag{4.31}$$

The combined model for the CUB leads to an interesting evolution, in which quasars increase in their luminosity until $z \sim 2.0$, at which point these objects have reached their maximum contribution. Increasing in their luminosity with redshift, galaxies and QSOs contribution in equal parts at $z \sim 3.0$, after which galaxies are the most dominant contributors (see right panel of Fig. 4.3).

4.2.6 Cosmic X-Ray Background

Quasar contribution

As quasars are emitting radiation not just in the X-ray, but also in the infrared, optical, and UV regime, one needs to incorporate a bolometric correction, which relates the lu-

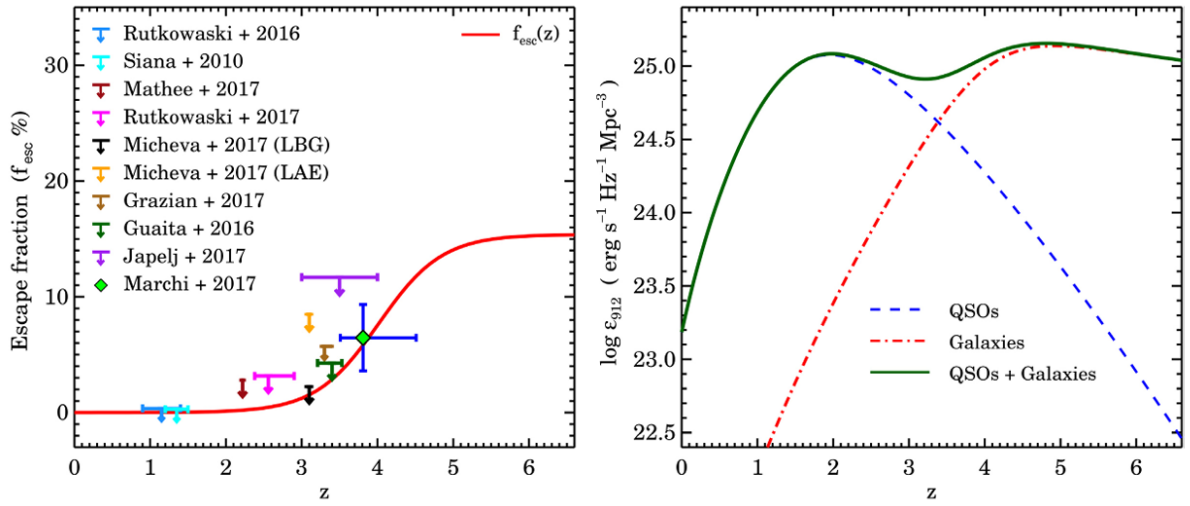

Figure 4.3: *Left:* Escape fraction f_{esc} of UV-galaxies. *Right:* Redshift evolution of the CPB at $\lambda = 912\,\text{Å}$ modeled by a combination of contributions from quasars and galaxies (from Khaire & Srianand 2019).

minosity in a given energy band L_{band} with the total luminosity across all energies L_{bol}. This can be modeled by a smooth double power law:

$$\frac{L_{\mathrm{bol}}}{L_{\mathrm{band}}} = m_1 \left(\frac{L_{\mathrm{bol}}}{10^{10} L_\odot}\right)^{k_1} + m_2 \left(\frac{L_{\mathrm{bol}}}{10^{10} L_\odot}\right)^{k_2}, \tag{4.32}$$

which includes the best fitting parameters m_1, m_2, k_1, and k_2 (Shen et al. 2020), whose values can be found in Tab. 4.4 in the Appendix. The bolometric corrections for different wavelength bands are shown in Fig. 4.4, in which the Soft X-Ray (orange) and Hard X-Ray (green) bands are of interest.

The bolometric luminosity function itself, is also modeled by a smooth double power law

$$\phi(L) = \frac{\phi_*}{\left(\frac{L}{L_*}\right)^{\gamma_1} + \left(\frac{L}{L_*}\right)^{\gamma_2}} \tag{4.33}$$

with a normalization ϕ_*, break-luminosity L_* as well as the faint-end and bright-end slope γ_1 and γ_2.

However, too large values of the faint-end slope ($\gamma_1 > 1$) or too small values of the bright-end slope ($\gamma_2 < 1$) lead to divergences in the total luminosity when integrating, resulting in a nonphysical model (see Fig. 4.5). This leads to the "Global fit B", in which the four parameters were allowed to vary in some pre-determined way, in which only a negative evolution of γ_1 with redshift was possible:

$$\gamma_1(z) = a_0 \left(\frac{1+z}{1+z_{\mathrm{ref}}}\right), \tag{4.34}$$

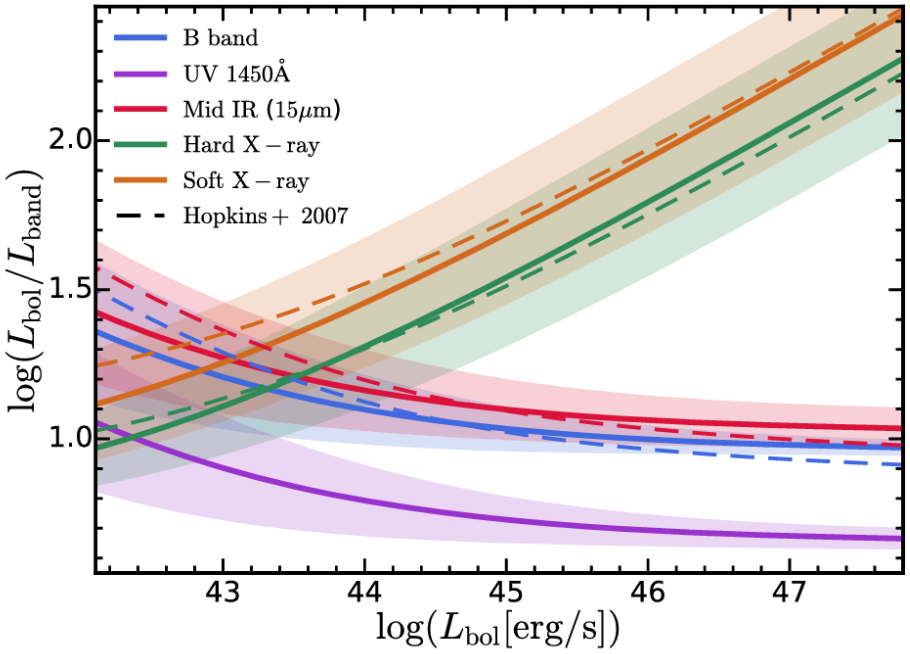

Figure 4.4: The bolometric corrections of the quasar luminosity function for different energy ranges (from Shen et al. 2020).

$$\gamma_2(z) = \frac{2b_0}{\left(\frac{1+z}{1+z_{\mathrm{ref}}}\right)^{b_1} + \left(\frac{1+z}{1+z_{\mathrm{ref}}}\right)^{b_2}}, \tag{4.35}$$

$$\log(L_*(z)) = \frac{2c_0}{\left(\frac{1+z}{1+z_{\mathrm{ref}}}\right)^{c_1} + \left(\frac{1+z}{1+z_{\mathrm{ref}}}\right)^{c_2}}, \tag{4.36}$$

$$\log(\phi_*(z)) = d_0 + d_1 \cdot (1+z), \tag{4.37}$$

where z_{ref} is set to 2.0. Their evolution can be seen in Fig. 4.5 ("Global fit B" in pink). Numerical values for each parametrization can be found in Tab. 4 in the Appendix.

Contributions from Galaxies

Besides AGNs, the are also contributions from, mostly X-ray binaries, contributing to the CXB. The corresponding luminosity function of galaxies in the X-ray can be described by a Schechter function:

$$\phi(L,z) = A \left(\frac{L}{L_*(z)}\right)^{\alpha} \exp\left(-\frac{L}{L_*(z)}\right), \tag{4.38}$$

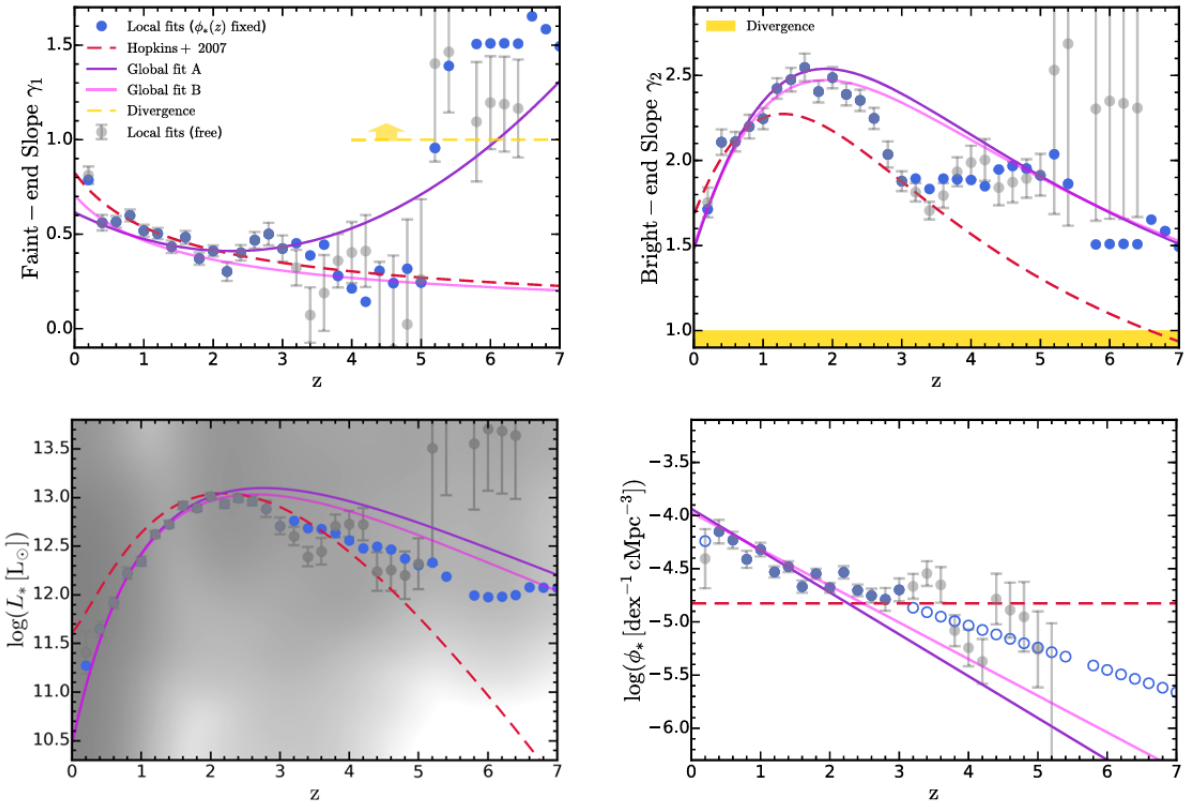

Figure 4.5: Evolution of the four parameters γ_1, γ_2, $\log(L_*)$, $\log(\phi_*)$ with redshift. The "Global fit B" model was used as it did not lead to divergences (from Shen et al. 2020).

where $L_*(z)$ is the only parameter changing with redshift (Aird et al. 2015). It is assumed to change linearly up to a cut-off redshift z_c, at which point it stays constant:

$$\log\left(L_*(z)\right) = \begin{cases} \log L_0 + \beta \log\left(1+z\right) & \text{for } z < z_c \\ \log L_0 + \beta \log\left(1+z\right) & \text{for } z \geq z_c \end{cases}. \tag{4.39}$$

In total, this includes five free parameters: the normalization A, the faint-end slope α, the characteristic luminosity L_0, the "luminosity evolution slope" β, and the cut-off redshift z_c, whose values are shown in Tab. 5. This model is perhaps not complex enough to grasp the full evolution of the emission from galaxies in the X-ray regime. The rising characteristic luminosity results into an increased luminosity for low redshifts, but does not model any evolution beyond the cut-off redshift z_c, which is possibly adequate to some redshift, but not on the scales up to $z = 10.0$.

4.2.7 Cosmic γ-Ray Background

FSRQs

The luminosity function of FSRQs can be assumed to be described by a smooth double-power law of the form

$$\phi(L, z = 0) = A \left[\left(\frac{L}{L_*} \right)^{\gamma_1} + \left(\frac{L}{L_*} \right)^{\gamma_2} \right]^{-1}. \tag{4.40}$$

The redshift evolution is described by a PLE (Marcotulli et al. 2022). This means that the four parameters (normalization A, break-luminosity L_*, faint- and bright-end slope γ_1, γ_2) remain unchanged. Instead the luminosity itself undergoes an evolution, which results in

$$\phi(L, z) = \phi(L/e(z), z = 0) \tag{4.41}$$

with the evolutionary term

$$e(z) = (1 + z)^k \mathrm{e}^{z/\xi}, \tag{4.42}$$

where k is the redshift index and ξ the evolutionary cutoff term. This evolutionary term is used only up to an energy of about 200 keV; for higher energies the evolutionary term is modified and reads

$$e(z) = (1 + z)^{k+\gamma z}. \tag{4.43}$$

Here, γ takes the role of introducing a cutoff (Ajello et al. 2009). The corresponding numerical values can be found in Tab. 6, and 7 in the Appendix, respectively.

Type Ia Supernovae

The rate of SNe Ia is closely connected to the SFR. But since stars first have to go through a substantial part of their life cycle, it lags behind the SFR. This effect can be modeled by a convolution between the SFR and the delay time distribution (DTD) function:

$$R_{\mathrm{Ia}} = k_\alpha A \int_{\tau_{\min}}^{\tau_{\max}} \mathrm{SFR}(t - \tau)\, \mathrm{DTD}(\tau)\, \mathrm{d}\tau. \tag{4.44}$$

The convolution is further modified by k_α, which is the number of stars per unit mass in a stellar generation, and A, which is the fraction of star systems resulting into a SN Ia. The integration limits $\tau_{\min}$, $\tau_{\max}$ are the minimum and maximum time spans after the star's formation, in which the supernova explosion can happen (Palicio, P. A. et al. 2024). The DTD can be approximated by many functions. One that is often used is a simple power law

$$\mathrm{DTD} \propto t^{-1}. \tag{4.45}$$

The SN Ia-rate for different DTD-models is shown in Fig. 4.6. Here, the "Mix"-model is used.

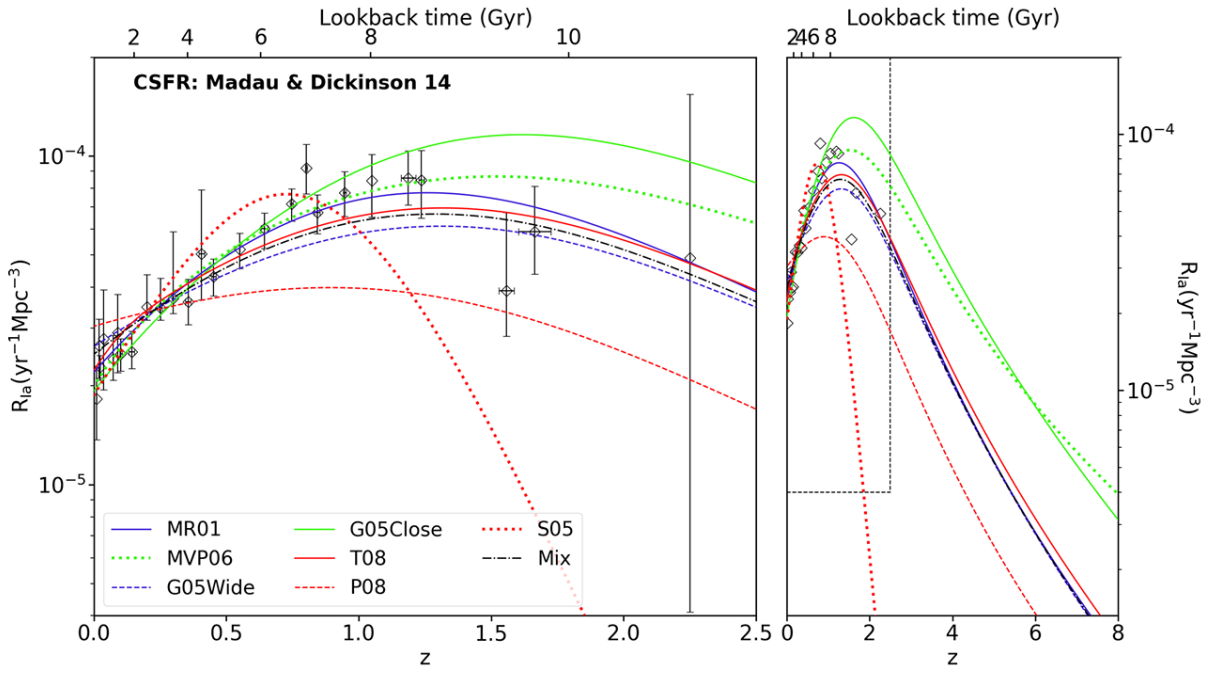

Figure 4.6: The rate of SNe Ia as a function of redshift for different DTD-models. All models rely on the SFR derived in Madau & Dickinson (2014). Here, the "Mix" model (black dotted line) was used for the evolution of SNe Ia (from Palicio, P. A. et al. 2024).

BL Lacs

BL Lacs undergo a bit of an unusual evolution. This subclass of blazars can also be modeled by a smooth double power law. The evolution is best described by an LDDE, meaning the luminosity function is multiplied by an evolution parameter that strongly depends on the luminosity of the source (Ajello et al. 2014):

$$\phi(L, z) = \phi(L, z = 0) \cdot e(L, z), \tag{4.46}$$

where

$$e(L, z) = \left[\left(\frac{1+z}{1+z_c(L)} \right)^{p_1(L)} + \left(\frac{1+z}{1+z_c(L)} \right)^{p_2} \right] \tag{4.47}$$

with the additional parametrizations:

$$z_c(L) = z_c^* \cdot \left(\frac{L}{10^{48}} \right)^{\alpha}, \tag{4.48}$$

and

$$p_1(L) = p_1^* + \tau \cdot [\log(L) - 46]\,. \tag{4.49}$$

This leads to a total of 9 parameters: the standard parameters for a double power law (A, L_*, γ_1, γ_2) as well as the evolution parameters (z_c^*, p_1^*, p_2, τ, α). For numerical values see Tab. 8.

The result of this parametrization is a slight negative evolution of BL Lac objects up to a redshift of ~ 0.5, followed by an increase up to a redshift of ~ 1.5, after which the luminosity decreases again.

4.3 A full model of the Photon Background

Incorporating all of the above parametrization into the model for the CPB leads to an evolution in the relative amplitude, which is the relative change of each BB amplitude relative to redshift 0 (see Fig. 4.7).

The behavior of most BBs is relatively similar to one another. First an increase in their luminosity can be observed up to a redshift of about 2.0, after which their luminosity keeps only decreasing.

However, there are a few BBs revealing a quite unique behavior. First of all, there is BB 3 (orange line in the top plot), which corresponds to the CMB. It stays constant, as its evolution is fully modeled by the increasing temperature of the CMB, which itself leads to an BB increasing in its intensity and a shift to higher energies.

Further, there is BB 10 (teal line in the top plot), whose evolution includes two bumps. The reason for that is the contribution by quasars and galaxies: first bump arises from the maximum in quasar luminosity; the second one is the result of an increasing contribution from galaxies in the X-ray that is negligible for the local Universe (Khaire & Srianand 2019).

In the case of BB 13 and 14 (light blue filled and dotted line in the bottom plot), there seems to be a flattening evolution for high redshifts, which can be explained by the shortcomings of the parametrization modeling the evolution of galaxies, which did not include an eventual decrease with redshift (see Eq. 4.38 and 4.39).

On the higher energetic end, BBs 18 – 20 (dotted and dashed dark blue lines in the bottom plot) show a less dynamic evolution, with a maximum around redshift 5 – much earlier in the history of the Universe than the other components. The reason for that is the slow evolution of FSRQs that dominate these three BBs (Ajello et al. 2012). To some extent, this can also be seen for BB 17 (dark blue filled line), where, for high redshifts, the curve flattens, signaling a dominance by the slow evolving FSRQs as well.

Lastly, the evolution of of the four most-energetic BBs is the most striking with a negative evolution for small redshifts up to about 0.5, after which a slight increase up to about $z \sim 1.5$ sets in with an eventual decrease again. The authors in Ajello et al. (2014) theorize that the evolution of BL Lacs is dominated by two effects: First, there is the initial evolution of these objects starting in the early Universe that peaks around redshift 1.5 and then drops off. The eventual increase for low redshifts can be explained by the relation between FSRQs and BL Lacs. It is theorized that BL Lacs are the final evolutionary stage

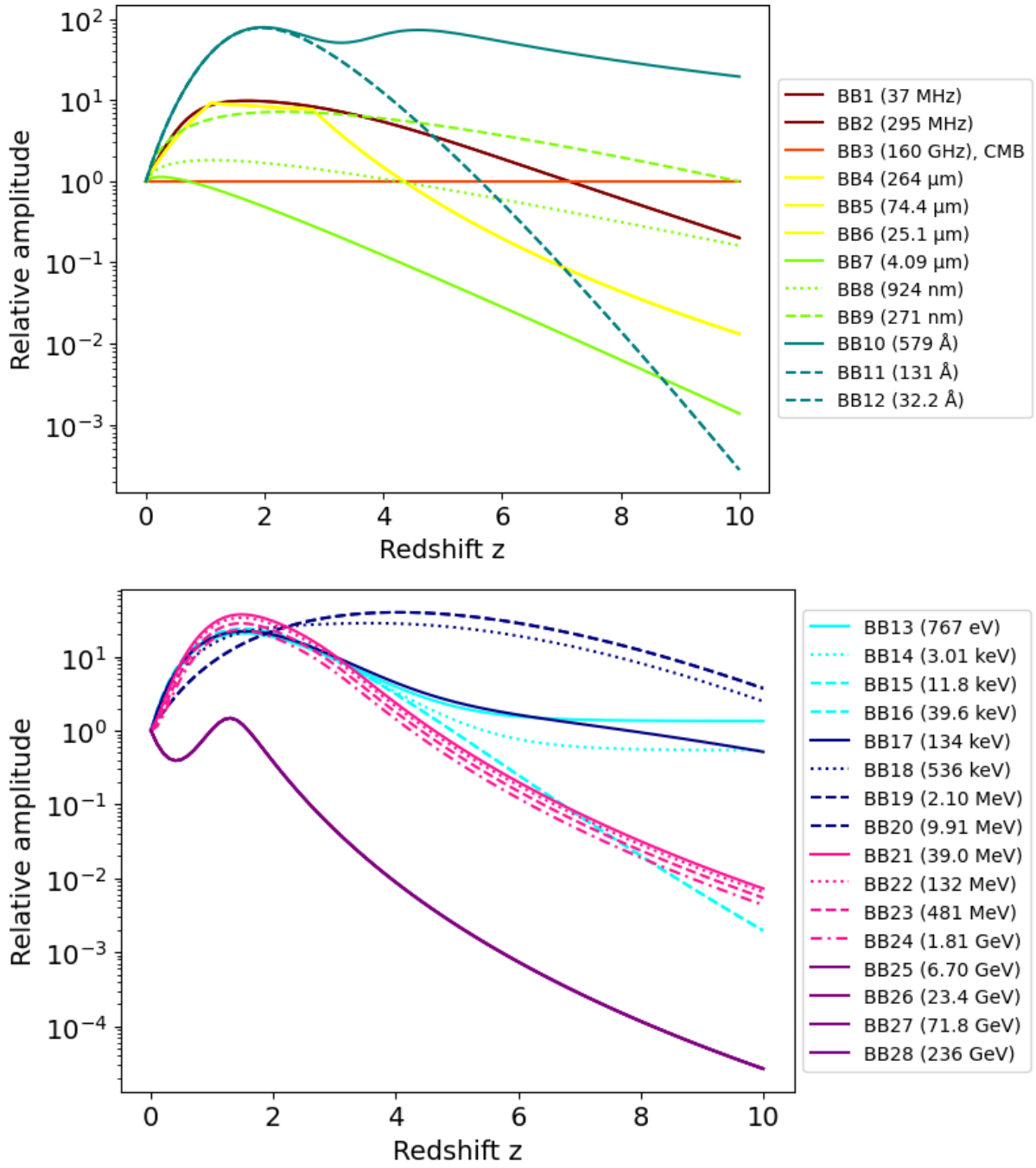

Figure 4.7: Evolution of amplitude relative to redshift 0.0 for the first 12 Blackbodies (top), and for Blackbodies 13 – 28 (bottom).

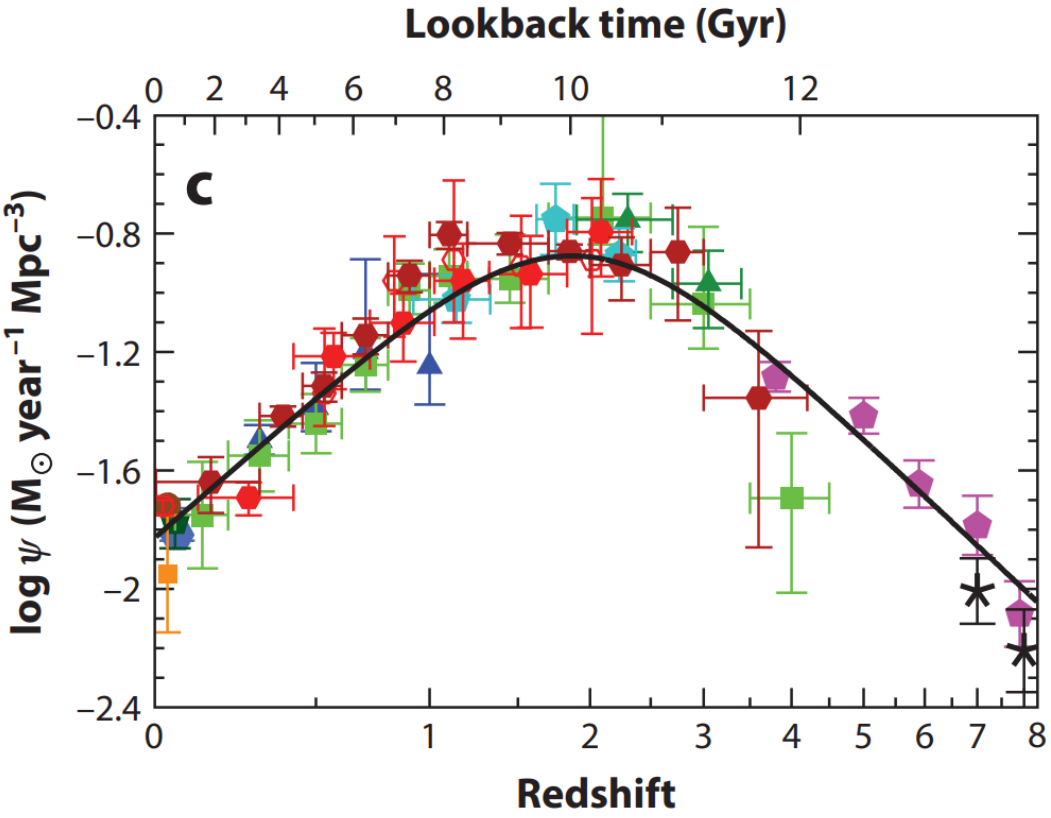

Figure 4.8: SFR as a function of redshift (from Madau & Dickinson 2014). The SFR is steadily increasing up to a redshift of about 2.0, after which it eventually decreases again. Its behavior has a striking similarity with most plots given in Fig. 4.7.

of FSRQs, that emerge when their accretion rate drops. Thus, a decrease in FSRQs will lead to an increasing number of BL Lacs, hence, culminating in another peak presumably still ahead in time.

Nevertheless, for most sources, a striking connection can be made to the Madau-plot, which shows SFR density of the Universe as a function of redshift and shows a similar behavior (see Fig. 4.8). Starting from $z = 0$, the SFR increases up to a redshift of about 2.0, after which it decreases. Since the luminosity evolution of most objects in the Universe is linked to star formation, the CPB will therefore also show a similar trend. Likewise, the positron emissivity as a function of redshift should also follow the SFR density.

Combining these relative amplitudes and the redshift evolution, the CPB can finally be constructed for up to redshift 10.0, some of which are shown in Fig. 4.9 and 4.10. It is noted that beyond redshift 5.0, the luminosity functions become rather uncertain. At redshift 10.0, one would then expect that the CMB completely dominates the spectrum, together with a peak in the UV as well as around MeV (see bottom plot in Fig. 4.10).

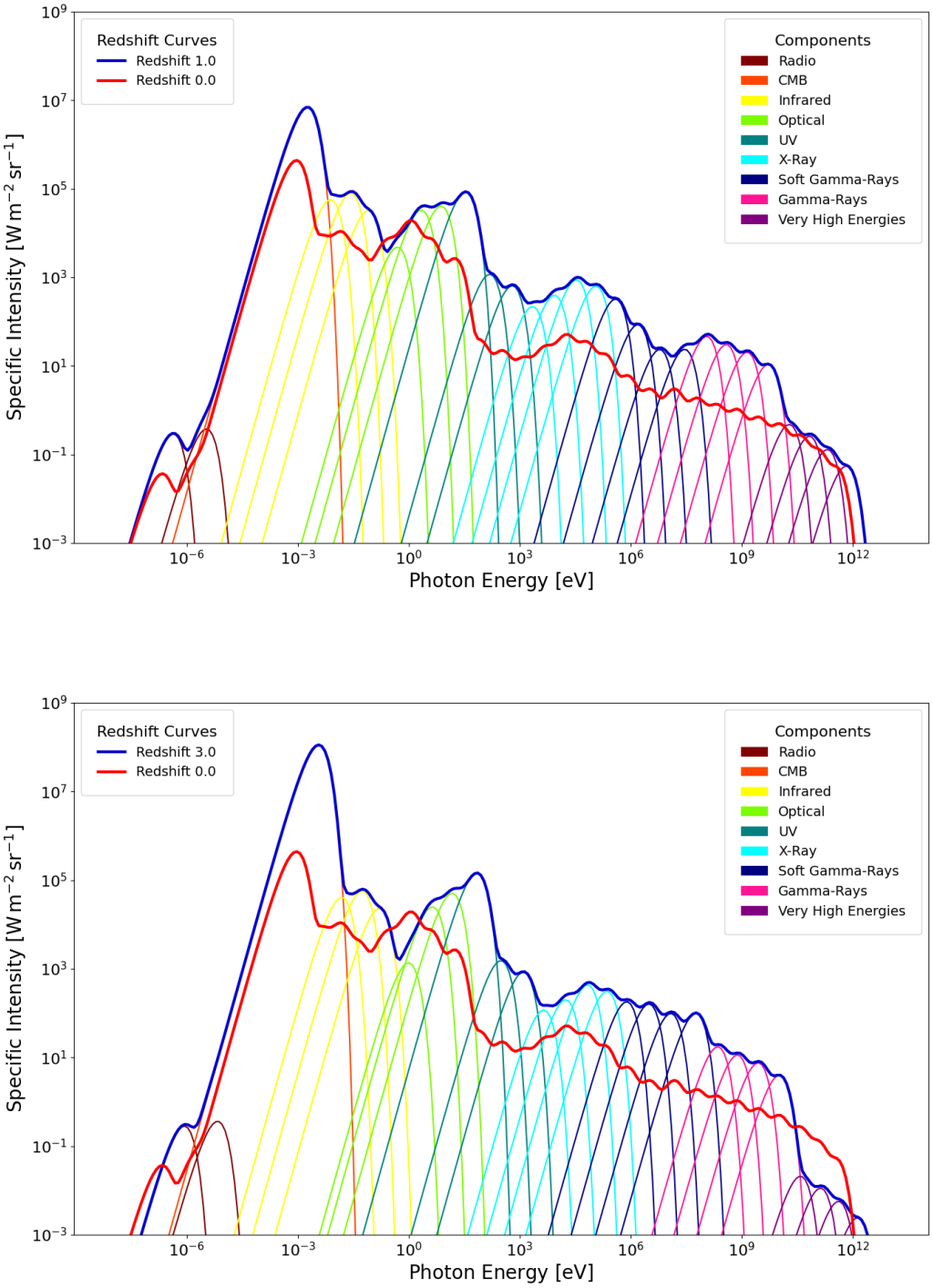

Figure 4.9: Redshift evolution for the CPB for $z = 1.0$ (top), and $z = 3.0$ (bottom).

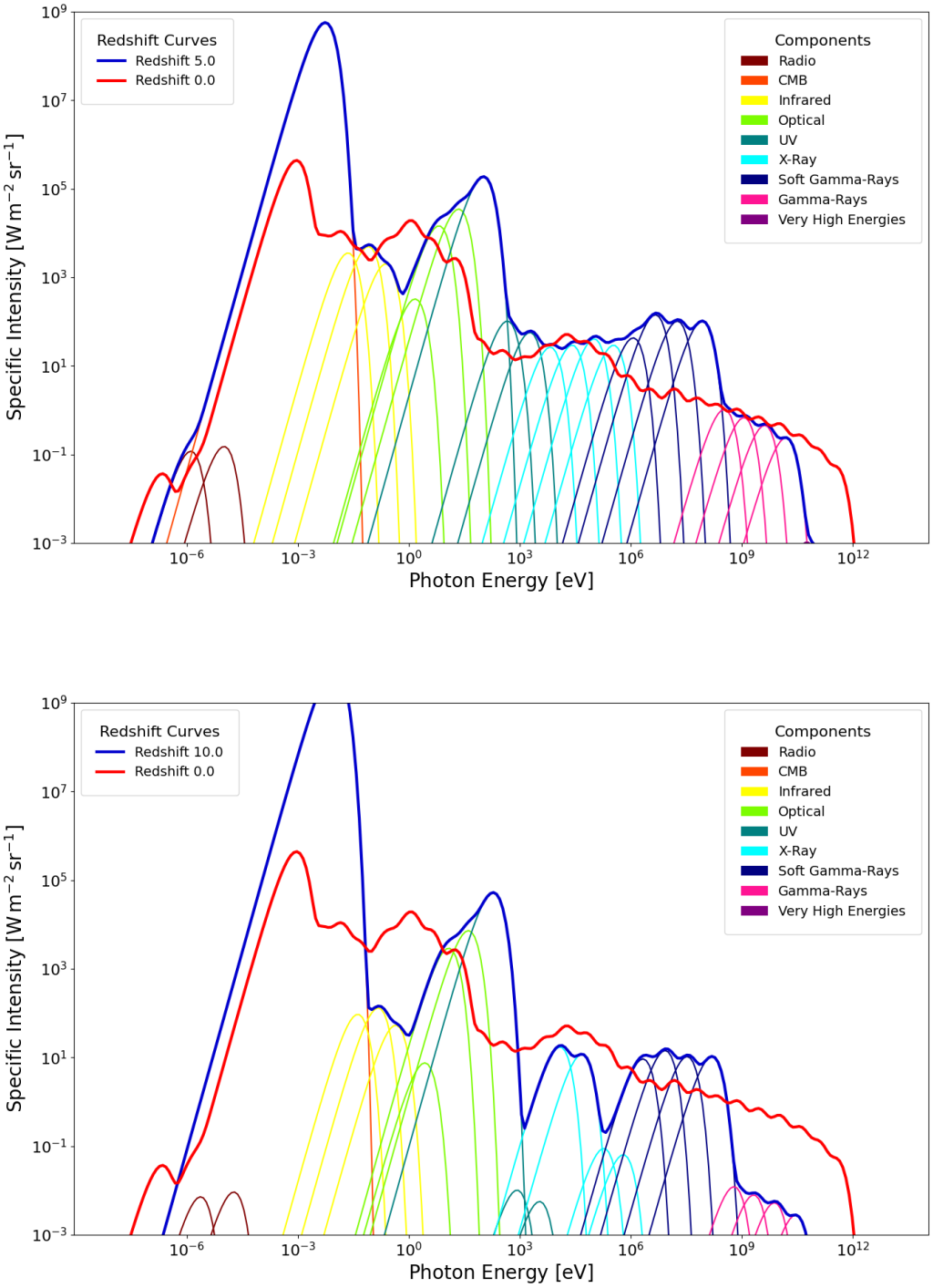

Figure 4.10: Redshift evolution for the CPB for $z = 5.0$ (top), and $z = 10.0$ (bottom).

4.4 Calculating the positron production rate

To determine the positron production rate in a given volume, one needs to integrate the emissivity over the corresponding comoving volume of space; for that, the emissivity $\dot{n}_{\pm}$ is assumed to be constant in the interval of $\Delta z = \pm 0.05$ around the given redshift (see Fig. 4.12).

To do that, the comoving volume in a given redshift bin was computed. The differential comoving volume is defined as (Hogg 2000)

$$\frac{\mathrm{d}V_{\mathrm{com}}}{\mathrm{d}z\,\mathrm{d}\Omega} = \frac{c \cdot D_{\mathrm{com}}^2(z)}{H(z)}, \tag{4.50}$$

where $D_{\mathrm{com}}(z)$ is the comoving distance, which can be derived with

$$D_{\mathrm{com}}(z) = \int_0^z \frac{c}{H(z')} \mathrm{d}z'. \tag{4.51}$$

$H(z)$ is the Hubble parameter, which, in the standard ΛCDM-model, is calculated by

$$H(z) = H_0 \sqrt{\Omega_m (1+z)^3 + \Omega_\Lambda} \tag{4.52}$$

with $H_0 = 67.66\,\frac{\mathrm{km/s}}{\mathrm{Mpc}}$, $\Omega_m = 0.31$, and $\Omega_\Lambda = 0.69$ (Planck Collaboration et al. 2020a). A plot of the differential comoving volume is shown in Fig. 4.11, where a steep increase up to $z \sim 2.0$ can be seen. Therefore, the comoving volume V_{com} can be calculated by integrating over the differential comoving volume:

$$V_{\mathrm{com}}(z) = 4\pi \int_{z_{\mathrm{center}}-\Delta z}^{z_{\mathrm{center}}+\Delta z} \frac{\mathrm{d}V_{\mathrm{com}}}{\mathrm{d}z\,\mathrm{d}\Omega}\,\mathrm{d}z, \tag{4.53}$$

resulting in a spherical shell of changing absolute thickness.

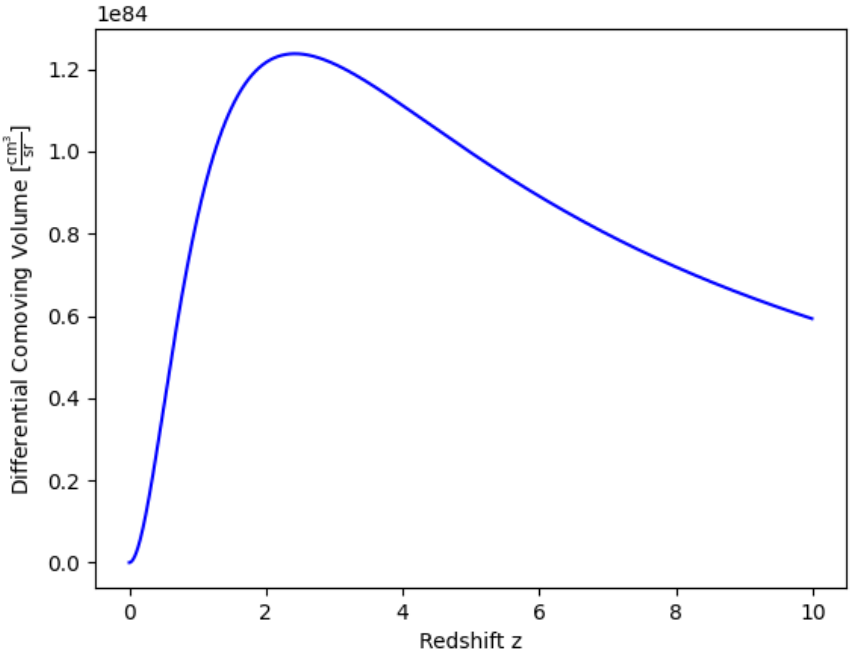

Figure 4.11: Differential comoving volume as a function of redshift.

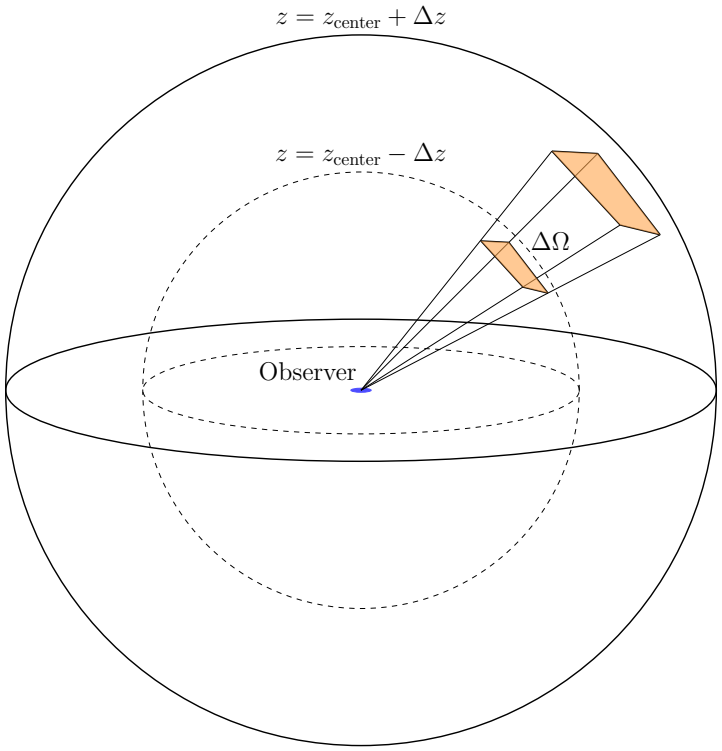

Figure 4.12: Visualization of the comoving volume. The comoving volume of a redshift bin includes the total volume between the inner and outer sphere.

Chapter 5

Results

5.1 Positron Production Rate

The resulting computation of the positron emissivity leads to a spectrum given as a function of the Lorentz factor γ, which can easily be cast into a function of energy. It is thus a differential emissivity, defined as the positron emissivity per eV (see Fig. 5.1). The spectrum shows a general decrease with energy, that is sharply cutoff around $10^{12}\,\mathrm{eV}$. However, there appears to be a slight excess in positrons starting around $1\,\mathrm{GeV}$, that is most noticeable for $z = 2.0 - 5.0$. To calculate the total pair production rate, the emissivity first needs to be integrated over the energy. This is done up to $z = 10.0$ in 0.1 steps and shows a steep increase for up to a redshift of 2.7, after which a slight decrease can be observed again (see Fig. 5.2).

After integrating over the comoving volume, the pair production rate of positrons can be calculated, which shows a quite similar behavior. The total, cumulative, pair production rates up to $z = 5.0$ and $z = 10.0$ are $\dot{n}_{\mathrm{cum}}^{5.0} = 7 \cdot 10^{54}\,\mathrm{s}^{-1}$ and $\dot{n}_{\mathrm{cum}}^{10.0} = 9 \cdot 10^{54}\,\mathrm{s}^{-1}$, respectively. Fig. 5.3 shows that these values are several orders of magnitude larger than the local *pair annihilation rate* in the Milky Way, which is about $5 \cdot 10^{43}\,\mathrm{s}^{-1}$ (Siegert 2023) and the possible contribution of contributing sources.

Given the uncertainties for the BB amplitudes are typically in the range of the uncertainties in the CPB spectrum, it is useful to assume that the uncertainties of these values are dominated by the strongest combinations of BBs (see below). A conservative estimate gives an uncertainty of about one order of magnitude in rates and emissivities.

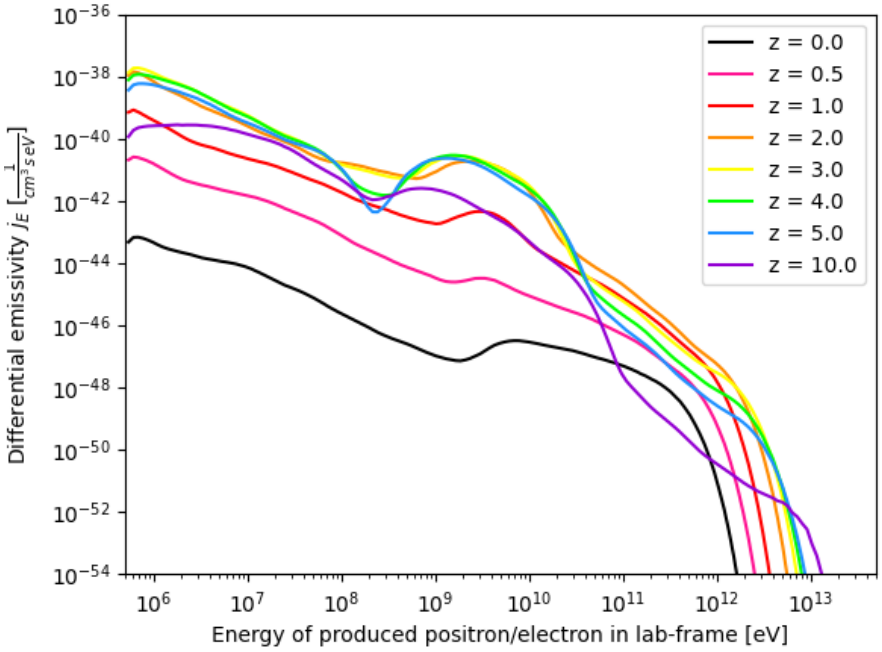

Figure 5.1: Differential positron emissivity for selected redshifts as a function of energy. The spectrum shows a general increase up to $\sim 10^{12}\,\mathrm{eV}$, where it is cut off. However, around $10^9 - 10^{10}\,\mathrm{eV}$ there is a slight excess, which is most pronounced for $z = 2.0 - 5.0$.

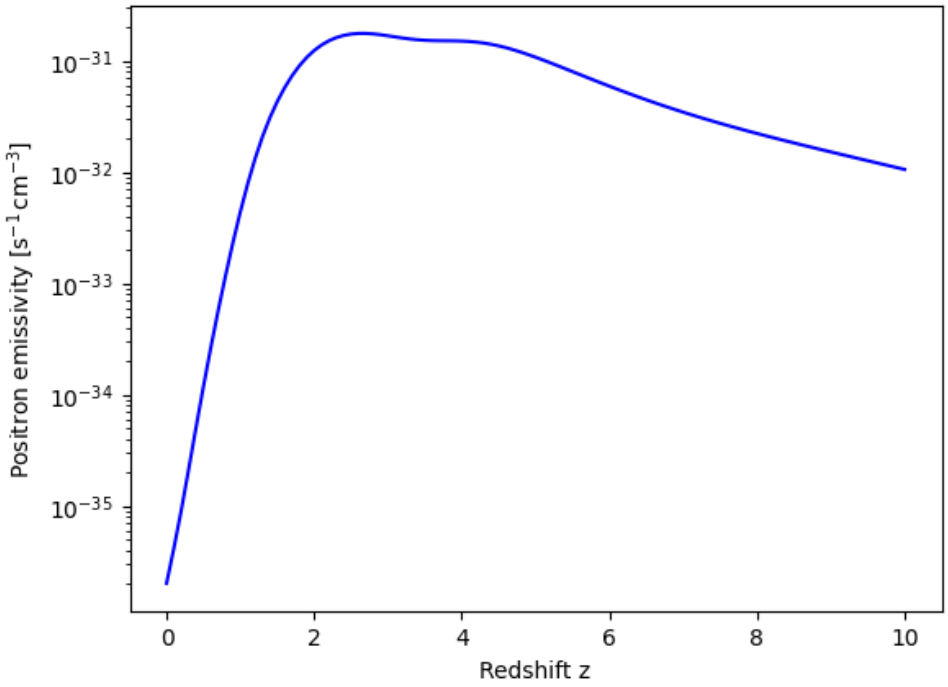

Figure 5.2: Positron emissivity as a function of redshift.

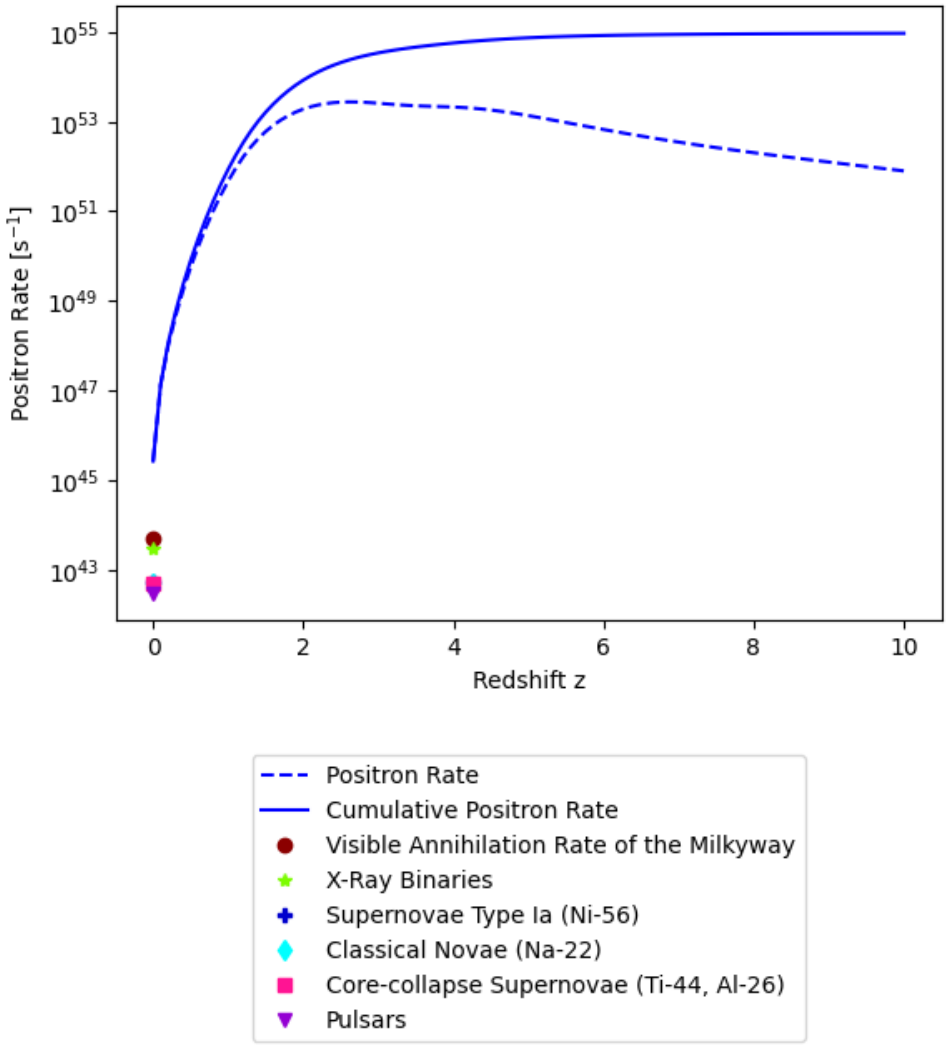

Figure 5.3: Differential and cumulative positron pair production rate of the CPB in redshift bin with a width of 0.1. As comparison, the total annihilation rate of the Milky Way together with possible sources are shown.

5.2 Composition of positron spectrum by Blackbody components

For $z = 0$ (local Universe), pair production from just three BB combinations – namely BB 08 & 28, BB 09 & 27, and BB 10 & 26 – are the most dominant and make up about 43 %; all of these are optical/near-UV ($\sim$ 900 nm, $\sim$ 300 nm, $\sim$ 60 nm) BBs interacting with VHE-BBs ($\sim$ 200 GeV, $\sim$ 70 GeV, $\sim$ 20 GeV). However, their contribution decreases almost immediately with redshift to negligible values as a consequence of the energy-dependent pair production cross section (see Fig. 5.4). Nevertheless, the strongest contribution will always be from optical/UV + VHE γ-rays. But since the BBs shift to higher energies

with redshift, other BBs, that were previously less energetic, will take their places.

Instead, combinations of one specific near-UV BB ($\sim 60\,\mathrm{nm}$) with different MeV/GeV-BBs ($\sim 0.1 - 10\,\mathrm{GeV}$) are the most dominant contributors for virtually all redshifts. Once again, this is driven by the energy-dependent cross section, now in combination with the luminosity functions of the relevant sources – namely quasars and their subtypes. Additionally, the contribution from the near-UV BB becomes significant, as it increases by about an order of magnitude stronger than comparable BBs (see Fig. 4.7). The interaction of BB 10 with BB 24 alone can contribute more than two thirds (68 %) of the total positron production for redshifts around 2.0. In total, those three combinations result into over 75 % of the positron pair production from redshift $2.0 - 6.0$, after which their dominance slowly fades.

5.3 Cosmic-ray positron spectrum and maximum annihilation flux

Integrating the differential positron emissivity over the comoving distance, which corresponds to a line of sight integration, results in the expected differential flux ϕ_E of positrons produced (see Fig. 5.5). An integral over energy would result in the number flux. Through this, a maximum photon flux can be obtained if all positrons were to annihilate locally at their redshift of production. In High energy astrophysics, the differential flux is often scaled by E^3, which is shown in Fig. 5.6.

For the local Universe, the scaled positron flux is monotonously increasing, until it reaches an energy of $10^{12}\,\mathrm{eV}$, where a sharp cut-off can be observed, similar to the cutoff observed for the emissivities. For increasing redshifts, the flux is increasing as well, since the emissivity itself also grows, while the cutoff energy also shifts to higher energies. This presumably lies in the shift of the most energetic BBs into TeV energies, allowing for a more effective production of TeV-positrons.

However, starting around $z \sim 2.0$, the spectra include a bump around $1 - 10\,\mathrm{GeV}$. This peak is still noticeable at $z = 10.0$, where it appears to broaden and reaches energies of close to 100 GeV.

To estimate the flux of the cosmological electron-positron annihilation to the CGB, the contribution by annihilation processes is considered. For simplicity, it is assumed that all positrons annihilate locally at their redshift of origin into two 511 keV-photons. These photons are then observed at the corresponding redshifted energy:

$$E_{\mathrm{obs}} = \frac{511\,\mathrm{keV}}{1+z}. \tag{5.1}$$

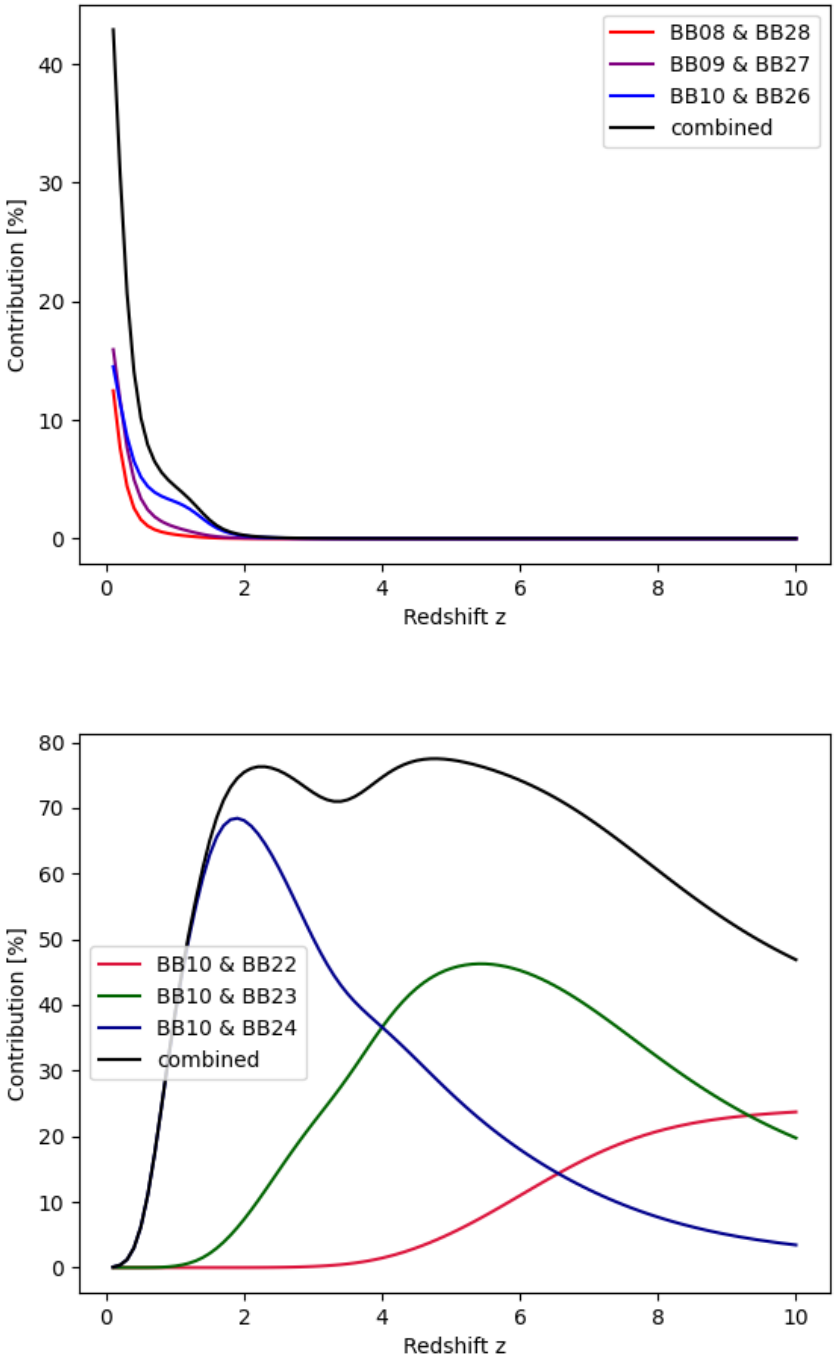

Figure 5.4: The changing contribution of six dominant BB combinations to pair production. Because of the energy-dependent cross section The combinations of BB 08 & 28, BB 09 & 27, and BB 10 & 26 (optical/UV & VHE) almost immediately lose their dominance with redshift (top). Instead, interactions of BB 10 with BB 21, 22, and 23, respectively, become dominate starting around redshift 1.0 and for all redshifts thereafter (bottom).

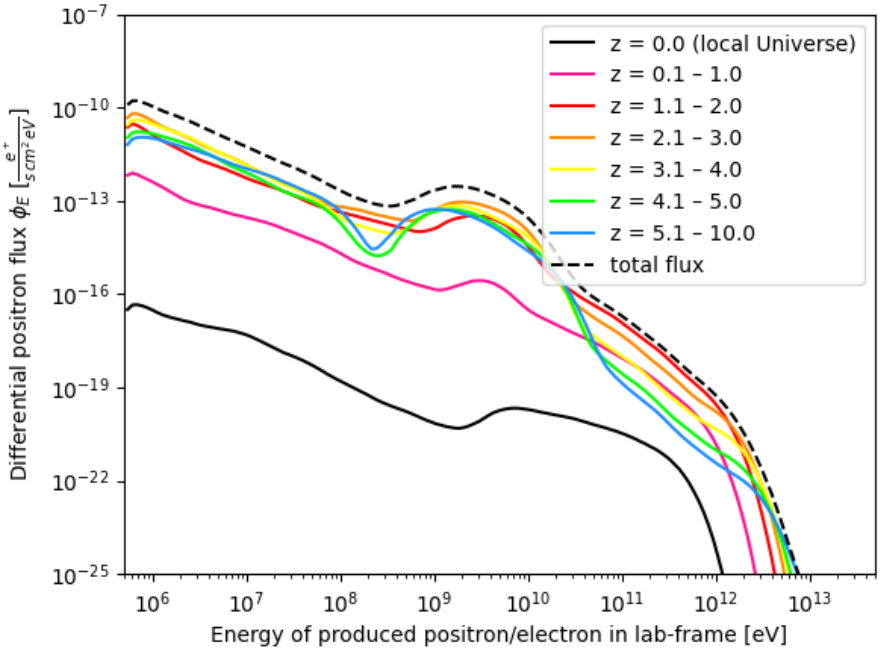

Figure 5.5: Differential positron flux as a function of energy. A slight excess around $1 - 10\,\mathrm{GeV}$ can be observed, which appears to broaden for higher redshifts.

The resulting annihilation lines are best described by a Gaussian function

$$\phi(E) \propto \frac{1}{\sqrt{2\pi}\,\sigma} \exp\left[-\frac{1}{2}\frac{(E - E_{\mathrm{obs}})^2}{\sigma^2}\right], \tag{5.2}$$

where E_{obs} is the center of each observed annihilation line, and σ the standard deviation. It is further assumed that the annihilation lines have a constant full width at half maximum (FWHM) of $1\,\mathrm{keV}$ for galactic conditions. As a broader width of at least $6\,\mathrm{keV}$ can be expected for intergalactic conditions, a line width of $6\,\mathrm{keV}$ and $10\,\mathrm{keV}$ is also modeled (Siegert 2023). For a Gaussian, the FWHM corresponds to:

$$\mathrm{FWHM} = 2\sqrt{2\ln 2}\,\sigma \approx 2.355\,\sigma. \tag{5.3}$$

However, this intrinsic width is also influenced by the redshift effect, which leads to

$$\mathrm{FWHM} = \frac{\Delta E}{1+z}, \tag{5.4}$$

where ΔE is the assumed width of each annihilation line at production.

Including fluxes up to $z = 10.0$ leads to a spectrum spanning between $46\,\mathrm{keV}$ and $511\,\mathrm{keV}$. For $\Delta E = 1\,\mathrm{keV}$, Fig. 5.7 shows sharp peaks around each redshifted annihilation energy, which is a result of the redshift binning in 0.1 steps. Assuming broader widths

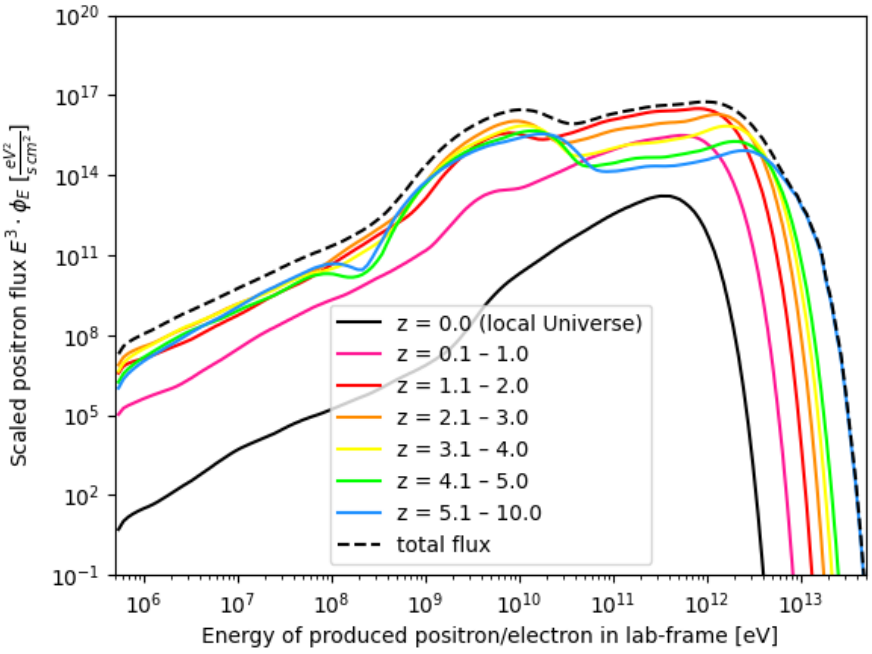

Figure 5.6: Positron flux spectrum produced by pair production from the CPB, scaled by E^3. For small redshifts ($z \lesssim 1.0$), the spectrum shows a steady increase up to a cutoff around 1 TeV. Starting around $z \sim 2.0$, an excess around $1 - 10$ GeV can be observed, that appears to broaden slightly for higher redshifts as well. Beyond 10^{12}eV the flux spectrum drops off, as the emissivity is also cutoff at high energies.

results in a smoother spectrum, albeit each peak is still visible (see bottom plot in Fig. 5.7). More general, the spectrum shows a slight increase from 46 keV up to $\sim$ 100 keV, where it stays constant up to $\sim$ 200 keV, after which it drops off. The cutoff beyond 511 keV and below 46 keV is especially strong, as no photons at these energies can be formed in significant amounts.

Another possible annihilation process can occur via the formation of Positronium (Ps), in which one electron and one positron form a metastable state. Because of the possible spin configurations (parallel or anti-parallel) of each particle, Ps either occurs as para-Positronium (p-Ps) with a total spin of 0 (singlet), or as ortho-Positronium (o-Ps) with a total spin of 1 (triplet). This results into two different decay modes: p-Ps will decay into two photons forming distinct 511 keV-lines, whereas o-Ps will decay into three photons leading to a continuum. Putting this together, results in a 1:4.5-ratio of photons produced by p-Ps and o-Ps.

Assuming a spectrum completely originating from Ps-decay shows a less chaotic behavior as the sharp peaks are complemented by the continuum of o-Ps photons (see Fig. 5.8). The big difference to the spectrum resulting from direct annihilation is the production of

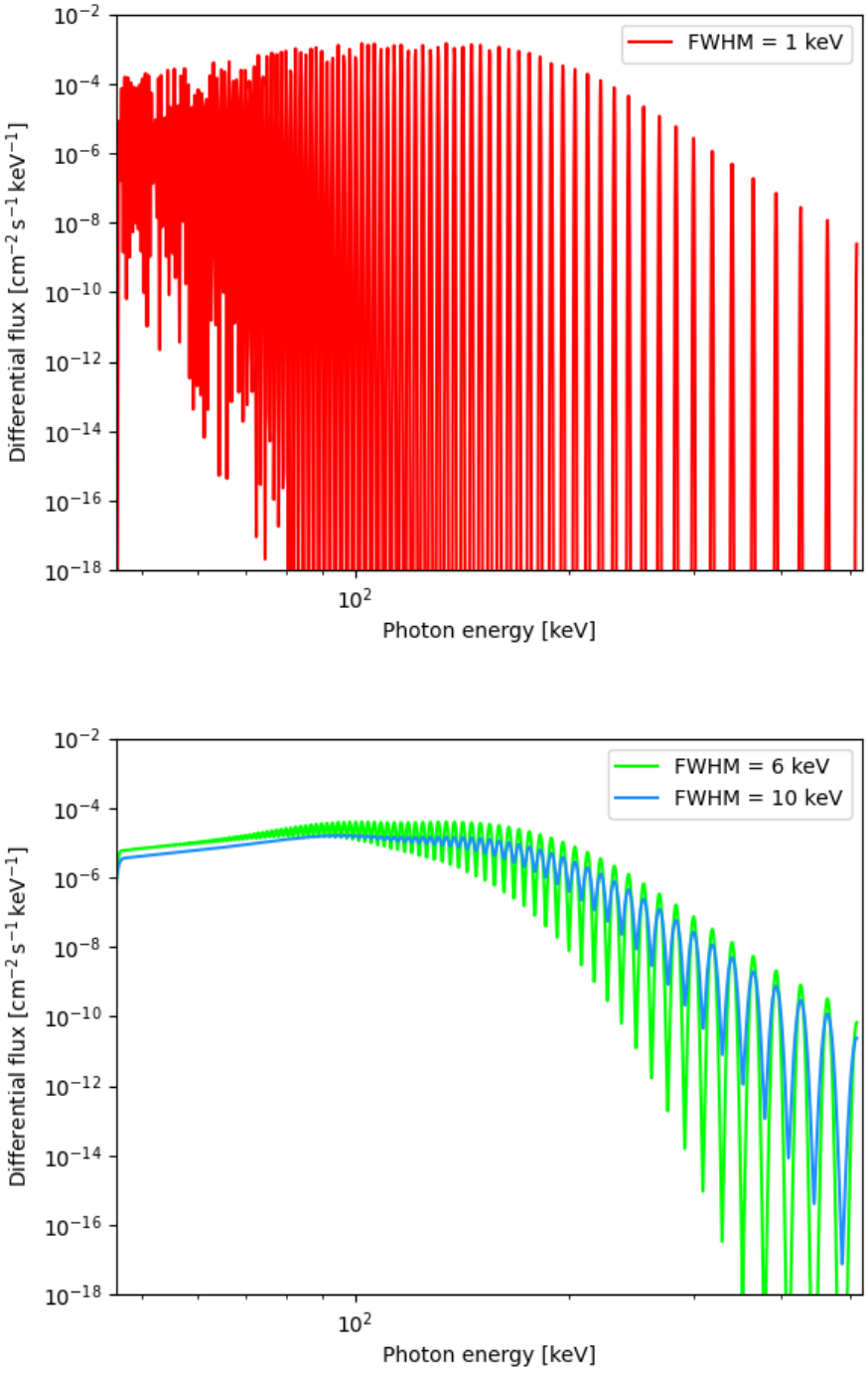

Figure 5.7: Annihilation spectrum of positrons assuming all positrons annihilate at their redshift of production into a 511 keV-line, resulting in distinct peaks at the redshifted annihilation energies. *Top*: For a FWHM of 1 keV, the spectrum shows a rather chaotic behavior as the distance between each peak is greater than the width of each annihilation line, leading to no overlap. *Bottom*: For a FWHM of 6 keV and 10 keV, the spectrum is oscillating much less, as the broader annihilation lines overlap to, at least, some degree.

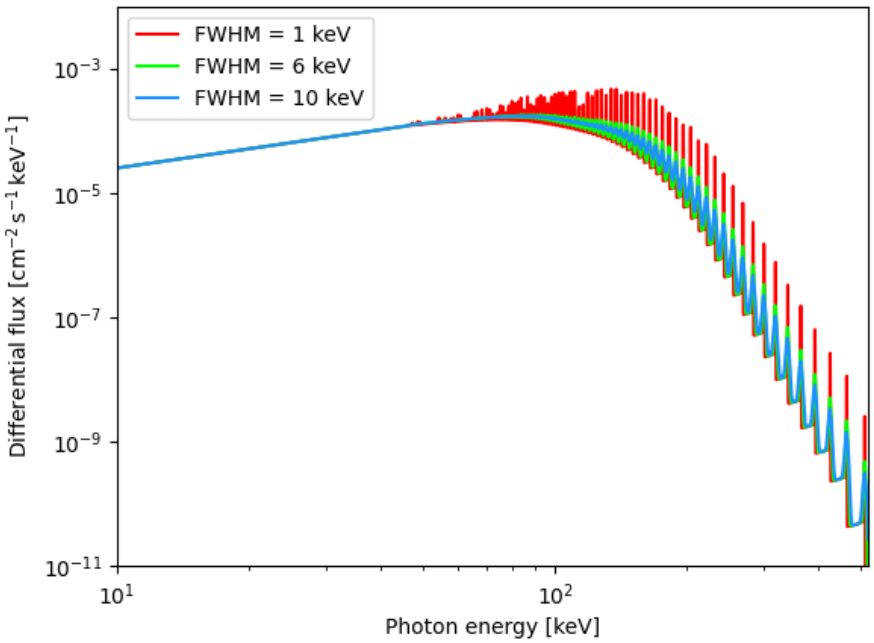

Figure 5.8: The spectrum of decay via Ps shows a much less chaotic behavior even for a FWHM of 1 keV. Reason for that is the continuum spectrum of o-Ps, resulting in a broad peak around 100 keV.

low-energetic photons below 46 keV, made possible by the production of o-Ps photons as well. This leads to a broad, but more pronounced peak around 100 keV.

Chapter 6

Conclusion and Outlook

The local pair production rate (up to $\sim 200\,\mathrm{Mpc}$) from CPB self-interactions is about $3 \times 10^{45}\,\mathrm{s}^{-1}$, that is, about 100 times stronger than the Milky Way itself (Siegert 2023). However, this volume contains around 10^5 Milky-Way-like galaxies. Hence, the CPB-contribution becomes insignificant relative to the number of galaxies and thus its contribution is potentially small. On large scales, this "cosmic pair production rate" comes from the billions of galaxies filling space. Unlike the highly anisotropic distribution of galaxies in the Local Volume, which would produce directional "hotspots" in pair production, the cosmic pair production (and putative annihilation) rate would be rather isotropic.

Despite this, beyond $z = 2$, contributions by galaxies become comparable to – or even smaller than – those from the CPB, as other sources begin to dominate at high redshifts, such as AGNs including quasars and blazars.

Assuming all positrons will decay via the formation of Ps, one can compare the resulting spectrum to the CGB-spectrum. In Kinzer et al. (1997), the CGB between $\sim 80 - 400\,\mathrm{keV}$ is modeled by the power law

$$\frac{\mathrm{d}N}{\mathrm{d}E} = (2.62 \pm 0.05) \cdot 10^{-3} \left(\frac{E}{100\,\mathrm{keV}}\right)^{-2.75\pm0.08} \mathrm{cm}^{-2}\,\mathrm{s}^{-1}\,\mathrm{keV}^{-1}\,\mathrm{sr}^{-1}. \tag{6.1}$$

Fig. 6.1 shows possible Ps spectra and the CGB-model. For energies below 100 keV, the spectrum of the emission from Ps shows almost no increase. However, the CGB-flux decreases by about three to four orders of magnitude on the same interval. Around the peak of 100 keV, the Ps-annihilation spectrum ($\sim 10^{-4}\,\mathrm{cm}^{-2}\,\mathrm{s}^{-1}\,\mathrm{keV}^{-1}$) reaches its maximum. There, the flux is only two orders of magnitude smaller than that of the CGB ($\sim 10^{-1} - 10^{-2}\,\mathrm{cm}^{-2}\,\mathrm{s}^{-1}\,\mathrm{keV}^{-1}$), opening a possible window for the observation of the pair annihilation of positrons. After this peak, however, the spectrum via Ps-decay decreases faster than the CGB-spectrum, meaning the relative contribution decreases as well, leaving only a small flux around 511 keV.

Of further interest is the cosmic-ray positron spectrum, which, for most redshifts, shows an excess for energies between $1 - 10\,\mathrm{GeV}$. The Alpha Magnetic Spectrometer (AMS) on

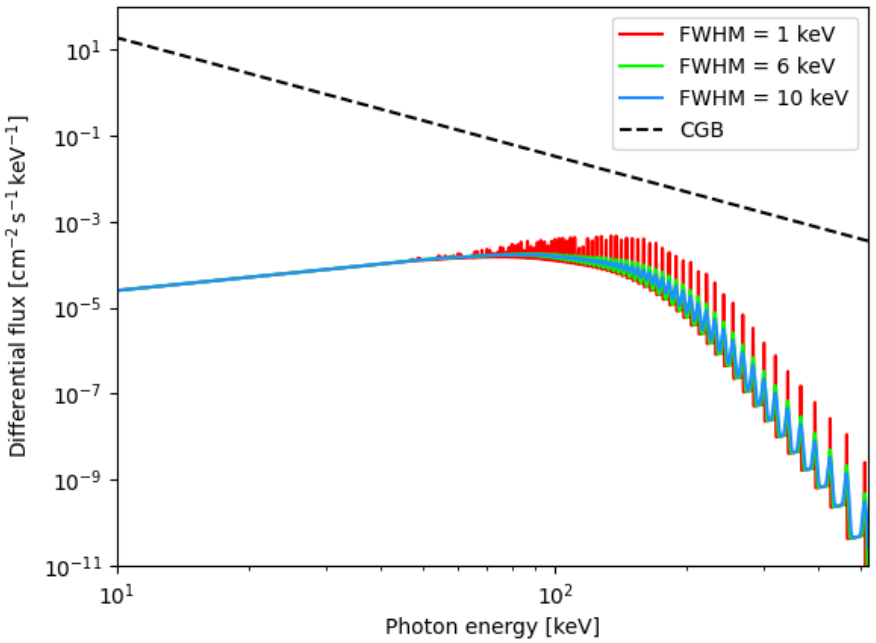

Figure 6.1: Annihilation via the formation of Ps and the CGB. Around 100 keV the annihilation spectrum has the biggest relative contribution to the CGB, possibly making up around 1 % of the flux.

the International Space Station has been measuring the positron flux since 2011. Based on 1.9 million positrons collected from 2011 to 2017, the positron spectrum appears to encompass two different components: A "diffuse term" peaking around 5 GeV and another "source term" peaking around few 100 GeV with a sharp cutoff in the TeV-energies (see Fig. 6.2).

Comparing the AMS-spectrum to the scaled positron flux spectrum derived from CPB-interactions (see Fig. 6.3), shows striking similarities. First, there are two visible peaks, the first one being around 10 GeV, the second one around 1 TeV, which are at about the same energies as the peaks of the AMS-spectrum – albeit the peaks of the theoretical positron spectrum are at slightly higher energies. This suggests that these two peaks correspond to the "diffuse term" and "source term". This can be motivated by the relative size of both peaks, which is about 2, meaning the second peak corresponds to a flux double the size of the first peak – just about the same ratio of the peaks in the AMS-spectrum. Additionally, the model in Aguilar et al. (2019) includes an exponential drop-off for the higher energetic source term that starts to take effect on the order of 1 TeV, comparable to the positron spectrum (Fig. 5.6).

Therefore, even though the pair production positron production by the CPB can not explain the plateau of the measured positron spectrum starting around 10 GeV, the dif-

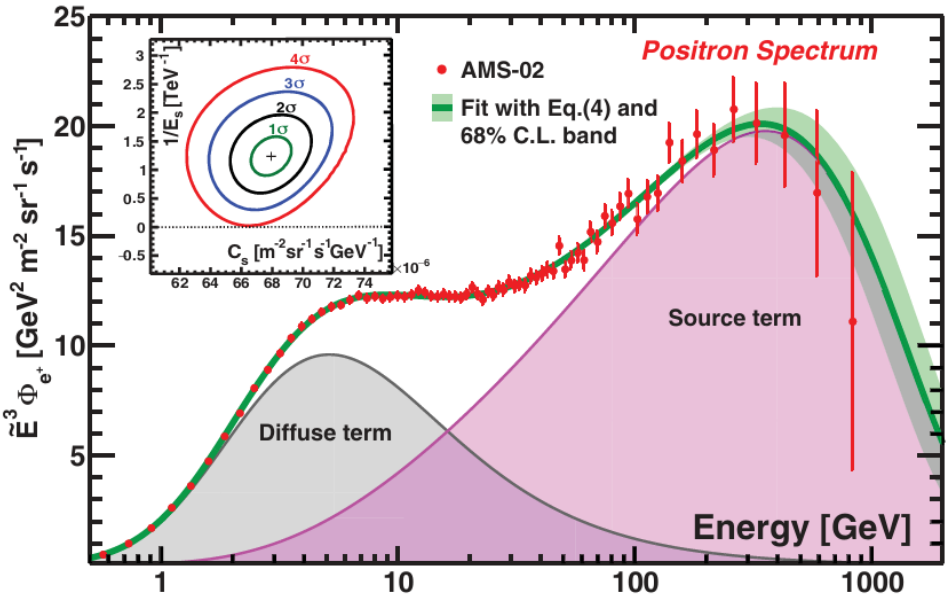

Figure 6.2: The positron flux measured by the Alpha Magnetic Spectrometer (AMS) on the International Space Station shown as a function of energy, scaled by E^3. It appears to consists out of two underlying spectra: A lower energetic "diffuse term" and a higher energetic "source term" that is eventually cut off beyond TeV-energies (from Aguilar et al. 2019).

ferentiation between the diffuse and source term may not be that clearly cut. Further, the positrons measured by AMS are coming from all directions, meaning there can not be a specific source that is producing positrons. Combining that with the isotropic nature of the CPB, makes either the CPB itself or a very local source a plausible candidate explaining, at least, a part of the positron flux possibly even for higher energies.

Finally, the question that naturally arises concerns the fate of the positrons: What happens to them? The big number of produced positrons can not remain unnoticed.

Since the ISM is filled with electrons, it is possible that positrons interact with those electrons, leading to annihilation – the opposite process of pair production, where two photons emerge. These interactions could make a measurable signal in the CGB if positrons spend enough time in the ISM to annihilate. This could occur through direct in-flight annihilation, producing a spectrum of photon energies up to the GeV range, or – after undergoing cooling processes such as Compton scattering or synchrotron radiation – through the formation of Ps, which ultimately annihilates into two or more photons. This would lead to a distinct 511 keV-line and an excess signal, which, on the one hand, consists of many reshifted 511 keV-lines and the spectrum arising from the decay of Ps that peaks around 100 keV. The flux around 100 keV may be strong enough that it can be measured as a component of the CGB.

Alternatively, without catastrophic losses, such as bremsstrahlung (Krumholz et al.

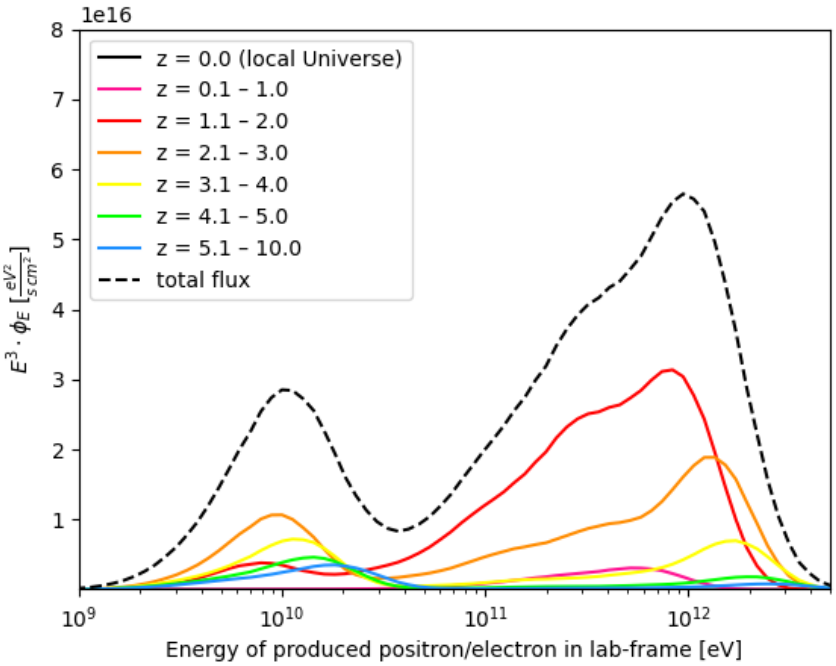

Figure 6.3: Positron flux resulting from pair production by CPB-photons, scaled by E^3. The spectrum consists of two peaks, the first one having its maximum at $\sim 10\,\mathrm{GeV}$ and the second one at $\sim 1\,\mathrm{TeV}$, after which a clear cutoff occurs. The spectrum exhibits striking similarities to the positron spectrum measured by AMS.

2022), positrons may not thermalize but instead propagate for a long time and thus enrich the intergalactic medium (IGM) with antimatter. This would in turn lead to the question of what the consequences of such an abundance of positrons in the IGM might be.

The Compton Spectrometer and Imager (COSI), a γ-ray telescope to be launched in 2027, will perform full-sky surveys between $0.2 - 5\,\mathrm{MeV}$. It will be crucial for further understanding of the CPB in that energy regime and may find some answers to the questions posted above.

Until then, the fate of the positrons seems to remain a bit of a mystery – it will, at least for the next few years, still remain *The Positron Puzzle*.

Chapter 7

Summary

7.1 English Summary

In this Bachelorthesis, the electron positron pair production from the Cosmic Photon Background (CPB), which is an isotropic radiation ranging across the entire electromagnetic spectrum, as a function of redshift was calculated. Decomposing the CPB into 28 Blackbodies (BBs) led to a reasonable description of the CPB without large residuals, where each BB corresponded to a specific energy. After identifying each BB with a specific composition of astrophysical sources such as the Cosmic Microwave Background (CMB), Active Galactic Nuclei (AGNs), star-forming galaxies, quasars, and blazars, the luminosity evolution of each BB could be determined. A helpful tool was the luminosity function, which describes the number density of sources as a function of luminosity. Incorporating the redshift evolution of the luminosity function of each BB together with the shift to higher energies resulting from the expansion of the Universe, led to a model of the CPB up to redshift 10.0.

From this, the positron emissivity, which is the positron production per volume, was calculated. Integrating the emissivity over the comoving volume resulted in the positron rate, which increases from its local value of $\sim 3 \cdot 10^{45}\,\mathrm{s}^{-1}$ up to $z \approx 2.7$, where it reaches its maximum rate on the order of $10^{53}\,\mathrm{s}^{-1}$. This exceeds the pair annihilation rate observed in the Milky Way by far. The most significant contributions arise from the interaction of UV and γ-Ray BBs, primarily powered by quasars and blazars. The spectrum of produced positrons appears to have a flux excess around $1 - 10\,\mathrm{GeV}$ and also close to $1\,\mathrm{TeV}$, which was also observed by Alpha Magnetic Spectrometer (AMS) on the International Space Station, meaning the pair production by CPB-photons is a promising explanation for the observed positron excess.

7.2 Deutsche Zusammenfassung

In dieser Bachelorarbeit wurde die Elektron-Positron Erzeugungsrate aus dem Kosmischen Photonenhintergrund (*engl.* Cosmic Photon Background, CPB) in Abhängigkeit zur Rotverschiebung berechnet. Der CPB ist eine isotrope Strahlung, die sich über das komplette elektromagnetische Spektrum erstreckt. Durch eine Überlagerung von 28 Schwarzkörper-Strahlern (*engl.* Blackbody, BB) konnte der CPB sinnvoll ohne große Abweichungen beschrieben werden, wobei jeder BB einem bestimmten Energiebereich entsprach. Nachdem jeder BB mit einer spezifischen Zusammensetzungen verschiedener astrophysikalischer Quellen, wie dem Kosmischen Mikrowellenhintergrund, Aktiven Galaxienkernen, sternbildender Galaxien oder Quasaren und Blazaren, identifiziert wurde, wurde die Helligkeitsentwicklung eines jeden BB bestimmt. Ein hilfreiches Mittel dafür war die Helligekitsfunktion, welche die Anzahlsdichte der Quellen in Abhängigkeit der Helligkeit beschreibt. Unter Berücksichtigung der Helligkeitsentwicklung eines jeden BB zusammen mit der Verschiebung zu höheren Energien, welche aus der Ausdehnung des Universums resultiert, konnte ein Modell des CPB bis hin zu einer Rotverschiebung von 10.0 erstellt werden.

Davon ausgehend, wurde die Positronenemissivität berechnet, welche die Positronen-Paarbildung pro Raumvolumen ist. Integriert man diese über das mitbewegte Volumen, erhält man die Positronen Paarerzeugungsrate, welche von ihrem lokalen Wert von $\sim 3 \cdot 10^{45}\,\mathrm{s}^{-1}$ bis etwa $z \approx 2.7$ ansteigt, wo sie ihren maximalen Wert in der Größenordnung von $10^{53}\,\mathrm{s}^{-1}$ liegt. Dies übersteigt die Annihilierungsrate der Milchstraße bei weitem. Die stärksten Beiträge stammen dabei aus der Interaktion von UV- und γ-Schwarzkörperstrahlern, wobei letztere primär von Quasaren und Blazaren angetrieben werden. Das Spektrum der erzeugten Positronen scheint einen Überschuss im Fluss bei etwa $1-10\,\mathrm{GeV}$ sowie bei etwa $1\,\mathrm{TeV}$ zu besitzen, welcher auch vom Alpha Magnetic Spectrometer (AMS) auf der Internationalen Raumstation beobachtet wurde. Dies bedeutet, dass die Paarerzeugung von Positronen aus Photonen des CPB eine vielversprechende Erklärung für diesen Positronenüberschuss sein könnte.

Bibliography

Aguilar, M., Ali Cavasonza, L., Ambrosi, G., et al. 2019, Phys. Rev. Lett., 122, 041102.

Aird, J., Coil, A. L., Georgakakis, A., et al. 2015, Monthly Notices of the Royal Astronomical Society, 451, 1892.

Ajello, M., Costamante, L., Sambruna, R. M., et al. 2009, The Astrophysical Journal, 699, 603.

Ajello, M., Gasparrini, D., Sánchez-Conde, M., et al. 2015, The Astrophysical Journal Letters, 800, L27.

Ajello, M., Greiner, J., Sato, G., et al. 2008, The Astrophysical Journal, 689, 666.

Ajello, M., Mauro, M. D., Paliya, V. S., & Garrappa, S. 2020, The Astrophysical Journal, 894, 88.

Ajello, M., Romani, R. W., Gasparrini, D., et al. 2014, The Astrophysical Journal, 780, 73.

Ajello, M., Shaw, M. S., Romani, R. W., et al. 2012, The Astrophysical Journal, 751, 108.

Anderson, C. D. 1933, Physical Review, 43, 491.

Aversa, R., Lapi, A., Zotti, G. d., Shankar, F., & Danese, L. 2015, The Astrophysical Journal, 810, 74.

Blackett, P. M. S. & Occhialini, G. P. S. 1933, Nature, 131, 1011.

Boettcher, M. & Schlickeiser, R. 1997, The Pair Production Spectrum from Photon-Photon Annihilation.

Chen, J. & Totani, T. 2025, Monthly Notices of the Royal Astronomical Society, 540, 3221.

Diehl, R., Siegert, T., Hillebrandt, W., et al. 2014, Science, 345, 1162.

Dirac, P. A. M. & Fowler, R. H. 1928, Proceedings of the Royal Society of London. Series A, Containing Papers of a Mathematical and Physical Character, 117, 610.

Dirac, P. A. M. & Fowler, R. H. 1930, Proceedings of the Royal Society of London. Series A, Containing Papers of a Mathematical and Physical Character, 126, 360.

Fixsen, D. J. 2009, The Astrophysical Journal, 707, 916.

Fukazawa, Y., Matake, H., Kayanoki, T., Inoue, Y., & Finke, J. 2022, The Astrophysical Journal, 931, 138.

Greiner, W. & Reinhardt, J. 2008, Quantum electrodynamics (Springer Science & Business Media).

Gruppioni, C., Pozzi, F., Rodighiero, G., et al. 2013, Monthly Notices of the Royal Astronomical Society, 432, 23.

Hallwachs, W. 1888, Annalen der Physik, 269, 301.

Helgason, K., Ricotti, M., & Kashlinsky, A. 2012, The Astrophysical Journal, 752, 113.

Hill, R., Masui, K. W., & Scott, D. 2018, Applied Spectroscopy, 72, 663.

Hogg, D. W. 2000, Distance measures in cosmology.

Inoue, Y. 2014, Cosmic Gamma-ray Background Radiation.

Jauch, J. M. & Rohrlich, F. 1976, The Theory of Photons and Electrons: the relativistic quantum field theory of charged particles with spin one-half, 2nd edn. (Berlin: Springer).

Khaire, V. & Srianand, R. 2019, Monthly Notices of the Royal Astronomical Society, 484, 4174.

Kinzer, R. L., Jung, G. V., Gruber, D. E., et al. 1997, The Astrophysical Journal, 475, 361.

Krumholz, M. R., Crocker, R. M., & Sampson, M. L. 2022, Monthly Notices of the Royal Astronomical Society, 517, 1355.

Lagache, G., Puget, J.-L., & Dole, H. 2005, Annual Review of Astronomy and Astrophysics, 43, 727.

Lahav, O. & Liddle, A. R. 2024, The Cosmological Parameters.

Leone, M. & Robotti, N. 2010, European Journal of Physics, 31, 975.

Longair, M. S. 2011, High energy astrophysics (Cambridge university press).

Madau, P. & Dickinson, M. 2014, Annual Review of Astronomy and Astrophysics, 52, 415.

Madejski, G. G. & Sikora, M. 2016, Annual Review of Astronomy and Astrophysics, 54, 725.

Mancuso, C., Lapi, A., Cai, Z.-Y., et al. 2015, The Astrophysical Journal, 810, 72.

Marcotulli, L., Ajello, M., Urry, C. M., et al. 2022, The Astrophysical Journal, 940, 77.

McLeod, D. J., McLure, R. J., Dunlop, J. S., et al. 2021, Monthly Notices of the Royal Astronomical Society, 503, 4413.

Michelson, A. A. & Morley, E. W. 1887, American journal of science, 3, 333.

Mohr, P., Newell, D., Taylor, B., & Tiesinga, E. 2024, CODATA Recommended Values of the Fundamental Physical Constants: 2022.

Palicio, P. A., Matteucci, F., Della Valle, M., & Spitoni, E. 2024, AA, 689, A203.

Penny, S. 2025, Bachelor's thesis, Julius-Maximilians Universität Würzburg.

Planck Collaboration, Aghanim, N., Akrami, Y., et al. 2020a, AA, 641, A6.

Planck Collaboration, Akrami, Y., Ashdown, M., et al. 2020b, AA, 641, A4.

Rayleigh, L. 1900, The London, Edinburgh, and Dublin Philosophical Magazine and Journal of Science, 49, 539.

Ruiz-Lapuente, P., The, L.-S., Hartmann, D. H., et al. 2016, The Astrophysical Journal, 820, 142.

Schechter, P. 1976, Astrophysical Journal, 203, 297.

Shen, X., Hopkins, P. F., Faucher-Giguère, C.-A., et al. 2020, Monthly Notices of the Royal Astronomical Society, 495, 3252.

Siegert, T. 2023, Astrophysics and Space Science, 368, 27.

Sikora, M., Begelman, M. C., & Rees, M. J. 1994, Astrophysical Journal, 421, 153.

Tompkins, S. A., Driver, S. P., Robotham, A. S. G., et al. 2023, Monthly Notices of the Royal Astronomical Society, 521, 332.

Yuan, Z., Wang, J., Zhou, M., Qin, L., & Mao, J. 2017, The Astrophysical Journal, 846, 78.

Appendix

Parameters of luminosity functions

$\log(\phi_0)$	$\log(L_*)$	β	γ	z_c	p_1	p_2	k_1	k_2
$-4.84^{+0.10}_{-0.15}$	$24.66^{+0.19}_{-0.14}$	$0.44^{+0.02}_{-0.02}$	$0.31^{+0.02}_{-0.02}$	$0.82^{+0.10}_{-0.10}$	$0.28^{+0.30}_{-0.28}$	$-5.67^{+0.34}_{-0.38}$	$4.85^{+0.14}_{-0.14}$	$4.64^{+1.46}_{-1.20}$

Table 1: Parameters of the Radio luminosity function of AGNs as well as the evolution parameters (see Eq. 4.16 – 4.20) (Yuan et al. 2017).

wavelength [nm]	filter	M_0^*	q	ϕ_o^*	p	α_0	r
4500	M	-21.84	0.3	3.29	0.8	-1.00	0.035
910	z	-22.86	0.4	2.05	0.4	-1.00	0.060
360	U	-20.20	1.0	5.46	0.5	-1.00	0.076

Table 2: Parameters of the Optical luminosity function (Schechter function) and its evolution parameters (see Eq. 4.23 – 4.27) (Helgason et al. 2012).

range	m_1	m_2	k_1	k_2
soft X-ray $(0.5 - 2.0\,\mathrm{keV}$	5.712	17.67	-0.026	0.278
hard X-ray $(2.0 - 10.0\,\mathrm{keV})$	4.073	12.60	-0.026	0.278

Table 3: Parameters of the bolometric corrections for the quasar luminosity function for X-ray energies (see Eq. 4.32) (Shen et al. 2020).

a_0	a_1	b_0	b_1	b_2
$0.3653^{+0.0115}_{-0.0114}$	$-0.6006^{+0.0422}_{-0.0417}$	$2.4709^{+0.0163}_{-0.0169}$	$-0.9963^{+0.0167}_{-0.0161}$	$1.0716^{+0.0180}_{-0.0181}$

c_0	c_1	c_2	d_0	d_1
$12.9656^{+0.0092}_{-0.0089}$	$-0.5758^{+0.0020}_{-0.0019}$	$0.4698^{+0.0025}_{-0.0026}$	$-3.6276^{+0.0209}_{-0.0203}$	$-0.3444^{+0.0063}_{-0.0061}$

Table 4: Evolution parameters for the bolometric luminosity function of quasars (see Eq. 4.33 – 4.37) (Shen et al. 2020).

$\log A$	α	$\log L_0$	β	z_c
-3.59 ± 0.08	0.81 ± 0.03	41.12 ± 0.07	2.66 ± 0.24	0.82 ± 0.10

Table 5: (Evolution) parameters of the X-Ray luminosity function of galaxies (see Eq. 4.38 – 4.39) (Aird et al. 2015).

A	L_*	γ_1	γ_2	k	ξ
1.13 ± 0.12	$(1.01 \pm 0.66) \cdot 10^{44}$	-1.00 ± 2.07	1.67 ± 0.17	3.23 ± 0.57	-1.62 ± 0.47

Table 6: Parameters for the luminosity function and evolution function of FSRQs below 200 keV (see Eq. 4.40 – 4.42) (Marcotulli et al. 2022).

A	γ_1	γ_2	L_*	k	γ
$(0.175 \pm 0.034) \cdot 10^7$	-50.0	2.49 ± 0.37	2.42 ± 0.19	3.67 ± 0.48	-0.30 ± 0.08

Table 7: Parameters for the luminosity function and evolution function for FSRQs beyond 200 keV (see Eq. 4.40, 4.41, and 4.43) (Ajello et al. 2009).

A	γ_1	L_*	γ_2
$3.39^{+7.44}_{-2.13} \cdot 10^{-9}$	$0.27^{+0.26}_{-0.46}$	$0.28^{+0.43}_{-0.21}$	$1.86^{+0.86}_{-0.48}$

z_c*	p_1^*	τ	p_2	α	μ^*	β
$1.34^{+0.22}_{-0.27}$	$2.24^{+1.25}_{-1.07}$	$4.92^{+1.45}_{-2.12}$	$-7.37^{+2.95}_{-5.43}$	$4.53^{+4.98}_{-6.52} \cdot 10^{-2}$	$2.10^{+0.03}_{-0.03}$	$6.46^{+2.34}_{-2.07} \cdot 10^{-2}$

Table 8: Parameters of the luminosity function of BL Lacs (top) and evolution parameters (bottom) (see Eq. 4.46 – 4.49) (Ajello et al. 2014).

Decomposition into Blackbodies

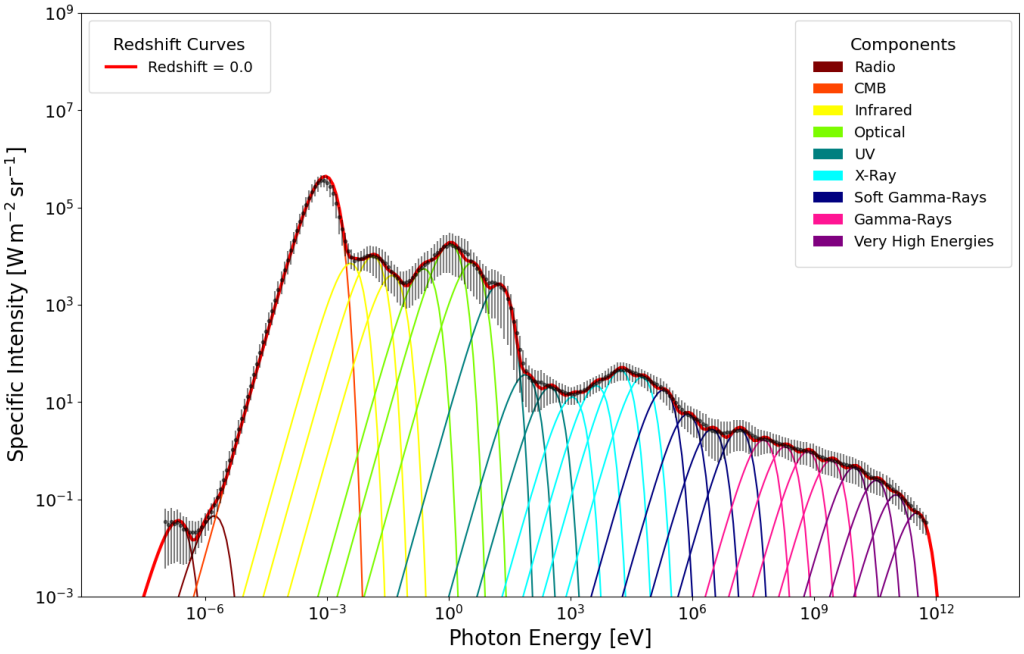

Figure 1: Blackbody decomposition of the CPB for Redshift 0. Data points taken from Hill et al. (2018)

Redshift evolution of the CPB

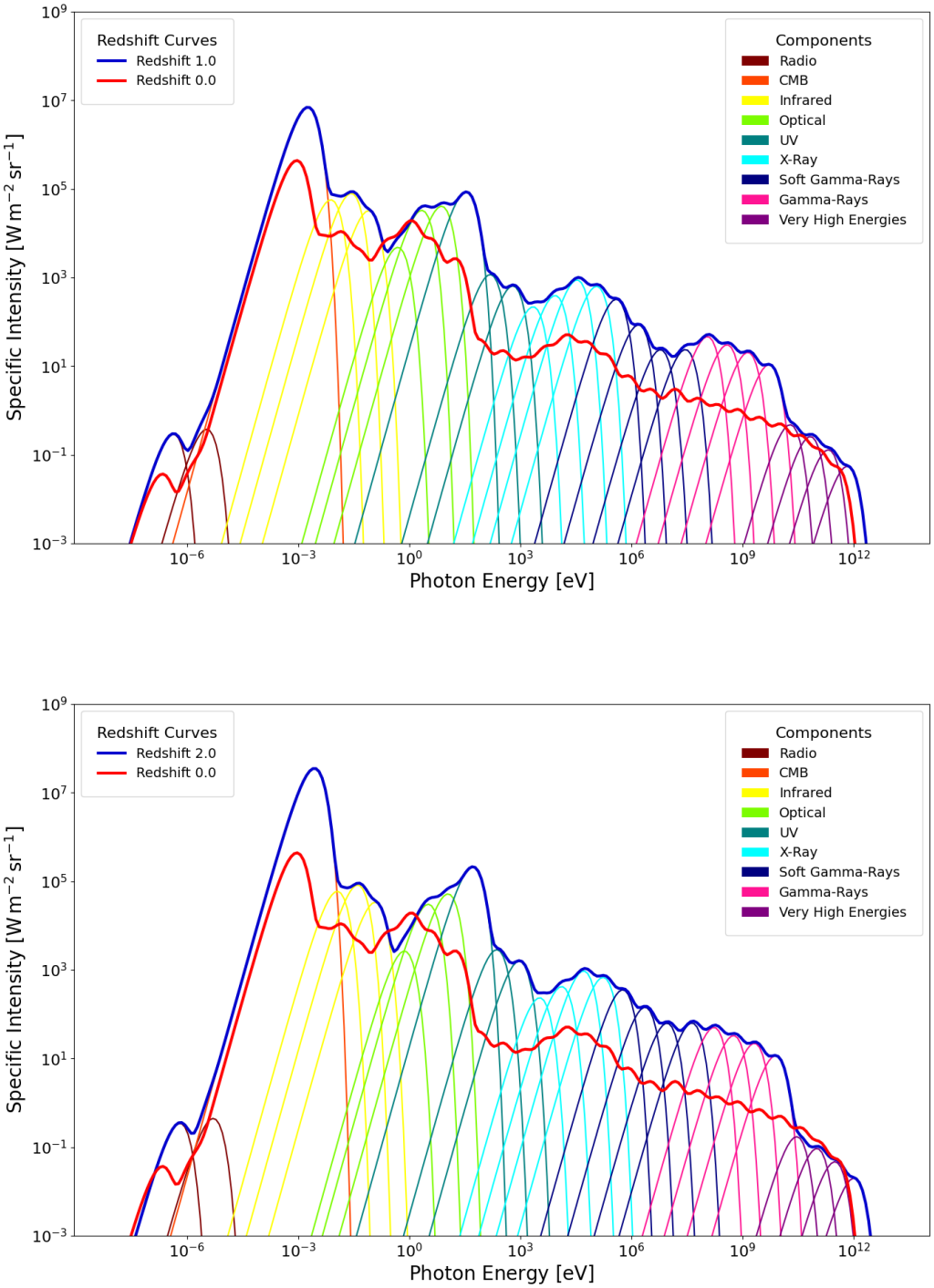

Figure 2: Blackbody evolution of the CPB for Redshift 1.0 (top), and 2.0 (bottom).

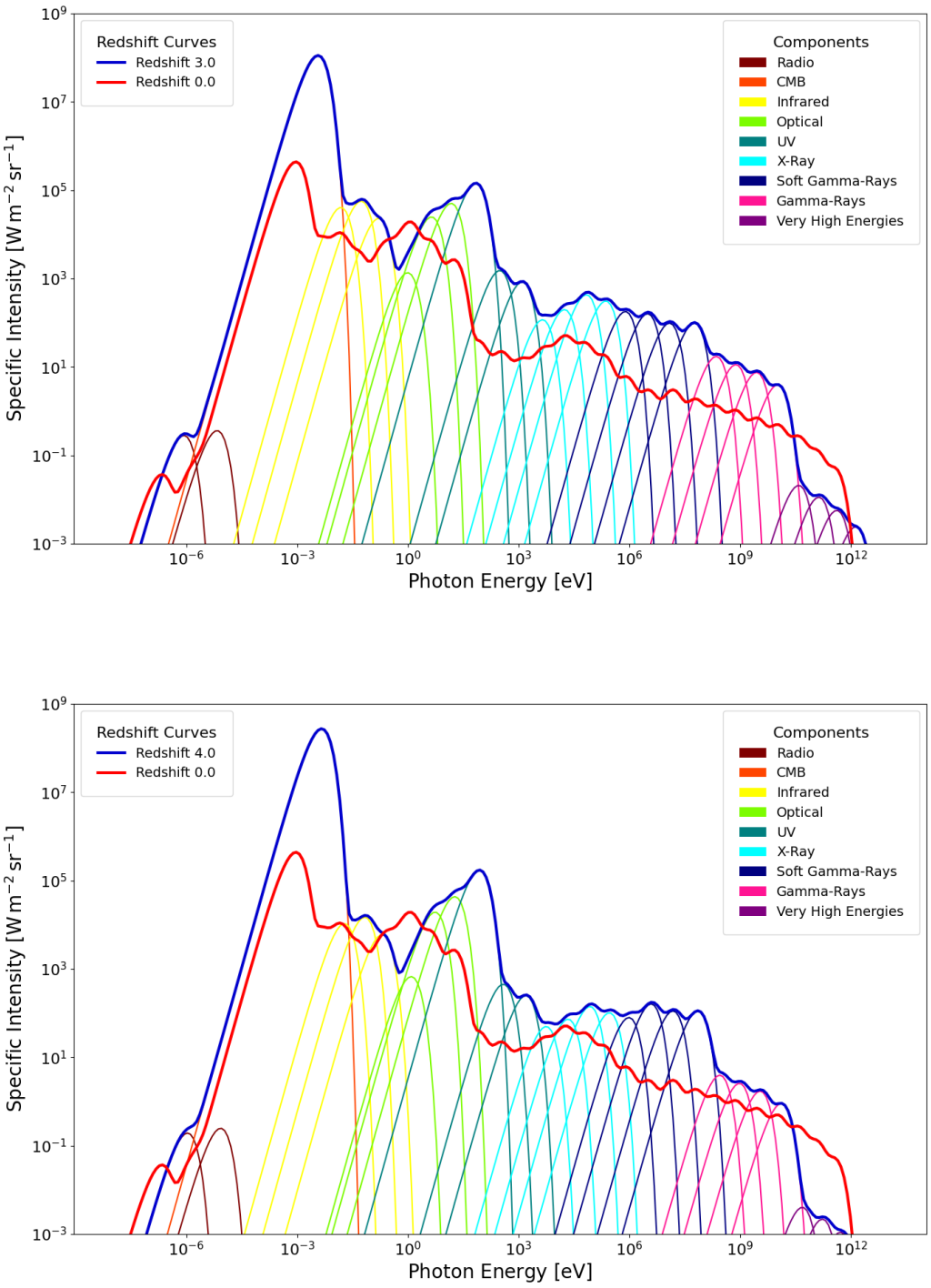

Figure 3: Blackbody evolution of the CPB for Redshift 3.0 (top), and 4.0 (bottom).

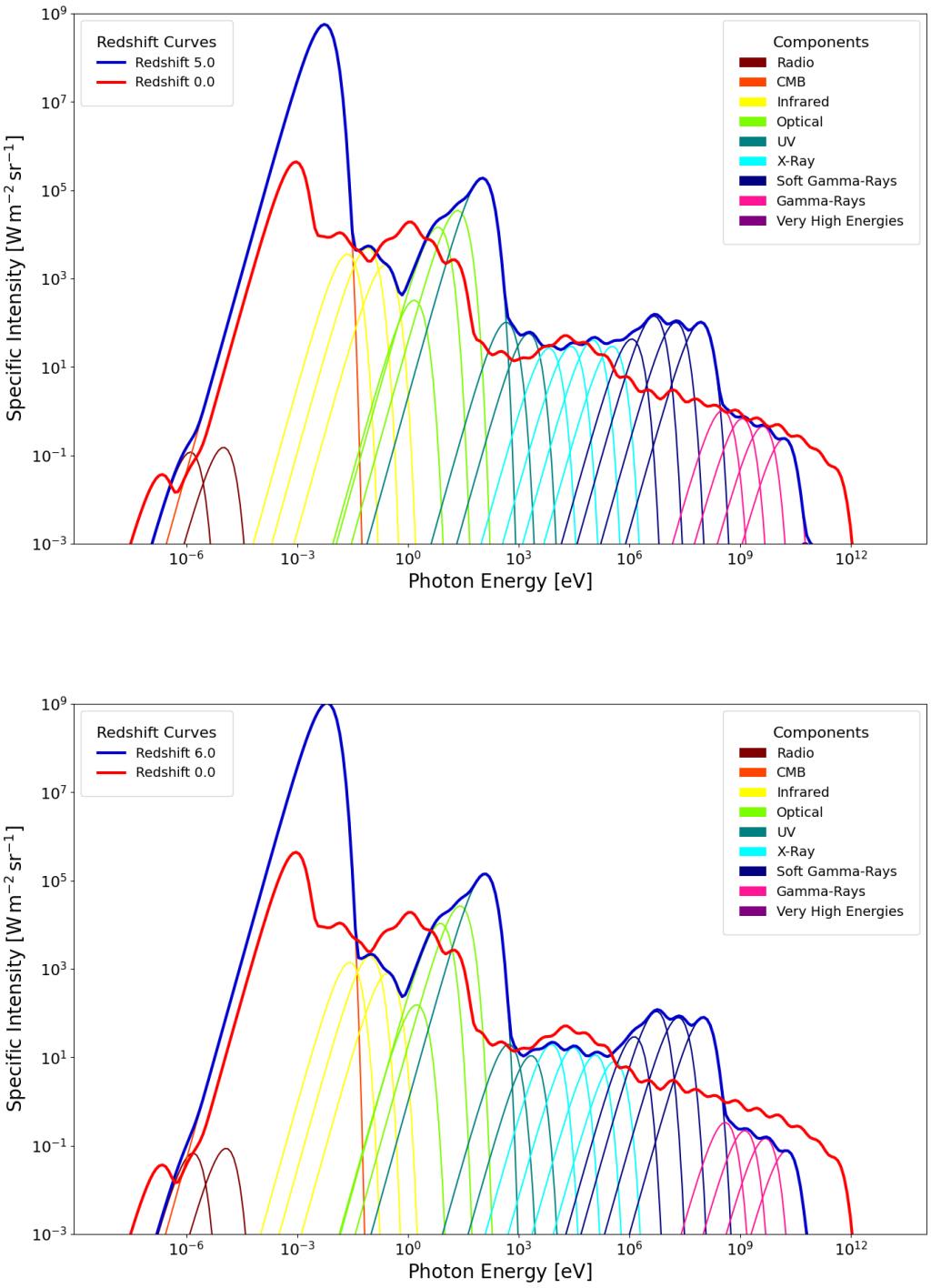

Figure 4: Blackbody evolution of the CPB for Redshift 5.0 (top), and 6.0 (bottom).

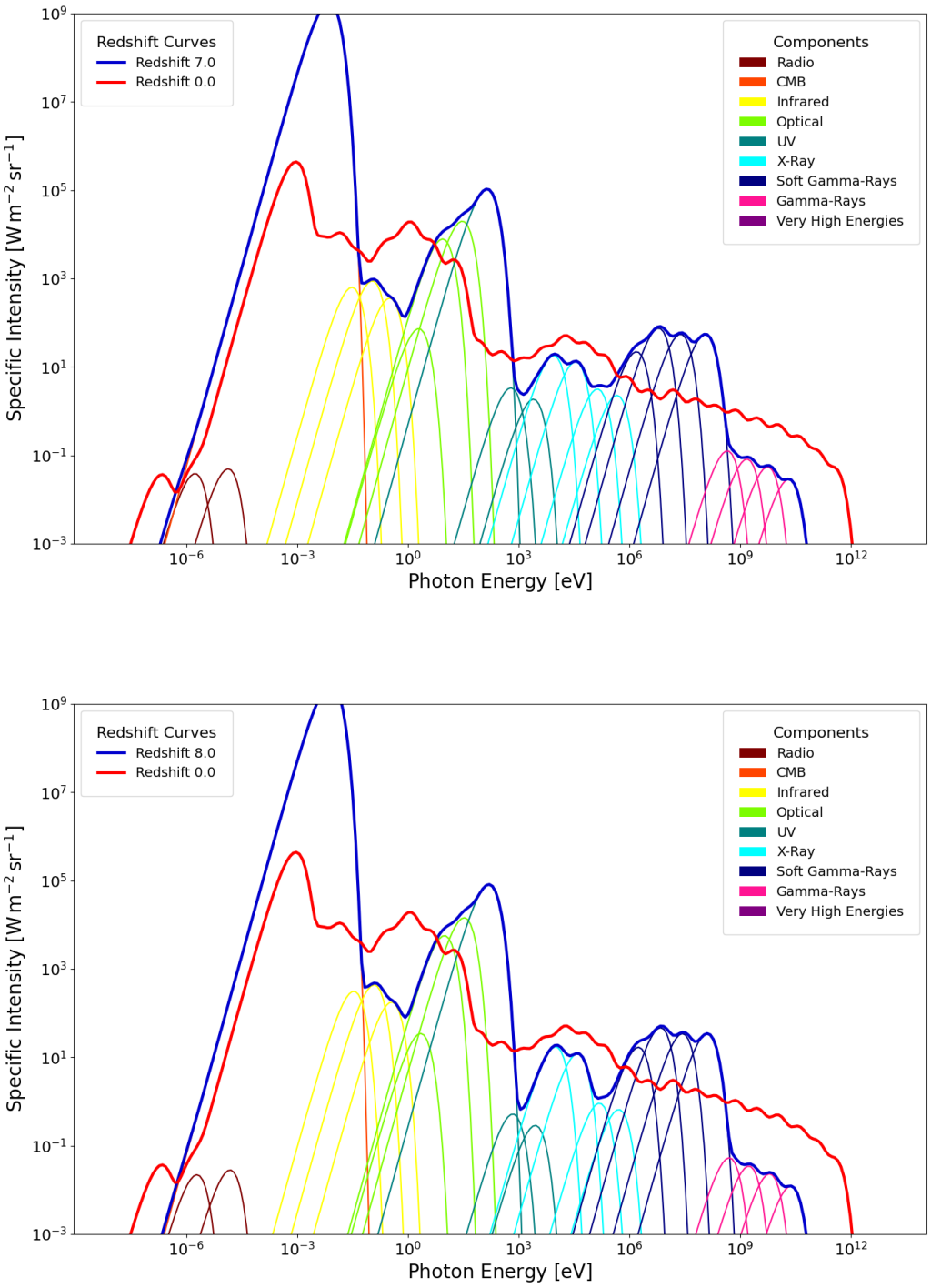

Figure 5: Blackbody evolution of the CPB for Redshift 7.0 (top), and 8.0 (bottom).

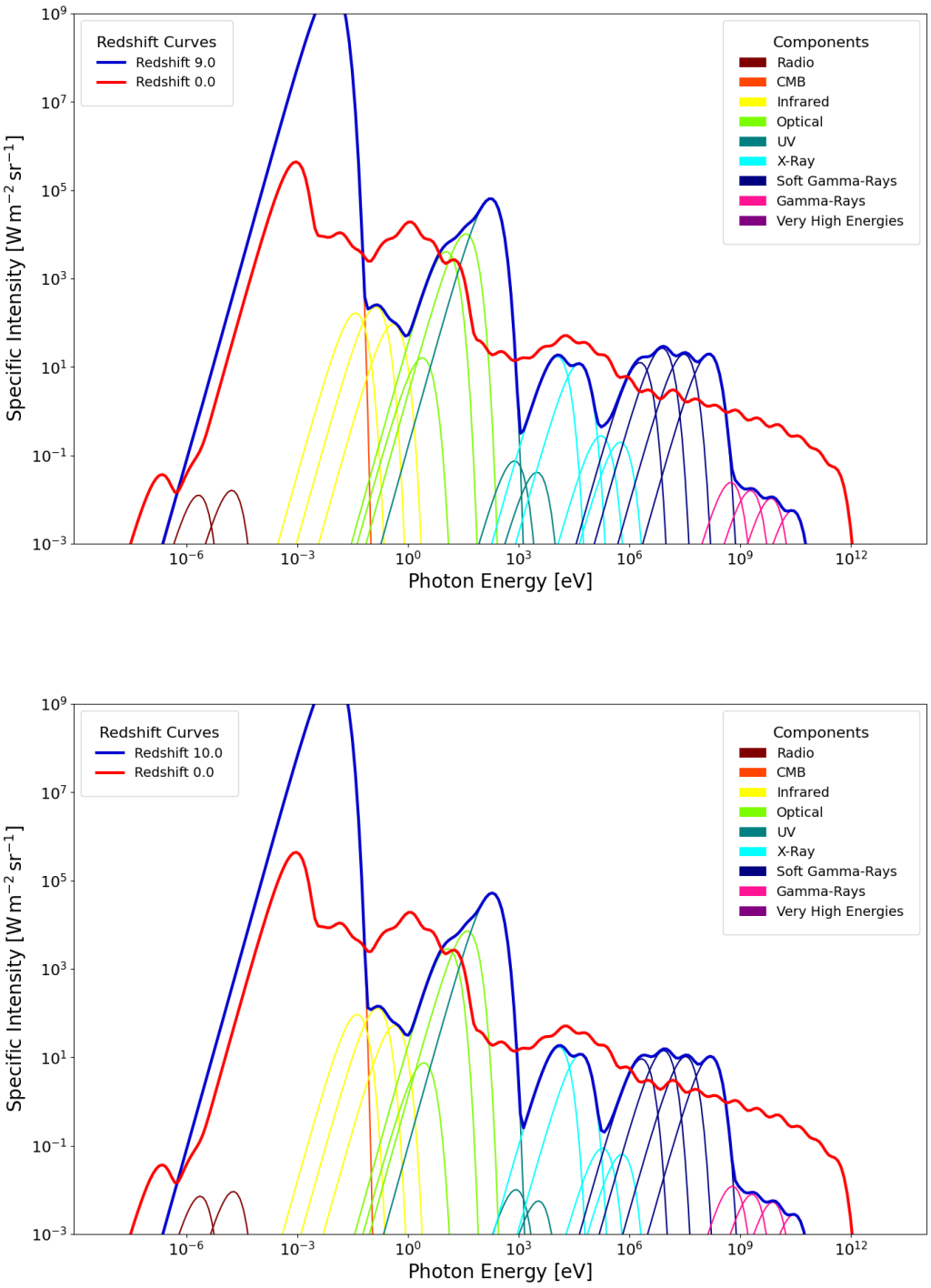

Figure 6: Blackbody evolution of the CPB for Redshift 9.0 (top), and 10.0 (bottom).

Positron emissivities

Redshift z	Positron emissivity [$\mathrm{cm^{-3}\,s^{-1}}$]	Redshift z	Positron emissivity [$\mathrm{cm^{-3}\,s^{-1}}$]
0.1	$4.213 \cdot 10^{-36}$	2.6	$1.755 \cdot 10^{-31}$
0.2	$9.217 \cdot 10^{-36}$	2.7	$1.755 \cdot 10^{-31}$
0.3	$2.151 \cdot 10^{-35}$	2.8	$1.738 \cdot 10^{-31}$
0.4	$1.189 \cdot 10^{-35}$	2.9	$1.708 \cdot 10^{-31}$
0.5	$5.111 \cdot 10^{-35}$	3.0	$1.671 \cdot 10^{-31}$
0.6	$2.662 \cdot 10^{-34}$	3.1	$1.632 \cdot 10^{-31}$
0.7	$5.721 \cdot 10^{-34}$	3.2	$1.595 \cdot 10^{-31}$
0.8	$1.181 \cdot 10^{-33}$	3.3	$1.564 \cdot 10^{-31}$
0.9	$2.334 \cdot 10^{-33}$	3.4	$1.540 \cdot 10^{-31}$
1.0	$4.401 \cdot 10^{-33}$	3.5	$1.523 \cdot 10^{-31}$
1.1	$7.863 \cdot 10^{-33}$	3.6	$1.514 \cdot 10^{-31}$
1.2	$1.321 \cdot 10^{-32}$	3.7	$1.509 \cdot 10^{-31}$
1.3	$2.080 \cdot 10^{-32}$	3.8	$1.507 \cdot 10^{-31}$
1.4	$3.074 \cdot 10^{-32}$	3.9	$1.504 \cdot 10^{-31}$
1.5	$4.295 \cdot 10^{-32}$	4.0	$1.500 \cdot 10^{-31}$
1.6	$5.722 \cdot 10^{-32}$	4.1	$1.486 \cdot 10^{-31}$
1.7	$7.314 \cdot 10^{-32}$	4.2	$1.466 \cdot 10^{-31}$
1.8	$9.002 \cdot 10^{-32}$	4.3	$1.437 \cdot 10^{-31}$
1.9	$1.070 \cdot 10^{-31}$	4.4	$1.400 \cdot 10^{-31}$
2.0	$1.233 \cdot 10^{-31}$	4.5	$1.356 \cdot 10^{-31}$
2.1	$1.381 \cdot 10^{-31}$	4.6	$1.306 \cdot 10^{-31}$
2.2	$1.508 \cdot 10^{-31}$	4.7	$1.250 \cdot 10^{-31}$
2.3	$1.610 \cdot 10^{-31}$	4.8	$1.192 \cdot 10^{-31}$
2.4	$1.685 \cdot 10^{-31}$	4.9	$1.132 \cdot 10^{-31}$
2.5	$1.732 \cdot 10^{-31}$	5.0	$1.072 \cdot 10^{-31}$

Table 9: Positron emissivity at given redshift up to redshift 5.0.

Redshift z	Positron emissivity [$\mathrm{cm^{-3}\,s^{-1}}$]	Redshift z	Positron emissivity [$\mathrm{cm^{-3}\,s^{-1}}$]
5.1	$1.013 \cdot 10^{-31}$	7.6	$2.619 \cdot 10^{-32}$
5.2	$9.553 \cdot 10^{-32}$	7.7	$2.509 \cdot 10^{-32}$
5.3	$8.999 \cdot 10^{-32}$	7.8	$2.406 \cdot 10^{-32}$
5.4	$8.470 \cdot 10^{-32}$	7.9	$2.309 \cdot 10^{-32}$
5.5	$7.969 \cdot 10^{-32}$	8.0	$2.217 \cdot 10^{-32}$
5.6	$7.497 \cdot 10^{-32}$	8.1	$2.130 \cdot 10^{-32}$
5.7	$7.055 \cdot 10^{-32}$	8.2	$2.048 \cdot 10^{-32}$
5.8	$6.641 \cdot 10^{-32}$	8.3	$1.967 \cdot 10^{-32}$
5.9	$6.255 \cdot 10^{-32}$	8.4	$1.895 \cdot 10^{-32}$
6.0	$5.896 \cdot 10^{-32}$	8.5	$1.824 \cdot 10^{-32}$
6.1	$5.562 \cdot 10^{-32}$	8.6	$1.757 \cdot 10^{-32}$
6.2	$5.251 \cdot 10^{-32}$	8.7	$1.692 \cdot 10^{-32}$
6.3	$4.963 \cdot 10^{-32}$	8.8	$1.630 \cdot 10^{-32}$
6.4	$4.695 \cdot 10^{-32}$	8.9	$1.571 \cdot 10^{-32}$
6.5	$4.447 \cdot 10^{-32}$	9.0	$1.514 \cdot 10^{-32}$
6.6	$4.216 \cdot 10^{-32}$	9.1	$1.460 \cdot 10^{-32}$
6.7	$4.002 \cdot 10^{-32}$	9.2	$1.408 \cdot 10^{-32}$
6.8	$3.802 \cdot 10^{-32}$	9.3	$1.357 \cdot 10^{-32}$
6.9	$3.616 \cdot 10^{-32}$	9.4	$1.309 \cdot 10^{-32}$
7.0	$3.443 \cdot 10^{-32}$	9.5	$1.263 \cdot 10^{-32}$
7.1	$3.282 \cdot 10^{-32}$	9.6	$1.218 \cdot 10^{-32}$
7.2	$3.131 \cdot 10^{-32}$	9.7	$1.175 \cdot 10^{-32}$
7.3	$2.990 \cdot 10^{-32}$	9.8	$1.133 \cdot 10^{-32}$
7.4	$2.859 \cdot 10^{-32}$	9.9	$1.093 \cdot 10^{-32}$
7.5	$2.735 \cdot 10^{-32}$	10.0	$1.054 \cdot 10^{-32}$

Table 10: Positron emissivity for a given redshift up to a redshift of 10.0.

Positron production rates

Redshift z	Positron production rate [s^{-1}]	Redshift z	Positron production rate [s^{-1}]
0.1	$1.311 \cdot 10^{47}$	2.6	$2.725 \cdot 10^{53}$
0.2	$9.817 \cdot 10^{47}$	2.7	$2.718 \cdot 10^{53}$
0.3	$4.585 \cdot 10^{48}$	2.8	$2.680 \cdot 10^{53}$
0.4	$1.727 \cdot 10^{49}$	2.9	$2.621 \cdot 10^{53}$
0.5	$5.594 \cdot 10^{49}$	3.0	$2.549 \cdot 10^{53}$
0.6	$1.606 \cdot 10^{50}$	3.1	$2.473 \cdot 10^{53}$
0.7	$4.183 \cdot 10^{50}$	3.2	$2.400 \cdot 10^{53}$
0.8	$1.004 \cdot 10^{51}$	3.3	$2.334 \cdot 10^{53}$
0.9	$2.241 \cdot 10^{51}$	3.4	$2.279 \cdot 10^{53}$
1.0	$4.659 \cdot 10^{51}$	3.5	$2.236 \cdot 10^{53}$
1.1	$9.009 \cdot 10^{51}$	3.6	$2.202 \cdot 10^{53}$
1.2	$1.615 \cdot 10^{52}$	3.7	$2.175 \cdot 10^{53}$
1.3	$2.679 \cdot 10^{52}$	3.8	$2.150 \cdot 10^{53}$
1.4	$4.134 \cdot 10^{52}$	3.9	$2.125 \cdot 10^{53}$
1.5	$5.982 \cdot 10^{52}$	4.0	$2.095 \cdot 10^{53}$
1.6	$8.199 \cdot 10^{52}$	4.1	$2.056 \cdot 10^{53}$
1.7	$1.072 \cdot 10^{53}$	4.2	$2.007 \cdot 10^{53}$
1.8	$1.343 \cdot 10^{53}$	4.3	$1.947 \cdot 10^{53}$
1.9	$1.620 \cdot 10^{53}$	4.4	$1.877 \cdot 10^{53}$
2.0	$1.887 \cdot 10^{53}$	4.5	$1.798 \cdot 10^{53}$
2.1	$2.130 \cdot 10^{53}$	4.6	$1.712 \cdot 10^{53}$
2.2	$2.337 \cdot 10^{53}$	4.7	$1.622 \cdot 10^{53}$
2.3	$2.503 \cdot 10^{53}$	4.8	$1.529 \cdot 10^{53}$
2.4	$2.622 \cdot 10^{53}$	4.9	$1.436 \cdot 10^{53}$
2.5	$2.695 \cdot 10^{53}$	5.0	$1.345 \cdot 10^{53}$

Table 11: Positron production rates up to a redshift of 5.0.

Redshift z	Positron production rate [s^{-1}]	Redshift z	Positron production rate [s^{-1}]
5.1	$1.256 \cdot 10^{53}$	7.6	$2.468 \cdot 10^{52}$
5.2	$1.171 \cdot 10^{53}$	7.7	$2.341 \cdot 10^{52}$
5.3	$1.091 \cdot 10^{53}$	7.8	$2.221 \cdot 10^{52}$
5.4	$1.015 \cdot 10^{53}$	7.9	$2.110 \cdot 10^{52}$
5.5	$9.446 \cdot 10^{52}$	8.0	$2.005 \cdot 10^{52}$
5.6	$8.787 \cdot 10^{52}$	8.1	$1.907 \cdot 10^{52}$
5.7	$8.176 \cdot 10^{52}$	8.2	$1.815 \cdot 10^{52}$
5.8	$7.611 \cdot 10^{52}$	8.3	$1.728 \cdot 10^{52}$
5.9	$7.088 \cdot 10^{52}$	8.4	$1.646 \cdot 10^{52}$
6.0	$6.607 \cdot 10^{52}$	8.5	$1.569 \cdot 10^{52}$
6.1	$6.164 \cdot 10^{52}$	8.6	$1.496 \cdot 10^{52}$
6.2	$5.755 \cdot 10^{52}$	8.7	$1.427 \cdot 10^{52}$
6.3	$5.379 \cdot 10^{52}$	8.8	$1.361 \cdot 10^{52}$
6.4	$5.034 \cdot 10^{52}$	8.9	$1.299 \cdot 10^{52}$
6.5	$4.715 \cdot 10^{52}$	9.0	$1.240 \cdot 10^{52}$
6.6	$4.422 \cdot 10^{52}$	9.1	$1.184 \cdot 10^{52}$
6.7	$4.151 \cdot 10^{52}$	9.2	$1.131 \cdot 10^{52}$
6.8	$3.902 \cdot 10^{52}$	9.3	$1.080 \cdot 10^{52}$
6.9	$3.671 \cdot 10^{52}$	9.4	$1.032 \cdot 10^{52}$
7.0	$3.458 \cdot 10^{52}$	9.5	$9.859 \cdot 10^{51}$
7.1	$3.261 \cdot 10^{52}$	9.6	$9.421 \cdot 10^{51}$
7.2	$3.078 \cdot 10^{52}$	9.7	$9.003 \cdot 10^{51}$
7.3	$2.909 \cdot 10^{52}$	9.8	$8.605 \cdot 10^{51}$
7.4	$2.751 \cdot 10^{52}$	9.9	$8.225 \cdot 10^{51}$
7.5	$2.605 \cdot 10^{52}$	10.0	$7.862 \cdot 10^{51}$

Table 12: Positron production rates up to a redshift of 10.0.

Comoving volume of spherical shells

Redshift z	Comoving shell volumes [cm^3]	Redshift z	Comoving shell volumes [cm^3]
0.1	$3.113 \cdot 10^{82}$	2.6	$1.553 \cdot 10^{84}$
0.2	$1.065 \cdot 10^{83}$	2.7	$1.549 \cdot 10^{84}$
0.3	$2.131 \cdot 10^{83}$	2.8	$1.542 \cdot 10^{84}$
0.4	$3.379 \cdot 10^{83}$	2.9	$1.534 \cdot 10^{84}$
0.5	$4.704 \cdot 10^{83}$	3.0	$1.525 \cdot 10^{84}$
0.6	$6.032 \cdot 10^{83}$	3.1	$1.515 \cdot 10^{84}$
0.7	$7.311 \cdot 10^{83}$	3.2	$1.505 \cdot 10^{84}$
0.8	$8.507 \cdot 10^{83}$	3.3	$1.493 \cdot 10^{84}$
0.9	$9.601 \cdot 10^{83}$	3.4	$1.481 \cdot 10^{84}$
1.0	$1.059 \cdot 10^{84}$	3.5	$1.468 \cdot 10^{84}$
1.1	$1.146 \cdot 10^{84}$	3.6	$1.454 \cdot 10^{84}$
1.2	$1.222 \cdot 10^{84}$	3.7	$1.441 \cdot 10^{84}$
1.3	$1.288 \cdot 10^{84}$	3.8	$1.427 \cdot 10^{84}$
1.4	$1.345 \cdot 10^{84}$	3.9	$1.413 \cdot 10^{84}$
1.5	$1.393 \cdot 10^{84}$	4.0	$1.389 \cdot 10^{84}$
1.6	$1.433 \cdot 10^{84}$	4.1	$1.384 \cdot 10^{84}$
1.7	$1.466 \cdot 10^{84}$	4.2	$1.369 \cdot 10^{84}$
1.8	$1.492 \cdot 10^{84}$	4.3	$1.355 \cdot 10^{84}$
1.9	$1.514 \cdot 10^{84}$	4.4	$1.340 \cdot 10^{84}$
2.0	$1.530 \cdot 10^{84}$	4.5	$1.326 \cdot 10^{84}$
2.1	$1.542 \cdot 10^{84}$	4.6	$1.311 \cdot 10^{84}$
2.2	$1.550 \cdot 10^{84}$	4.7	$1.297 \cdot 10^{84}$
2.3	$1.555 \cdot 10^{84}$	4.8	$1.282 \cdot 10^{84}$
2.4	$1.557 \cdot 10^{84}$	4.9	$1.268 \cdot 10^{84}$
2.5	$1.556 \cdot 10^{84}$	5.0	$1.254 \cdot 10^{84}$

Table 13: Comoving volumes of spherical shells up to redshift 5.0; each value represents the volume between $z - 0.05$ and $z + 0.05$.

Redshift z	Comoving shell volumes [cm^3]	Redshift z	Comoving shell volumes [cm^3]
5.1	$1.240 \cdot 10^{84}$	7.6	$9.425 \cdot 10^{83}$
5.2	$1.226 \cdot 10^{84}$	7.7	$9.327 \cdot 10^{83}$
5.3	$1.212 \cdot 10^{84}$	7.8	$9.231 \cdot 10^{83}$
5.4	$1.199 \cdot 10^{84}$	7.9	$9.137 \cdot 10^{83}$
5.5	$1.185 \cdot 10^{84}$	8.0	$9.044 \cdot 10^{83}$
5.6	$1.172 \cdot 10^{84}$	8.1	$8.952 \cdot 10^{83}$
5.7	$1.159 \cdot 10^{84}$	8.2	$8.862 \cdot 10^{83}$
5.8	$1.146 \cdot 10^{84}$	8.3	$8.773 \cdot 10^{83}$
5.9	$1.133 \cdot 10^{84}$	8.4	$8.686 \cdot 10^{83}$
6.0	$1.121 \cdot 10^{84}$	8.5	$8.600 \cdot 10^{83}$
6.1	$1.108 \cdot 10^{84}$	8.6	$8.515 \cdot 10^{83}$
6.2	$1.096 \cdot 10^{84}$	8.7	$8.432 \cdot 10^{83}$
6.3	$1.084 \cdot 10^{84}$	8.8	$8.350 \cdot 10^{83}$
6.4	$1.072 \cdot 10^{84}$	8.9	$8.269 \cdot 10^{83}$
6.5	$1.060 \cdot 10^{84}$	9.0	$8.189 \cdot 10^{83}$
6.6	$1.049 \cdot 10^{84}$	9.1	$8.111 \cdot 10^{83}$
6.7	$1.037 \cdot 10^{84}$	9.2	$8.034 \cdot 10^{83}$
6.8	$1.026 \cdot 10^{84}$	9.3	$7.958 \cdot 10^{83}$
6.9	$1.015 \cdot 10^{84}$	9.4	$7.883 \cdot 10^{83}$
7.0	$1.004 \cdot 10^{84}$	9.5	$7.809 \cdot 10^{83}$
7.1	$9.936 \cdot 10^{83}$	9.6	$7.736 \cdot 10^{83}$
7.2	$9.830 \cdot 10^{83}$	9.7	$7.665 \cdot 10^{83}$
7.3	$9.726 \cdot 10^{83}$	9.8	$7.594 \cdot 10^{83}$
7.4	$9.624 \cdot 10^{83}$	9.9	$7.525 \cdot 10^{83}$
7.5	$9.524 \cdot 10^{83}$	10.0	$7.456 \cdot 10^{83}$

Table 14: Comoving volumes of spherical shells up to redshift 10.0; each value represents the volume between $z - 0.05$ and $z + 0.05$.

Comoving distance of each redshift bin

Redshift z	Comoving distance [cm]	Redshift z	Comoving distance [cm]
0.1	$1.302 \cdot 10^{27}$	2.6	$3.505 \cdot 10^{26}$
0.2	$1.235 \cdot 10^{27}$	2.7	$3.370 \cdot 10^{26}$
0.3	$1.167 \cdot 10^{27}$	2.8	$3.243 \cdot 10^{26}$
0.4	$1.101 \cdot 10^{27}$	2.9	$3.124 \cdot 10^{26}$
0.5	$1.037 \cdot 10^{27}$	3.0	$3.011 \cdot 10^{26}$
0.6	$9.759 \cdot 10^{26}$	3.1	$2.905 \cdot 10^{26}$
0.7	$9.182 \cdot 10^{26}$	3.2	$2.805 \cdot 10^{26}$
0.8	$8.642 \cdot 10^{26}$	3.3	$2.710 \cdot 10^{26}$
0.9	$8.138 \cdot 10^{26}$	3.4	$2.621 \cdot 10^{26}$
1.0	$7.670 \cdot 10^{26}$	3.5	$2.536 \cdot 10^{26}$
1.1	$7.236 \cdot 10^{26}$	3.6	$2.456 \cdot 10^{26}$
1.2	$6.835 \cdot 10^{26}$	3.7	$2.379 \cdot 10^{26}$
1.3	$6.464 \cdot 10^{26}$	3.8	$2.307 \cdot 10^{26}$
1.4	$6.121 \cdot 10^{26}$	3.9	$2.238 \cdot 10^{26}$
1.5	$5.803 \cdot 10^{26}$	4.0	$2.172 \cdot 10^{26}$
1.6	$5.510 \cdot 10^{26}$	4.1	$2.110 \cdot 10^{26}$
1.7	$5.238 \cdot 10^{26}$	4.2	$2.050 \cdot 10^{26}$
1.8	$4.986 \cdot 10^{26}$	4.3	$1.993 \cdot 10^{26}$
1.9	$4.752 \cdot 10^{26}$	4.4	$1.939 \cdot 10^{26}$
2.0	$4.534 \cdot 10^{26}$	4.5	$1.887 \cdot 10^{26}$
2.1	$4.332 \cdot 10^{26}$	4.6	$1.837 \cdot 10^{26}$
2.2	$4.144 \cdot 10^{26}$	4.7	$1.789 \cdot 10^{26}$
2.3	$3.968 \cdot 10^{26}$	4.8	$1.744 \cdot 10^{26}$
2.4	$3.803 \cdot 10^{26}$	4.9	$1.700 \cdot 10^{26}$
2.5	$3.650 \cdot 10^{26}$	5.0	$1.658 \cdot 10^{26}$

Table 15: Comoving distances within each redshift bin up to redshift 5.0; each value represents the comoving distance between $z - 0.05$ and $z + 0.05$.

Redshift z	Comoving distance [cm]	Redshift z	Comoving distance [cm]
5.1	$1.618 \cdot 10^{26}$	7.6	$9.693 \cdot 10^{25}$
5.2	$1.579 \cdot 10^{26}$	7.7	$9.526 \cdot 10^{25}$
5.3	$1.542 \cdot 10^{26}$	7.8	$9.365 \cdot 10^{25}$
5.4	$1.507 \cdot 10^{26}$	7.9	$9.208 \cdot 10^{25}$
5.5	$1.472 \cdot 10^{26}$	8.0	$9.055 \cdot 10^{25}$
5.6	$1.439 \cdot 10^{26}$	8.1	$8.907 \cdot 10^{25}$
5.7	$1.407 \cdot 10^{26}$	8.2	$8.762 \cdot 10^{25}$
5.8	$1.376 \cdot 10^{26}$	8.3	$8.621 \cdot 10^{25}$
5.9	$1.347 \cdot 10^{26}$	8.4	$8.484 \cdot 10^{25}$
6.0	$1.318 \cdot 10^{26}$	8.5	$8.351 \cdot 10^{25}$
6.1	$1.291 \cdot 10^{26}$	8.6	$8.221 \cdot 10^{25}$
6.2	$1.264 \cdot 10^{26}$	8.7	$8.095 \cdot 10^{25}$
6.3	$1.238 \cdot 10^{26}$	8.8	$7.971 \cdot 10^{25}$
6.4	$1.213 \cdot 10^{26}$	8.9	$7.851 \cdot 10^{25}$
6.5	$1.189 \cdot 10^{26}$	9.0	$7.714 \cdot 10^{25}$
6.6	$1.166 \cdot 10^{26}$	9.1	$7.619 \cdot 10^{25}$
6.7	$1.143 \cdot 10^{26}$	9.2	$7.508 \cdot 10^{25}$
6.8	$1.122 \cdot 10^{26}$	9.3	$7.399 \cdot 10^{25}$
6.9	$1.100 \cdot 10^{26}$	9.4	$7.292 \cdot 10^{25}$
7.0	$1.080 \cdot 10^{26}$	9.5	$7.188 \cdot 10^{25}$
7.1	$1.060 \cdot 10^{26}$	9.6	$7.087 \cdot 10^{25}$
7.2	$1.041 \cdot 10^{26}$	9.7	$6.988 \cdot 10^{25}$
7.3	$1.022 \cdot 10^{26}$	9.8	$6.891 \cdot 10^{25}$
7.4	$1.004 \cdot 10^{26}$	9.9	$6.797 \cdot 10^{25}$
7.5	$9.864 \cdot 10^{25}$	10.0	$6.704 \cdot 10^{25}$

Table 16: Comoving distances within each redshift bin up to redshift 10.0; each value represents the comoving distance between $z - 0.05$ and $z + 0.05$.

Acknowledgments

Zuallererst möchte ich Thomas dafür danken, dass ich bei ihm in der Arbeitsgruppe an so einem spannenden Thema arbeiten durfte. Durch seine stets hilfreichen Anmerkungen und Ideen habe ich viel gelernt und viel Freude an dieser Arbeit gehabt. Darüber hinaus bin ich dankbar, dass er es mir als Teil seiner Arbeitsgruppe ermöglicht hat, zum allerersten Mal eine Konferenz zu besuchen. In der Arbeitsgruppe habe ich mich immer sehr wohl und wertgeschätzt gefühlt und ich bin froh, dass ich all diese Menschen, die Teil der AG Siegert sind, kennenlernen durfte.

Daneben geht auch noch ein Dank an meine Eltern. Ich bin dankbar für die jahrelange Förderung und Unterstützung, die sie mir während dieses Studiums gegeben haben. Ich bin froh, dass sie mich zu dem Menschen gemacht haben, der ich bin.

Zuletzt bin ich den vielen, tollen Menschen dankbar, denen ich über die Jahre hinweg hier in Würzburg begegnet bin – deren Menge ist so groß, dass ich sie hier gar nicht aufzählen könnte! Explizit hervorheben möchte ich Julius, Nico, Christian, Maria, Jakob und Samu, mit denen ich über die Jahre unfassbar viel Zeit außerhalb und innerhalb der Uni verbracht habe. Ihr habt mich zu einem besseren Menschen gemacht – ich hoffe, ihr seht das andersherum genauso!

Declaration of originality

I declare that I have authored this thesis independently, that I have not used other than the declared sources / resources, and that I have explicitly marked all material which has been quoted either literally or by content from the used sources.

Würzburg, July 9, 2025

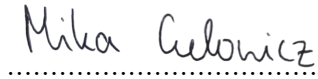

Mika Gelowicz

Julius-Maximilians-
UNIVERSITÄT
WÜRZBURG

Versicherung zur selbständigen Leistungserbringung

Titel der Bachelorarbeit:

Calculation of Electron-Positron Pair Production from the Cosmic Photon Background as a Function of Redshift

Thema bereitgestellt von (Titel, Vorname, Nachname, Lehrstuhl):
Dr. Thomas Siegert, Lehrstuhl für Astronomie

Eingereicht durch (Vorname, Nachname, Matrikel):
Mika Gelowicz, 2761183

Ich versichere, dass ich die vorstehende schriftliche Arbeit selbständig verfasst und keine anderen als die angegebenen Quellen und Hilfsmittel benutzt habe. Die benutzte Literatur sowie sonstige Hilfsquellen sind vollständig angegeben. Wörtlich oder dem Sinne nach dem Schrifttum oder dem Internet entnommene Stellen sind unter Angabe der Quelle kenntlich gemacht.

Weitere Personen waren an der geistigen Leistung der vorliegenden Arbeit nicht beteiligt. Insbesondere habe ich nicht die Hilfe eines Ghostwriters oder einer Ghostwriting-Agentur in Anspruch genommen. Dritte haben von mir weder unmittelbar noch mittelbar Geld oder geldwerte Leistungen für Arbeiten erhalten, die im Zusammenhang mit dem Inhalt der vorgelegten Arbeit stehen.

☒ Mit dem Prüfungsleiter bzw. der Prüfungsleiterin wurde abgestimmt, dass für die Erstellung der vorgelegten schriftlichen Arbeit Chatbots (insbesondere ChatGPT) bzw. allgemein solche Programme, die anstelle meiner Person die Aufgabenstellung der Prüfung bzw. Teile derselben bearbeiten könnten, entsprechend den Vorgaben der Prüfungsleiterin bzw. des Prüfungsleiters eingesetzt wurden. Die mittels Chatbots erstellten Passagen sind als solche gekennzeichnet.

Der Durchführung einer elektronischen Plagiatsprüfung stimme ich hiermit zu. Die eingereichte elektronische Fassung der Arbeit ist vollständig. Mir ist bewusst, dass nachträgliche Ergänzungen ausgeschlossen sind.

Die Arbeit wurde bisher keiner anderen Prüfungsbehörde vorgelegt und auch nicht veröffentlicht. Ich bin mir bewusst, dass eine unwahre Erklärung zur Versicherung der selbstständigen Leistungserbringung rechtliche Folgen haben kann.

Würzburg, 09.07.2025 Mika Gelowicz

Ort, Datum, Unterschrift